



since 1558

Preparation and characterization of planar hybrid
Josephson junctions based on Ba-122
Pnictide single crystals

Dissertation
to obtain the academic degree of
doctor of natural sciences (Dr. rer. nat.)

The dissertation submitted to the council of the Faculty of Physics and
Astronomy at Friedrich-Schiller-Universität Jena

By M.Sc. of physics Noor Ali Hasan
born on 24.01.1984 in Baghdad

„Printed with the support of the German Academic Exchange Service

DAAD“

„Gedruckt mit Unterstützung des Deutschen Akademischen

Austauschdienstes DAAD“

Referees

1. Prof. Dr. rer. nat. habil. Paul Seidel
2. Prof. Dr. rer. nat. habil. Hannes Töpfer
3. Prof. Dr. rer. nat. habil. Michael Siegel

Date of defense: 06.12.2016

SYMBOLS AND ABBREVIATIONS

T, T_c	– Temperature, Critical temperature
$B, B_{c,c1,c2}$	– Magnetic flux density, Critical magnetic flux densities
$H, H_{c,c1,c2}$	– Magnetic field, Critical magnetic field
n_s	– Density of Cooper pairs
λ_L	– London penetration depth
$\xi, \xi(0)$	– Coherence length, Coherence length at $T=0$
$\xi_{GL}(T)$	– Ginzburg-Landau coherence length
m	– Mass
q, q_s	– Charge, Charge of the Cooper pair
Ψ, Ψ_0	– Wave function, Amplitude of the wave function
E_F	– Fermi energy
t, τ	– Time, Normalized time
r	– Space vector
ϕ, φ	– Phase, Phase difference of the Josephson junction
J, J_c	– Current density, Critical current density
A	– Magnetic vector potential
R, R_N	– Electrical resistance, Normal junction resistance
V	– Electrical voltage
i_b	– Normalized bias current
I, I_c	– Current, Critical current
I_{ex}, I_R	– Excess current, Return current
C	– Capacity
$\Delta, \Delta(0)$	– Energy gap in the superconductor, Energy gap at $T = 0$
Ψ_{GL}	– Order parameter
f, ω, ω_c	– Frequency, Angular frequency, Natural frequency of the Josephson junction
i_m	– Normalized microwave amplitude
Γ	– Dynes parameter
β_c	– McCumber parameter
G, G_N	– Conductance, Normalized conductance
γ	– Conductance noise parameter
ω_{mw}, Ω	– Microwave frequency, Relative microwave frequency
Ω_b	– Phonon frequency
$e = 1.602\ 176\ 487\ 4 \cdot 10^{-19}$ C	– Elementary charge
$m_0 = 9.109\ 382\ 154\ 5 \cdot 10^{-31}$ kg	– The rest mass of the free electron
$k_B = 1.380\ 650\ 424 \cdot 10^{-23}$ J.K ⁻¹	– Boltzmann constant
$h = 2\pi\hbar = 6.626\ 068\ 963\ 3 \cdot 10^{-34}$ J.s	– Planck constant
$\Phi_0 = h/2e = 2.067\ 833\ 758 \cdot 10^{-15}$ T.m ²	– Flux quantum

TABLE OF CONTENTS

1 Introduction	
1.1. Motivation	3
1.2. Aim of work.	3
2 Fundamentals	
2.1 Superconductivity	5
2.2 Energy gap	9
2.3 Iron - based superconductors	11
2.4 Josephson junctions	14
2.5 Josephson equations	16
2.5.1 d.c effect	16
2.5.2 a.c effect	17
2.6 I-V characteristics of Josephson junctions	17
2.7 Inverse a.c effect (Microwaves dependence)	21
2.8 Josephson junctions in an external magnetic field	22
2.9 Spectroscopy.	23
2.10 Andreev reflection and tunneling spectroscopy	24
3 Material processing and examination	
3.1 Materials	27
3.1.1 Crystals growth	27
3.1.2 EDX-ray spectroscopy analysis	28
3.2 Crystals processing	30
3.2.1 Cleaving.	30
3.2.2 Sticking	30
3.2.3 Polishing	31
3.3 Etching rate of single crystal	33
3.4 Examination the crystal surface by EBSD-measurements.	34

4 Thin film technology and Sample preparation	
4.1 Thin film technology	37
4.1.1 Photolithography and junction layout	37
4.1.2 Equipment for thin film technology	39
4.1.2.1 Sputtering systems	39
4.1.2.1. a DC-Magnetron sputtering	39
4.1.2.1. b RF- Magnetron sputtering	40
4.1.3 Ion beam etching	40
4.1.4 Thermal evaporation	40
4.2 Junction fabrication	41
4.3 Electrical measuring techniques	46
4.4 Techniques to fabricate point contact	48
5 Investigation of Josephson Junctions	
5.1 Planar hybrid junctions based on undoped Ba-122 single crystals	
5.1.1 Current voltage characteristic	50
5.1.2 Spectroscopy	51
5.2 Planar hybrid Josephson junctions based on Co-doped Ba-122 single crystals	
5.2.1 Current voltage characteristic & temperature dependence	52
5.2.2 Microwave irradiation	58
5.2.3 Magnetic field dependence	59
5.2.4 Spectroscopy	61
5.3 Point contact Andreev Reflection and tunneling spectroscopy	
5.3.1 Niobium tip pressed on unprocessed surface of single crystals	63
5.3.2 Niobium tip pressed on processed surface of single crystals	65
5.3.3 Gold tip pressed on processed surface of single crystals	66
5.3.4 Difficulties in the point contact spectroscopy measurements	67
6 Summary and Conclusions	68
References	70
List of Figures	80
Acknowledgement	85

1. INTRODUCTION

1.1 MOTIVATION

Iron-based superconductors (FBS) are a new family of unconventional high - temperature superconductors discovered in 2006 [1]. The record of the critical temperature (T_c) rose to 55 K in 2008 [2]. Since this date, the discovery of FBS gained a great attention and much effort which has been made whether to experimental or theoretical works, to understand the nature of the superconductivity in iron pnictides and their fundamental properties such as energy gap and order parameter symmetry. FBS show very interesting properties like high critical current density [3, 4] and magnetic field. Most important for the still missing understanding in FBS is the pairing symmetry of the order parameter (OP) which is proposed to be s_{\pm} -wave unconventional symmetry. Up to now, there is no consensus on its symmetry. Some literature argues for the nodeless s_{\pm} symmetry with sign change between the Fermi pockets [5] others display nodal s_{\pm} symmetry [6], s_{++} state [7] and even d-wave [8]. Therefore, the symmetry of the pnictides remains one of the main topics for discussion. Andreev reflection, tunneling and Josephson effect measurements are excellent experimental methods which can give an indication about these properties such as the symmetry of the energy gap. There are some publications which are based on the Josephson effect, to provide proof of the symmetry from phase sensitive contact measurements on devices consisting of two Josephson junctions [9-11]. In order to provide proof of the predictions of the s_{\pm} -symmetry, other references show how the s_{\pm} -symmetry has an effect on a tunnel or point contact spectrum [12- 15], as well as on the $I_c R_N$ -product of Josephson junctions [16- 21].

1.2 AIMS OF WORK

The main concerns in this research work are two aspects; first one is to fabricate Josephson junctions and tunnel contacts on iron pnictide single crystals. While the second aspect is to direct many efforts to characterize, modeling for understanding the novel properties of these exotic materials.

The tetragonal crystal system of $\text{Ba}(\text{Fe}_{1-x}\text{Co}_x)_2\text{As}_2$ single crystals ($x \approx 0.06$, $T_c = 23.5$ K) were produced by a self-flux method [22, 23]. The single crystals surface as grown has usually a rough surface structure. To realize tunneling and Josephson junctions (JJs) along the crystallographic c-axis, the standard technique procedure is based on the photolithographic preparation process used for pnictide thin films. The advantages of using pnictide single crystals are superior to thin films in various aspects (e.g. purity, better crystalline structure, easier to dope etc.). Nevertheless, thin film technologies require high-quality surfaces. Thus these make it necessary to apply a polishing procedure for these materials. Therefore chemical- mechanical polishing used in order to reach a root mean square (RMS) roughness of less than 5 nm. For this process, the surface structure is tested before the actual start of junction fabrication. The electron backscattering diffraction (EBSD)

analysis was used to evaluate quantitative microstructure analysis surface. Another problem with crystals surface is the crystal surface degradation over time at atmosphere. Additionally, it is sensitive to water and acetone, which are supposed to use in a photolithography process for junction preparation. Thus an additional sputtered Au layer is used to protect the sample's surface. In that way, it should be able to fabricate the junctions. That shows the reasons that there is no published paper on the single crystals materials similar to this technique, to our knowledge. Therefore it has been studied extensively.

One of the major points in this work is to realize a planar hybrid Josephson SNS*, SIS* junctions, where Ba-122 single crystals act as a base electrodes (S) with different barriers, including normal metals (Au, Ti), as well as subsequently oxidized thin metal films (Ti, Al) resulting in insulating barriers (TiO_x, AlO_x) on polished surfaces of pnictide single crystals.

Thermally evaporated layers of lead and indium (PbIn) were used as the conventional counter electrode (S*). Indium layer was used as a protection layer. The junction design allows measuring the electrical properties of these junctions like resistance on temperature on each electrode and the junctions itself as well as temperature dependent current-voltage characteristics and differential conductance vs. voltage. Josephson junctions are the targeted search for critical currents, $I_c R_N$ -product, microwave and magnetic field dependence and superconducting energy gaps. By determination of the $I_c R_N$ -product, one can get information on the characteristic quality of the JJs.

Additionally, this work includes the preparation of tunneling point contact performed by a different sharp tip of Nb, Au electrode, which is pressed along c-axis of the surface of single crystals.

The observed properties of Josephson junctions showing interesting results are important for basic research as well as for future application. For the characterization of the Josephson effects, the I-V characteristic is fitted within RCSJ-model and the obtained $I_c R_N$ -products may have influenced on the type of barrier. The measured values of high $I_c R_N$ -products increased the possibilities for applications like superconducting quantum interference devices (SQUIDs, Superconducting **Q**uantum **I**nterference **D**evelopes).

2. FUNDAMENTALS

2.1 SUPERCONDUCTIVITY

Superconductivity is a physical phenomenon when the electrical dc resistivity of the material drops to zero at a certain low temperature. The temperature which the material transforms from a normal state to superconducting state is called critical temperature (T_c). In the other word, there is no resistance to the electrical dc current [24]. Therefore at T_c , the specimen presumably undergoes a phase transition from normal state to a superconducting state. T_c differs from one material to another, it should be mentioned that the superconducting materials losing their superconductivity behavior if the current density characteristic of that material was exceeded. This is known as Silsbee effect. The critical current density (J_c) is the critical current per unit area $J_c = I_c/A$.

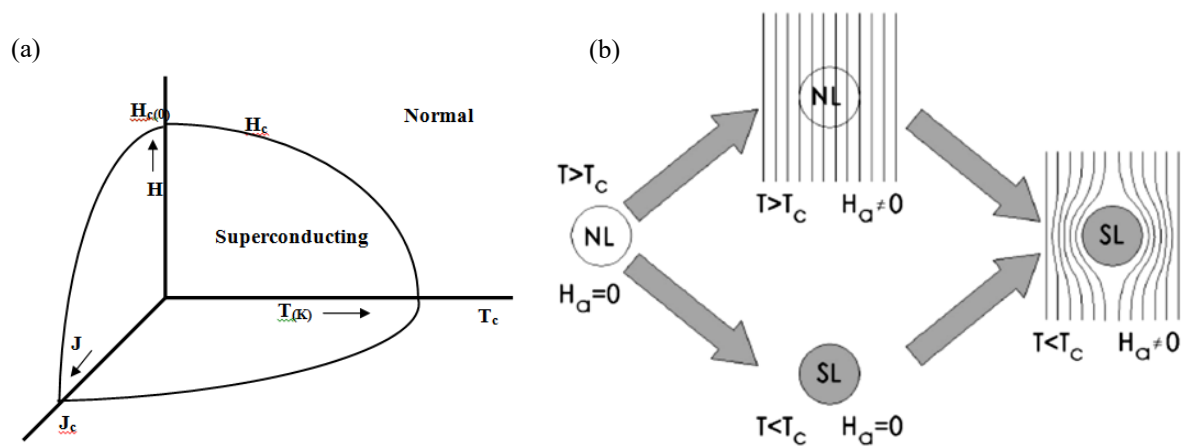


Fig. 2.1.1: (a) The relationship between critical temperature (T_c), critical magnetic field (H_c), and critical current density (J_c). These parameters are a characterization of a superconductor. (b) Meissner effect: a material changes its state from normal metal (NL) to superconductor (SL) under different conditions [25].

The other dominant characteristic is the critical magnetic field (H_c) which is applied on the superconductor, when the T_c of a superconductor is measured in the presence of an applied magnetic field (H), as the magnetic field exceeds a certain value H_c the superconducting state was destroyed and the material behaves like a normal conductor. The dependence of the critical magnetic field on temperature was described by the following formula:

$$H_c(T) = H_c(0)[1 - (T/T_c)^2] \quad (2.1)$$

where $H_c(0)$ is the field at $T=0$ K.

These two quantities (J_c and H_c) characterized together with the fixed T_c , manifest a material as a superconductor. The phase diagram in Fig. 2.1.1 (a) demonstrates the relationship between T_c , H_c , and J_c .

The interesting in superconductivity is that superconductors expel all magnetic flux from its interior by the induction of surface current when it found in an external magnetic field and cooled down which means it becomes a perfect diamagnetism. This phenomenon is known as Meissner effect. That illustrated in Fig. 2.1.1 (b).

According to the two-fluid model (London theory), if a magnetic field is applied in Z-direction and surface specimen of SC laying in the XY plane then an electric field E appears in the superconductor, the superconducting electrons are accelerated without dissipation. This supercurrent around SC specimen produces a magnetic field B inside SC, which cancels the external field. That makes inside the SC, $B=0$ and is the reason for excluding the external magnetic field. In another hand, the magnetic field can penetrate a superconductor surface at a small distance (x) called the London penetration depth (λ_L) and decays exponentially to zero inside the superconductor in accordance with Meissner effect, which illustrated in Fig. 2.1.2. The nature of the decay depends on the superconducting electron density n_s . By using Maxwell equations:

$$\nabla \times B_z(x) = \mu_0 J_s, \text{ Where } J_s \text{ is supercurrent density } J_s = [n_s e^2 / m] \hat{A} \quad (2.2)$$

n_s is the density of superconducting electrons, m is the mass of an electron, \hat{A} is the magnetic vector potential.

We get $\nabla^2 B_z(x) = B / \lambda_L^2$, The solution to the simple differential equation is:

$$B(x) = B_o \exp (-x/\lambda_L) \quad (2.3)$$

$$\lambda_L = \sqrt{(m/\mu_o n_s e^2)}$$

λ_L penetrates the superconductor surface of value depends on the superconductor material and is for HTS anisotropic. While the value of λ_L for FBS is about 200 nm, with this value the record for J_c is calculated about $\approx 16.8 \times 10^{11} \text{ A.m}^{-2}$ [26, 27].

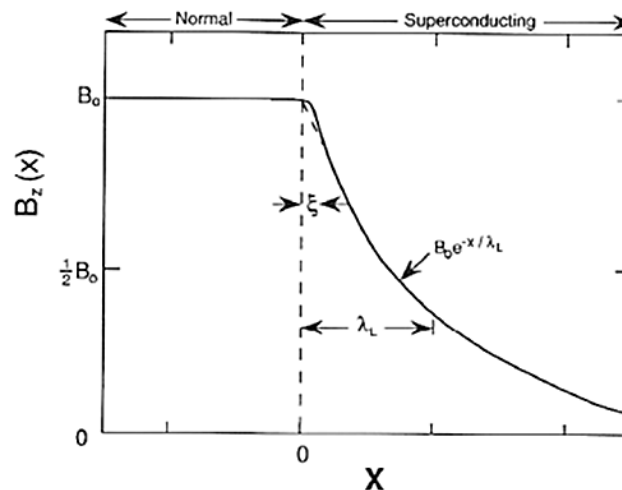


Fig. 2.1.2: Characterizes the distance vs. a magnetic field penetrates inside the superconductor material, Exponential decay of a constant applied magnetic field $B_z(x)$ inside a superconductor for the case $\lambda_L > \xi$. Note the small deviation from exponential behavior within a coherence length ξ of the surface. [25]

There are two different types of behavior for an external magnetic field, which can have occurred when a sufficiently large field is applied, and the superconductors can be divided into two types correspondingly:

Type I can be described below a critical field $H_c(T)$, which decreases with increasing temperature, falling to zero at $T=T_c$, flux does not penetrate the superconductor. This is Meissner effect and called type I. above the critical field H_c , the entire specimen reverts to normal behavior, with perfect flux penetration.

Type II is a second type superconductor which has two critical fields H_{c1} and H_{c2} associated with it. When the applied field is below H_{c1} the flux is excluded. Above H_{c1} there is a partial flux penetration, and the sample consists of both normal and superconducting regions, a state is known as the mixed state, see Fig.2.1.3 (a). In this state, the flux penetrates in the form of flux vortices or flux lines. The penetrated flux lines will be surrounded by superconducting current vortices. That illustrates in Fig.2.1.3 (b). Where the fields penetrate the specimen, the material is normal, but it is superconducting elsewhere. This local normal state can occur even though the temperature below T_c . That is explained there is an overlap in some regions in superconductors. The vortices sometimes called Abrikosov vortices. These vortices carry a flux value of about $\Phi_0 = h/2e = 2.07 \times 10^{-15} \text{ T}\cdot\text{m}^2$ which is known as a flux quantum. The diameter of such a vortex amounts to $2\xi_{GL}$ where ξ_{GL} is the Ginzburg-Landau coherence length. The Abrikosov vortex has occurred naturally in a lattice which is arranged as Triangular vortex lattice. The vortices can be introduced by anchoring (pinning) like defects [28], or generated artificially e.g. It is caused by ion irradiation [29]. The other method is made non-superconducting nanoparticles [30], this leads to a possible increase of maximum supercurrent.

When the value of the magnetic field is above H_{c2} , the superconducting state goes to the normal state. The upper critical field H_{c2} for some type II superconductor can be as high as 100 T and may be much higher for HTS, compared with a critical field of around 10 mT for

type I superconductor. Thus if the applied field is sufficiently large, it will be energetically favorable for the superconductor to revert to a normal state.

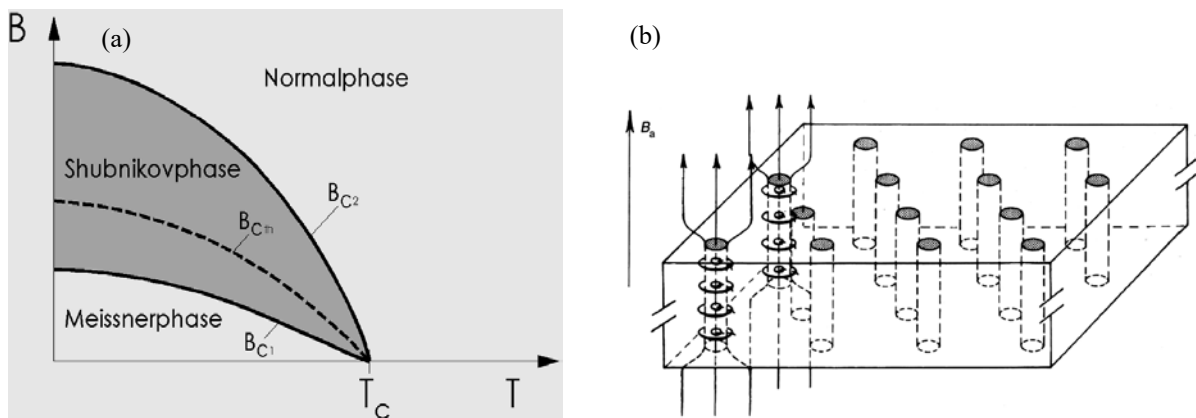


Fig. 2.1.3: (a) Magnetic field behavior of Type-II superconductor. [25] (b) Flow penetration in the form of vortices, Such a distribution of magnetic field lines is expected for a type-II superconductor, i.e. for all high-temperature superconductors (HTS). [25]

An understanding of superconductivity was advanced in 1957 by Barden, Cooper, and Schrieffer. It is known as the BCS Theory [31]. Thus the mechanism behind superconductivity, the idea comes from that two electrons (or holes) pair up, which normally should repel each other by introducing an attractive interaction between them. The answer to this was found to be in phonons, packets of sound waves present in the lattice as it vibrates. In which one electron has wave vector k_1 emit phonon q and changes direction other one k_2 absorbed the phonon and changes own direction, two paired electrons are called Cooper pairs as shown in Fig.2.1.4 (a). This phonon exchange created correlated state between them. Thus BCS theory explained the superconducting current as a super fluid of Cooper pairs.

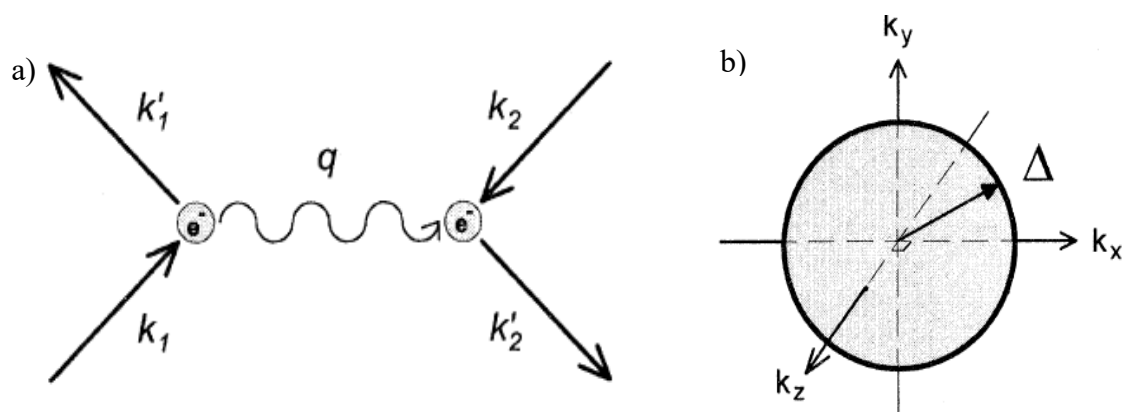


Fig. 2.1.4: (a) Cooper pair: pairing interaction between two electron by a virtual phonon q overall effect [32]. (b) An isotropic s-wave Symmetry of Order parameter OP (Gap Δ in Fig.) [32].

Since the distance between the Cooper pair is very small denoted as the superconducting coherence length (ξ), there is a strong overlap of the individual wave functions and thus to form a total macroscopic wave function of order parameter OP (Ψ_{GL}). Coherence length as an introduction of the Ginzburg-Landau parameter is given

$$\xi_{GL} = (\hbar^2/2m\alpha)^{0.5} \quad (2.4)$$

The coherence length as an introduction according to BCS theory is,

$$\xi = \hbar v_f / \pi \Delta \quad (2.5)$$

Where \hbar is the reduced Planck constant, m : the mass of Cooper pair, α : a development coefficient of the Ginzburg-Landau theory, v_f : the Fermi velocity, and Δ : the superconducting gap.

There is a ratio between λ_L and ξ , which is $k = \lambda_L / \xi$. Type I superconductor related to $0 < k < 1/\sqrt{2}$, and type II superconductor related to $k > 1/\sqrt{2}$.

Considering the superconductivity as a thermodynamic phase can be a similar expression of the free energy density derived. This was carried out under the Ginzburg-Landau theory. So, the Ginzburg-Landau coherence length temperature dependence is:

$$\xi_{GL}(T) = \frac{\xi(0)}{\sqrt{1 - T/T_c}} \quad (2.6)$$

2.2 ENERGY GAP:

A significant energy gap is involved between the energy of a Cooper pair and the energy of two single and unpaired electrons. The energy gap described by BCS theory decrease towards zero as the temperature approach T_c , since the fraction of electrons in paired states decreasing with rising temperature. The total separation between states above and below the gap is conventionally described as $2\Delta(0)$ at zero temperature or $2\Delta(T)$ for finite temperature. BCS theory provides an integral equation $\Delta(T)$. Most equations for superconducting properties can be described by a dimensionless ($\Delta(T)/\Delta(0)$) versus (T/T_c) dependence. Fig. 2.2.1 shows temperature dependence of the energy gap.

The BCS theory provides thereby the equation for the temperature dependence of the gap of superconductors:

$$\Delta(T) = \Delta(0) \tanh(1.74\sqrt{T_c/T - 1}) \quad (2.7)$$

$$\Delta(0) \approx 1.76 k_B T_c$$

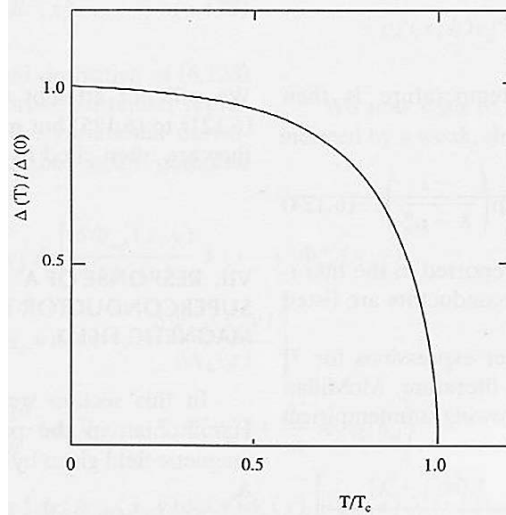


Fig. 2.2.1: Temperature dependence of the energy gap. The temperature is normalized to the critical temperature and the energy gap to the energy gap at 0K. [25]

Thus below a certain temperature of the superconducting phase would be happened that couple two electrons (holes) near the Fermi energy (E_F) to a Cooper pair. Thus the transition to the superconducting phase condenses these Cooper pairs. Due to their spin bosons of Cooper pairs, this would form a coherent quantum state. All of them could be described by the same wave function which is as an order parameter for the superconducting phase. The corresponding macroscopic wave function has the form (Ψ).

Now phases are described by order parameter which is the wave function of these Cooper pairs. Fig. 2.1.4 (b) shows the s-wave superconducting gap having an isotropic magnitude in all direction the momentum space (k), which is standard for BCS theory. Superconducting order parameter can be expressed at

$$\Psi = \Psi_0 \cdot \exp(i\varphi) \text{ or } \Delta = \Delta(k) \cdot \exp i\varphi(k) \quad (2.8)$$

$|\Psi| = \Delta \Rightarrow$ symmetry $\Psi(k)$ is symmetry of $\Delta(k)$ which is the magnitude of superconducting gap. That means the required magnitude to break up the cooper pair. $\Phi(k)$: The phase of the order parameter.

This also can be generally described by the magnitude Ψ_0 and phase of φ corresponding to n_s :

$$\Psi(\vec{r}, t) = |\Psi_0(\vec{r}, t)| \cdot e^{i\varphi} \quad , \quad |\Psi_0(\vec{r}, t)| \sim \sqrt{n_s} \quad (2.9)$$

The absolute magnitude of the wave function is, therefore, an indication of the Cooper pair density of states in the superconductor (n_s).

Three different symmetries of the OP are shown in Fig. 2.2.2 which contains isotropic s-wave (a), anisotropic s-wave without changing in sign (b), and d-wave sign change under 90° rotation (c).

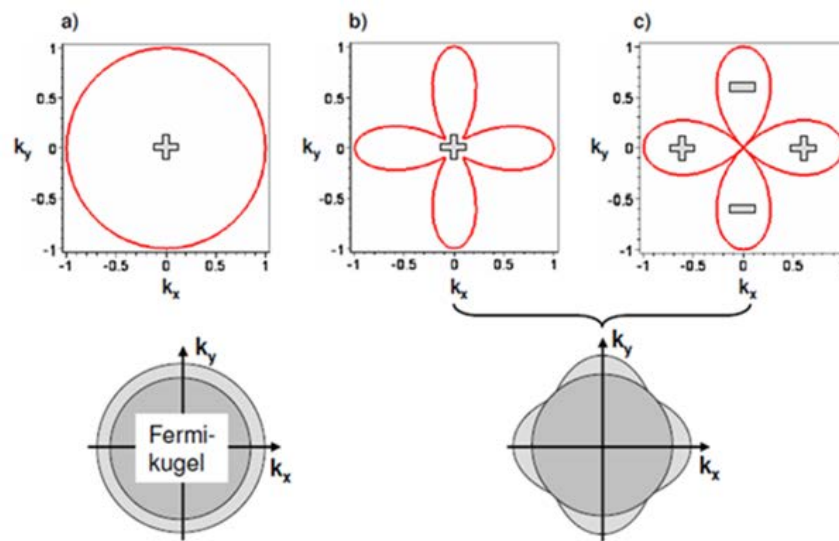


Fig. 2.2.2: Symmetry of OP: a) Isotropic s-wave, “Fermi Kugel” is written in the German language which means Fermi Sphere. (b) Anisotropic s-wave invariant under 90° rotation, no sign change. (c) d-wave sign change under 90° rotation. [33]

2.3 IRON – BASED SUPERCONDUCTORS

Iron pnictides are a new family of unconventional superconductors, which were discovered by a group of scientists at the Tokyo Institute of Technology. Since the date of discovery, many researchers with extensive effort have been directed characterizing and modeling the novel properties of these exotic materials of iron-based superconductors (FBS). First result was reported on FBS in 2006 with the discovery of superconductivity in LaFePO [1] and LaNiPO [34, 35] below 5 K. Two years later, the T_c raised up to 26 K with the fluoride doped arsenide LaFeAs(O_{1-x}F_x) [36]. It followed the record of T_c increasing up to 55 K when La was replaced by another rare-earth element SmFeAs(O_{1-x}F_x) [2, 37-38]. Since this last mentioned of T_c , they gained much greater attention. In 2014 the record T_c in this family is about 100 K found in mono-layer FeSe thin films on STO substrate producing some unknown interface effect [39]. Furthermore, these compounds can be classified into four main phases which are “1111” phase RFeAsO (R: the rare earth element), “122” type AFe₂As₂ (A: the alkali or alkali earth) “111” type BFeAs (B: the earth alkali metal) and FeSe type “11”. Those common classifications are named after the stoichiometry of their parental prototypes. The crystal structure of these compounds is shown in Fig. 2.3.1, all shares in the same plane of FeAs (FeSe for the first one), which is the intrinsic for the appearance of superconductivity. Thus the superconducting electrons in all FBS flow in the planes that have iron.

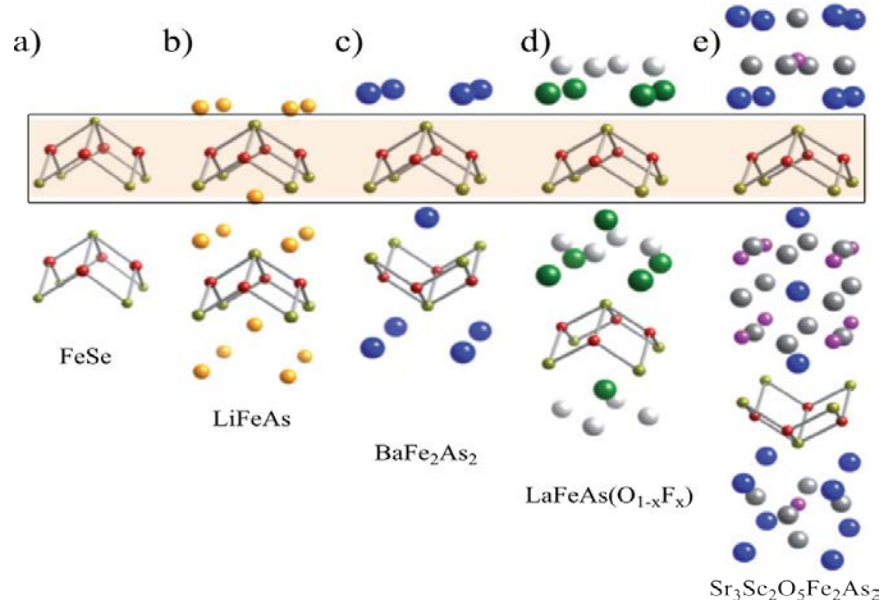


Fig. 2.3.1: Crystal structure of the different classes of FBS. All of these FBS contain FeSe or FeAs building blocks (the iron ions are shown in red and the pnictogen/chalcogen are shown in gold) [40].

The raising of T_c is not the only reason of their interested properties but there are other unique properties belong to FBS such as robust to impurities, high upper critical field, high critical density [4,26,27], and anisotropic crystallography. That it is shown in table 2.3 and a comparison is summarized with those of cuprates and MgB_2 . Furthermore, FBS are interesting material because of multiple gaps and unconventional symmetry. Up to now, there is no consensus on its symmetry which the supposed superconducting pairing symmetry in FBS is s_{\pm} -wave. But there are many papers with a different evidencing suggestion for the type of order parameter symmetry, such as in Refs. [41-43] are nodeless s_{\pm} symmetry, *i.e.* the term “unconventional pairing” used. Other display nodes in the gap structure (nodal s_{\pm} symmetry) [6]. The other literature presents s_{++} symmetry [7], and even d-wave [8]. It may be a possible reason for that the FBS has band structure which is a multiband nature. The multiband superconductivity with a sign reversal between electron and hole pockets that have been suggested to happen from a magnetic coupling between electron and hole pockets at the Fermi surface. The pairing interaction may be mediate by magnetic excitations. This above explanation may lead to a reason for a sign changing of s_{\pm} symmetry of the order parameter [5]. A reason for s_{++} symmetry may belong to orbital fluctuation without π -phase shift between different bands [7]. The reason for those compounds which have nodal s_{\pm} -wave is described as ‘accidental nodes’ by a disorder of doping. Fig. 2.3.2 (a) shows the four different order parameters in the FBS represented in the 2D 1-Fe Brillouin zone. Different colors represent different signs of the gap.

Fig. 2.3.2 (b) shows the calculation of band structure for a compound of FBS “LaFeAsO”, which illustrated two or more hole bands crossing the Fermi level near Γ point and two electrons bands near the M point. Γ , M, Z, R points symmetry on the Brillouin zone (BZ) are given particular.

Table 2.3: Physical properties of iron-based superconductors with those of cuprates and MgB_2 . [44]

	Iron Pnictides	Cuprates	MgB_2
Parent materials	Antiferromagnetic metal (semi-metal)	Mott insulator	Metal
Fermi level	5 bands	Single band	2 bands
Pairing symmetry	s-wave	d-wave	s-wave
Impurity	Robust	Sensitive	Sensitive
Max T_c	55 K	134 K	39 K
$B_{c2}(0\text{ K})$	100–250 T	~100 T	40 T
γ (Anisotropy)	1–2 (122)	5–7(YBCO); 50–90 (Bi-based)	~3.5

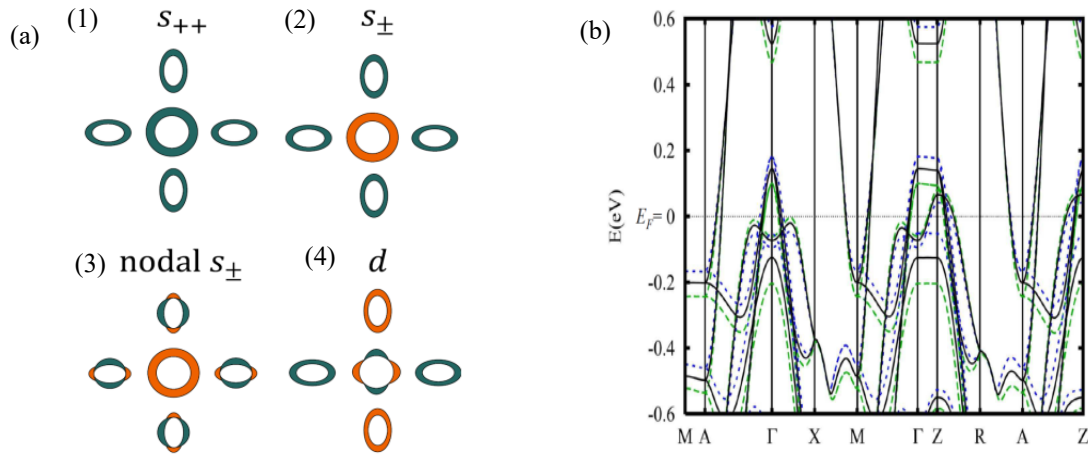


Fig. 2.3.2: a) Schematic pictures of the proposed order parameters in the iron-based superconductors represented in the 2D 1-Fe Brillouin zone. (1) s_{++} -wave symmetry, (2) s_{\pm} -wave symmetry, (3) Nodal s_{\pm} -wave symmetry, and (4) d-wave symmetry. Different colors stand for different signs of the gap. Electron is (green) and hole is (orange) [46]. b) The calculation of band structure for LaFeAsO [47].

The crystal structure of FBS is a crystal lattice of FeAs which contains from two square lattice planes of As which form above and below the square lattice of Fe, Fig. 2.3.3 (a) shows the arrangement of As creates unit cell twice 1-Fe unit cell. The corresponding 2- Fe Brillouin zone is twice as small as the 1-Fe unit cell that called folded BZ.

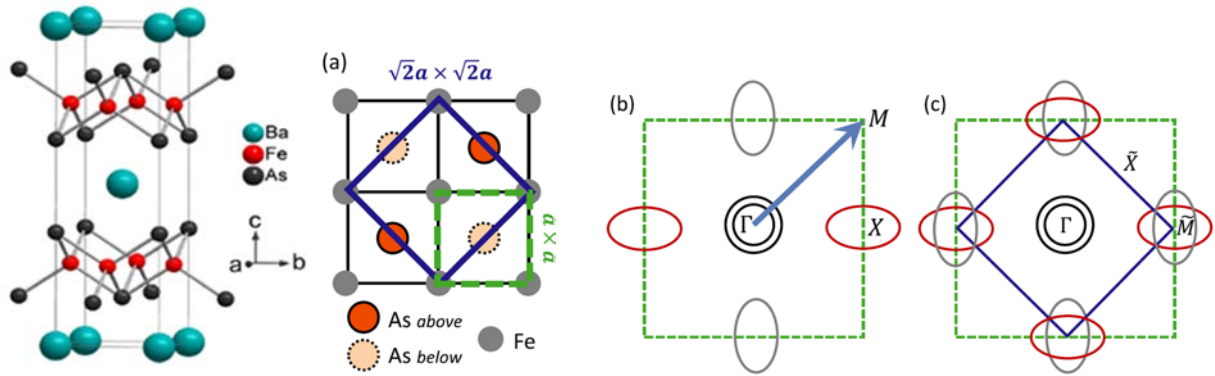


Fig. 2.3.3: Left: structure of BaFeAs. [45]. (a) FeAs lattice indicating As above and below the Fe plane. Dashed green and solid blue squares indicate 1- and 2-Fe unit cells, respectively. (b) Schematic of Fermi surface in the 1-Fe BZ whose boundaries are indicated by a green dashed square. The arrow indicates folding wave vector Q . (c) Fermi sheets in the folded BZ whose boundaries are now shown by a solid blue square. [46]

2.4 JOSEPHSON JUNCTIONS

In 1962, Brian Josephson predicted that the theoretical phenomenon of tunneling of copper pairs results in a current across an insulating barrier between two superconductors [48]. Josephson awarded a Nobel Prize in 1973 [49] for his prediction of the Josephson effect. A Josephson junction using a barrier layer between two superconductors which can be an insulator (I), normal metal (N) and construction (c) that lead to behavior SIS, SNS and ScS respectively. The barrier can be also a semiconductor, disturbs superconductor or any combination of these. In such cases there are other possible mechanisms occur like Andreev reflection or proximity effect. A result from these junctions' behaviors will be a nonlinear current-voltage characteristic (I-VC) of a Josephson junction which is described through the macroscopic wave functions. Where Cooper pairs behavior is described by macroscopic wave functions (Ψ_1 and Ψ_2) in which n_1 and n_2 represent the density of cooper pairs respectively for S1 and S2. The current through this junction depends on the phase angle ϕ which is the difference between the phases in the two superconductors $\phi = \phi_2 - \phi_1$ where ϕ_1, ϕ_2 are for S1 and S2 respectively. A scheme of a junction is shown in Fig. 2.4.1.

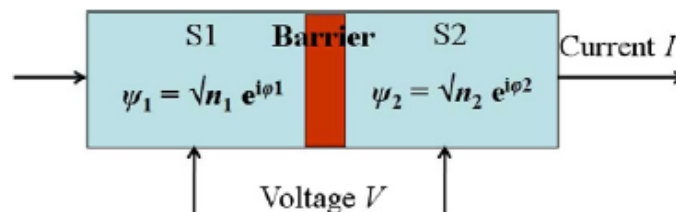


Fig. 2.4.1: A Josephson junction using a barrier layer between two superconductors [51].

Experimental observation of the Josephson effect was first made by Anderson and Rowell [50]. The properties of Josephson junctions and their typical I-VC suggest that it is the source of several important applications in various fields of human activity; from medicine to computer technology [51]. Fig. 2.4.2 illustrated some different structure of Josephson junctions [52].

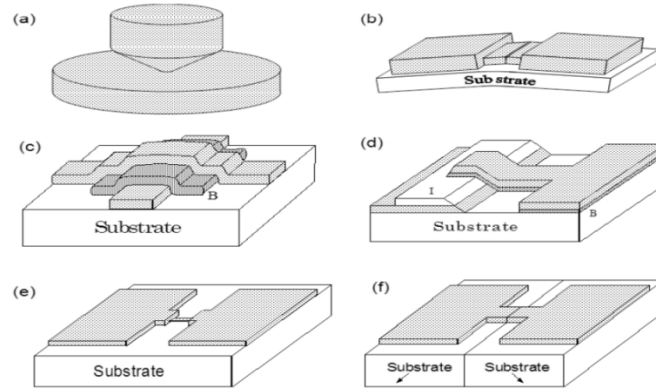


Fig. 2.4.2: Different junctions geometry where Josephson effect can take place. : (a) point contact, (b) break junction, (c) junction with crossed electrodes and barrier (B), (d) edge junction with barrier (B) and insulator layer (I), (e) nanobridge, and (f) bicrystal grain boundary junction. [52]

When it comes to the temperature dependence in the tunneling Josephson junction (SIS), it could be discussed and given by Ambegaokar and Baratoff [53, 54] as follows:

$$I_c(T) = \frac{\Delta_1(T)\Delta_2(T)\pi}{R_N\beta} \sum_{l=0,\pm 1,\dots} \frac{1}{\sqrt{(\omega_l^2 + \Delta_1(T)^2)(\omega_l^2 + \Delta_2(T)^2)}} \quad (2.10)$$

With

$$\omega_l = \frac{\pi(2l+1)}{\beta} \quad \text{and} \quad \beta = \frac{1}{k_B T}$$

Where in R_N is the normal resistance, k_B is Boltzmann constant, $\Delta_1(T)$ is the gap temperature dependent of the first superconductor and $\Delta_2(T)$ gap of the second superconductor. This can be seen in Fig. 2.4.3 that the curve depends on the ratio of gap energy.

The measured temperature dependence of Josephson critical current compared with the calculation of Ambegaokar and Baratoff, where the bottom curve shows (Sn/Sn) the case of two identical superconductors ($\Delta_1 = \Delta_2$). The second upper curve shows a lead-tin junction contact (Pb/Sn), their superconducting energy gaps is applicable to $\Delta_1(0)/\Delta_2(0) = 0.5$.

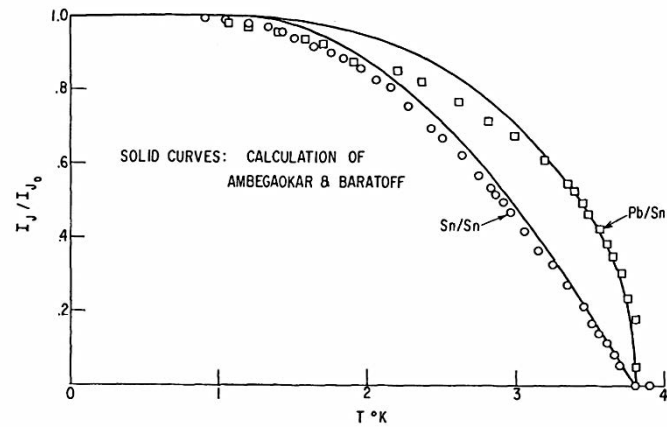


Fig. 2.4.3: The temperature profile of the critical Josephson current. The solid lines followed calculations of Ambegaokar and Baratoff, open symbols show experimental results from Fiske [55]

2.5 JOSEPHSON EQUATIONS

Josephson investigated the behavior of two weakly coupled superconductors on the basis of the microscopic theory of superconductivity by Bardeen, Cooper, and Schrieffer (BCS) [31] a few years after its publication. He predicted two main effects due to the tunneling Cooper pairs of superconducting electrons across the junction, i.e. a coupling of the macroscopic wave functions of the two superconductors.

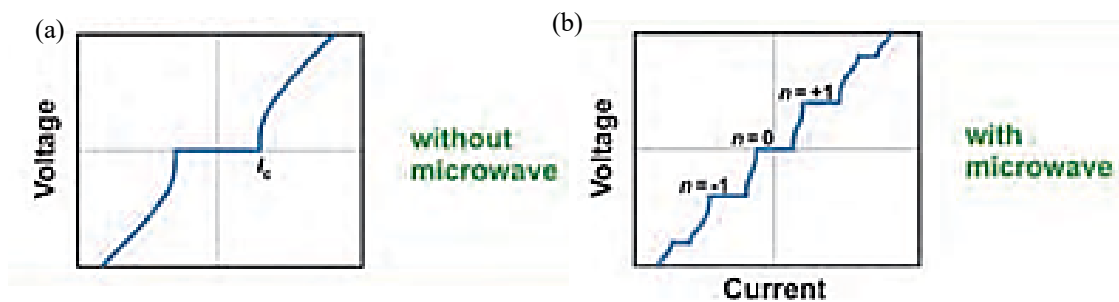


Fig. 2.5.1: schematic I - V characteristics without microwave (a), with a microwave (b). [51]

2.5.1 D.C EFFECT

The first equation describing the Josephson effect is the current-phase relation [48], as illustrated in the following equation below:

$$I_s = I_c \sin \varphi \quad (2.5.1)$$

Where I_s is the total supercurrent through a junction, φ ($\varphi = \varphi_2 - \varphi_1$) is the difference between the phases in the two superconductors as it mentioned and explained in the previous section.

For tunneling junctions with a small transmission coefficient of the insulating barrier, there is sinusoidal phase dependence. When the voltage difference between the superconducting electrodes is zero; the current can flow across the insulating barrier. The supercurrent (Josephson current) has a maximum value which is called the supercurrent amplitude or the critical current (I_c) of the Josephson junction. See Fig. 2.5.1 (a).

The supercurrent depends on the phase difference between the Cooper pair wave functions of both superconducting electrodes. This effect is known as the dc Josephson effect.

2.5.2 A.C EFFECT

The second equation describing the Josephson effect is the phase difference increases with time if an external voltage (V) is applied between the two superconductors or by feeding a junction by a bias current higher than the critical Josephson current.

$$d\phi/dt = (2e/\hbar)V \quad (2.5.2)$$

From equations (2.5.1) and (2.5.2) it can be obtained

$$I_s = I_c \sin ((2e/\hbar) V \cdot t) \quad (2.5.3)$$

It means that there is an alternating current within the junction (ac Josephson effect) with the junction frequency (ω) given by [31]:

$$\begin{aligned} d\phi/dt &= \omega = (2e/\hbar)V \\ \omega &= (2e/\hbar)V \end{aligned} \quad (2.5.4)$$

Where e is elementary charge and h is Planck's constant.

2.6 I-V CHARACTERISTICS OF JOSEPHSON JUNCTIONS

Because a nonlinear current – voltage behavior occurs in Josephson devices, that brought many important applications. Current properties in the active region of the junction do differ in different cases. Thus it was analyzed and described by Stewart and McCumber [56, 57]. It named after of their names or RCSJ-model (**R**esistively **C**apacitively **S**hunted **J**unction). We will discuss two cases in the next sections.

CASE 1: RSJ-MODEL

Here is the discussion of the I-V characteristic of a Josephson junction using a circuit which is represented in the equivalent circuit model in Fig. 2.6.1 (a), which is a Josephson

junction (J) in parallel with a resistance (R). Therefore the resistor acts as a shunt. The result of nonlinearity for this I-V characteristic is the characteristic voltage $V_c(T) = I_c(T)R_N$, where R_N is calculated at 4.2 K. A Josephson supercurrent flows up to I_c at $V = 0$. A transition occurs from the $V = 0$ state to a finite voltage state for $I > I_c$. Above this voltage, the I-V characteristic exhibits asymptotically to a linear behavior. The characteristic frequency is $\omega_C = (2e/\hbar)I_c R_N$.

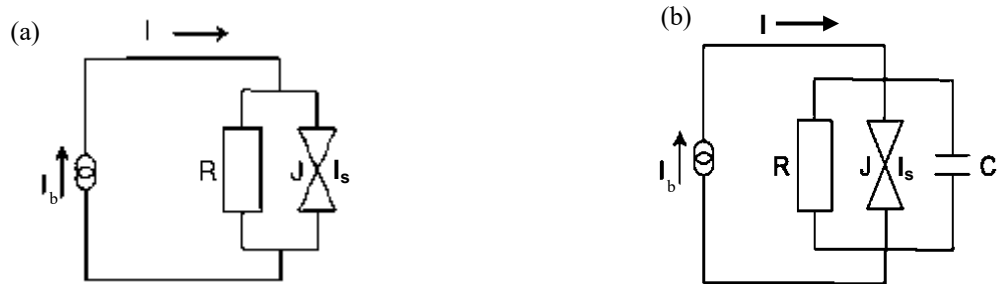


Fig. 2.6.1: Equivalent circuit diagram of a Josephson junction in (a) The resistively shunted Josephson junction RSJ model and b) The resistively and capacitively shunted Josephson junction RCSJ consisting of a power source with the bias current I_b , the Josephson junction (J) and Josephson current I_s , a capacity C , and an Ohmic resistance R .

As briefly way we present equations regarding this circuit. The sum of current across the circuit is given by

$$I = V/R_N + I_c \sin\phi \quad (2.6.1)$$

Where the first term is the Ohmic current, the second term is the Josephson current. In this case, it is considered, the followed equation will be used

$$\hbar (d\phi/dt) = 2e \cdot V \quad (2.6.2)$$

From eq. (2.6.2) we get

$$I = \hbar (d\phi/dt) / 2e R_N + I_c \sin\phi \quad (2.6.3)$$

$I > I_c$ the growing phase is with time and voltage becomes a no vanishing value. This is for $\beta c = 0$ introduced in eq. (2.6.8), the solution for the time-averaged voltage is

$$V = R_N (I^2 - I_c^2)^{1/2} \quad (2.6.4)$$

The I - V curve shows no hysteresis.

CASE 2: RCSJ-MODEL

Now in this mentioned case, it is used for modeling of resistively and capacitive shunted Josephson junctions. The junction with a critical current I_c is assumed to be parallel to an ohmic resistance R_N and a capacitance C . The circuit is shown in Fig. 2.6.1 (b). The total of current across the junction is given by

$$I = I_s + I_R + I_{Cap} \quad (2.6.5)$$

I_R , I_s and I_{Cap} represents normal, junction, and capacitance current, respectively. With substituting by Josephson equations that were described in section 2.5.1 and 2.5.2 respectively and subsequence calculations have resulted;

$$I = I_c \sin\varphi + V/R_N + C \cdot dV/dt \quad (2.6.6)$$

The Josephson supercurrent is the first term in the equation above, the following term is of the normal conduction part $I_R=V/R_N$, and the last part is the current through the capacitor $I_{Cap}=\hbar C/2e \cdot (d^2\varphi/dt^2)$ respectively. By substitution in eq. (2.6.5) is resulted below;

$$I = I_c \sin\varphi + \hbar/2eR_N \cdot (d\varphi/dt) + \hbar C/2e \cdot (d^2\varphi/dt^2) \quad (2.6.7a)$$

Eq. (2.6.7a) placed in a dimensionless form thus it obtained:

$$i_b(\tau) = \sin\varphi + \dot{\varphi} + \beta_C \ddot{\varphi} \quad (2.6.7b)$$

Where the following normalization parameters were used in eq. (2.6.7a), $i_b(\tau)=I/I_c$, $\dot{\varphi}=d\varphi/d\tau$, $\tau=t\omega_c$, $\omega_c=2eI_cR_N/\hbar$, and $\beta_C=2eCI_cR_N^2/\hbar$. Again the important parameter $I_c(T)R_N$ is the characteristic voltage $V_c(T)=I_c(T)R_N$.

ω_c , and β_C are the characteristic Josephson frequency of contact, and the McCumber parameter, respectively.

$$\beta_C = 2eCI_cR_N^2/\hbar \quad (2.6.8)$$

One has to distinguish a limit with respect to the so-called McCumber parameter. In Fig. 2.6.2 (a) shows different values of β_C starts with smaller black one followed increased gradually, when McCumber parameter has to be small $\beta_C < 1$ the I-V characteristics show non hysteretic behavior, see case 1 (RSJ model for $\beta_C=0$).

$\beta_C > 1$ or $I < I_c$ then the I-V characteristics becomes a hysteresis. As it is shown in Fig. 2.6.2 (b), when a current is below I_c , we get an unstable region which is illustrated as the current starting from zero until it will be reached the critical current I_c so that we do not have any voltage drop across the junction, At I_c value, the voltage is changing from zero to a finite value. This behavior is used to be in the Josephson devices. In the reverse direction, when the current decreasing below I_c , a resistive state occurs even at current values below I_c , (we called it the return current I_R) then the I_R returns to its normal behavior $I_R(V=0)$. The McCumber parameter, in that case, is possible to calculate by using hysteresis characteristics, from the ratio of return current I_R and the I_c can be estimated McCumber parameter by:

$$I_R/I_c = 4/\pi \cdot (\beta_C)^{1/2} \quad (2.6.9)$$

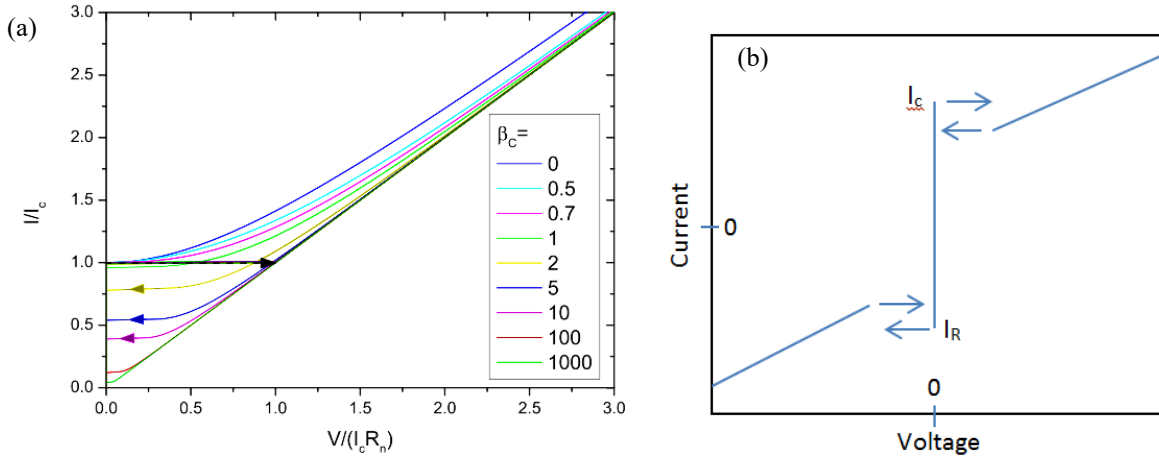


Fig. 2.6.2: (a) I - V characteristics curves calculated for different values of β_C according to equation (2.6.7b) [59]. (b) Schematic I - V characteristics for hysteretic Josephson junctions ($\beta_C > 1$).

I - V characteristic often can be influenced under realistic conditions, and gets smeared out around I_c due to a thermal noise current I_f . By introducing a thermal noise current I_f into Eq. (2.6.7b) the problem is managed [59].

$$V = \frac{2I_c R_N}{\gamma} \frac{e^{\pi\gamma i_b} - 1}{e^{\pi\gamma i_b}} T_1^{-1} \left(1 + \beta_C \frac{T_2}{T_1} \right) \quad (2.6.10)$$

$$\text{With } \gamma = \frac{\hbar I_c}{ek_B T_n}, T_1 = \int_0^{2\pi} \frac{J_0 \gamma \sin(\theta/2)}{e^{\pi\gamma i_b \theta}} d\theta$$

$$\text{And } T_2 = \int_0^{2\pi} \sin(\theta/2) \frac{J_1(\gamma \sin(\theta/2))}{e^{\pi\gamma i_b \theta}} d\theta$$

Here, J_n is the modified Bessel function of the n -th order and T_f is the effective noise temperature.

In a case of real measurements, I - V characteristics show asymmetry and an additional excess current. Both issues can be included in the RCSJ model by assuming the parameters are asymmetric. It can assume different parameters γ , I_c , β_C , and R_N for positive and negative currents, respectively. The possible reason for such effect can be an influence of trapped flux in the junction, but it can also be made happen by the multiband behavior of pnictides [60]. The effect of an excess current I_{ex} , can be placed in the model by replacing i_b in eq. (2.6.7b) by the following relation.

$$i_b = (I - I_{ex}) / (I_c - I_{ex}) \quad (2.6.11)$$

2.7 INVERSE A.C EFFECT (MICROWAVES DEPENDENCE)

Irradiation of the Josephson junction with an electromagnetic wave of an external frequency $\omega_{mw}=2\pi f_{mw}$, leads to a resonance effect between the external and the natural frequency of the junction which are manifested by the fact that occur in the characteristic curve to steps.

Thus it would have happened that the I-V characteristics shows clear steps, with constant voltage spacing values, See Fig. 2.5.1 (b). This is a created constant voltage step called Shapiro steps. This gives impression such as a series of resonances exist in the junction. These appeared resonances are at the frequencies $m/n\omega_c$ with $\omega_c=2eV_o/\hbar$ as the characteristic frequency. This is the basis of the voltage standard. Thus the frequency and the voltage are related only via natural constants by $f/V=K_J$. Where $K_J=2e/h$ named the Josephson constant, that is equivalent to $483597.870(11) \times 10^9 \text{ HzV}^{-1}$.

$$V_n = n (h/2e)f_{mw} = n \Phi_o f_{mw} , n=0,1,2\dots \quad (2.7.5)$$

Where n is an integer, Φ_o is flux quantum equals $h/2e$, f_{mw} is the radiation frequency. This effect is called inverse ac-Josephson Effect.

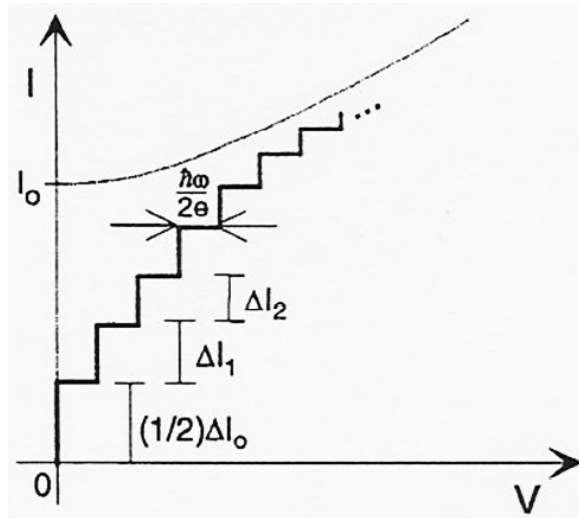


Fig. 2.7: Josephson junctions under irradiation of applied microwave wave showing Shapiro steps (schematic) [25].

The height of the n-th step of the current region ΔI_n , in which the voltage remains constant, that can be approximated to Bessel behavior and is calculated from

$$\Delta I_n = 2 I_c |J_n(A)| \quad \text{With } A = i_m/\Omega \sqrt{1 + \beta_c^2 \Omega^2} \quad \dots \quad (2.7.6)$$

Where J_n is Bessel function, Ω is the normalized frequency (relative frequency) $\Omega = \omega_{mw}/\omega_c$.

This can calculate by numerical solution of the extended RSJ equation (2.6.7b), see 2.6

$$\beta_c \ddot{\varphi} + \dot{\varphi} + \sin \varphi = i_o + i_m \sin \Omega \tau \quad (2.7.7)$$

$$\Omega = \omega_{mw}/\omega_c, \Omega = h/2e * f_{mw}/I_c R_N \quad (2.7.8)$$

Where the dots above phase difference is the derivation with τ the normalized time $\tau = \omega_c t$, $\omega_c = 2eI_c R_N/\hbar$. β_c is the McCumber parameter $\beta_c = 2eCI_c R_N^2/\hbar$. i_o, i_m are biasing dc current and the normalized amplitude of microwave current respectively.

2.8 JOSEPHSON JUNCTION IN AN EXTERNAL MAGNETIC FIELD

The magnetic field dependence is an interesting aspect of a fundamental effect in a Josephson junction, which is by applying parallel magnetic field⁽¹⁾ on a junction barrier. The magnetic field can penetrate the barrier of thickness (t) and two superconducting electrodes at the London penetration depth⁽²⁾ of the two superconducting electrodes ($\lambda_{L1}, \lambda_{L2}$), respectively. Therefore the actual thickness barrier (t) of the range is in which the magnetic field penetrates the contact. It is approximately by

$$t^* = t + \lambda_{L1} + \lambda_{L2}$$

Let us assume that the supercurrent density (J) passes inside a homogeneous junction. The Josephson relation can be written as

$$J(y, z) = J_c(y, z) \sin \varphi(y, z) \quad (2.8.1)$$

φ is a function of time and space coordinates in the plane of the junction. $J_c = I_c/WL$ (with contact width (W) and layer length (L)) is the critical current density of the junction and has unit of A/cm^2 . Under the condition $t \ll \lambda_L$ as well as the other dimensions of the contact $W, L \gg \lambda_L$, and the magnetic field (B) is directed in y direction,

$$\partial \varphi / \partial z = 2 e t^* B / \hbar \quad (2.8.2)$$

The resulted of a sinusoidal current-phase relationship and a homogeneous distribution of the critical current density give an induction the magnetic field dependence of the critical current of the amount of the sinus function. Thus this effect shows the critical current I_c of a Josephson junction is a maximum value for zero magnetic field and suppressed with applied magnetic field. Thus it appears like a Fraunhofer pattern as shown in Fig. 2.8. That may lead to prove the first current-phase relation of Josephson's equation, see section 2.5, P.16.

⁽¹⁾The strength of the applied magnetic field should be here less than the critical magnetic field B_{c1} and B_{c2} of a superconductor, above which the materials leave their superconducting state.

⁽²⁾The London penetration depth (λ) indicates a value of some nanometer, which is the typical value for conventional superconductor like Pb and Nb of about 39 nm, 85 nm [25], respectively. While the typical value for unconventional pnictide superconductor like K-doped: Ba-122 is $\lambda = 200$ nm [108].

$$I_c(\Phi) = I_c(0) \left| \sin\left(\pi\frac{\Phi}{\Phi_0}\right)/\pi\left(\frac{\Phi}{\Phi_0}\right) \right| \quad (2.8.4)$$

Here, (Φ) is the superconducting flux quantum $\Phi = t^*BL$, $I_c(\Phi)$ is the modulation of critical current as a function of the magnetic flux while the total critical current (max. value) is $I_c(0)$ with zero magnetic field.

The Josephson penetration depth (λ_J) can be given by equation below with $\Phi_0=2\lambda_L BL$

$$\lambda_J = \sqrt{c\Phi_0/16\pi^2\lambda_L J_c} \quad (2.8.5)$$

Magnetic field measurements play an important tool for the characterization of junction quality because the spatial critical current distribution $J_c(x,y)$ differs from the expected behavior. Such deviations might be due to an inaccurate definition of the junction geometry (*i.e.* patterning problems) or spatial inhomogeneity in the tunneling barrier. It also may evidence for symmetry of superconducting order parameter, that fulfilled by fabrication phase sensitive measurements, see section 5.2.3.

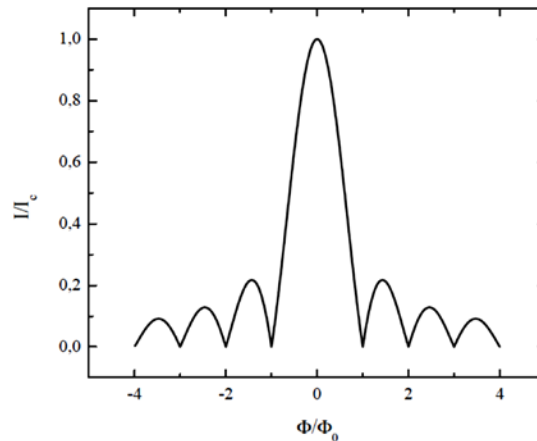


Fig. 2.8: Ideal magnetic field dependence of the critical current for Josephson junctions.

2.9 SPECTROSCOPY

A spectroscopy measurement is an important task to probe the interaction mechanisms between electrons and phonons as well as to characterize the properties such as the energy gaps and the symmetry of the order parameter in superconductor materials, in particular, the recent discovered of iron pnictide materials. Andreev reflection, tunneling, and Josephson Effect measurements are excellent experimental methods, which can give an indication of these properties.

In case two metals (NN) brought together, between them an insulator barrier the current will pass through this insulator barrier (tunneling current). Other group observed that NN is fabricated in micro constrictions way that shows nonlinearities in I-V characteristics and in second derivative d^2V/dI^2 [61].

When it comes to one side superconductor NS, The expected behavior will be observed much stronger than before in nonlinearities I-V characteristics and shows a feature curve in first derivative dV/dI which give the indication of the energy gap in the superconductor.

2.10 ANDREEV REFLECTION AND TUNNELING SPECTROSCOPY

The possible structure, in this case, is point contact Andreev reflection (PCAR). The contact made between two electrodes which are a normal metal and superconductor. The spectroscopies of PCAR provide energy spectroscopy in the low temperature range below the critical temperature of the superconductor material. Spectroscopy is taken from point contact in normal state and analysis by different regime such as ballistic (no scattering), thermal, and intermediate regime, regimes depend on Knudsen ratio $K = l/a$ where (l) is the electron mean free path and (a) is the contact radius, the ballistic condition can fulfill when $a < (l, \xi)$, in case $a > (l, \xi)$, see more description in Ref. [61].

PCAR in the superconducting state, the spectroscopy of the conductance (dI/dV) curves can be discussed theoretically by the Blonder, Tinkham, and Klapwijk (BTK) model. This model includes the effect of a finite transparency of the interface (represented barrier) via the dimensionless parameter (Z).

The Blonder, Tinkham, and Klapwijk (BTK) model [62] has been established as a theoretically model to discuss this phenomenon to identify the pairing symmetry as well as the surface electronic states. The BTK model has been thereafter extended to various situations, which is found to be more suitable for unconventional superconductors. In terms of the recent discovery of iron pnictide materials, also there is a Golubov model [63], which was developed and calculated spectra for different contact parameters of the multiband superconductor.

Through BTK model, this model calculated at $T = 0$, the electron comes from the N to S side can occur different possible processes at an N-S interface:

These possibilities associated to a dimensionless parameter (Z), a thin barrier of the form a repulsive potential $U = U_0 \delta(x)$ assumed by the dimensionless parameter. Z means contamination or thick oxides layers and even relatively degrade on the surface. Therefore case $Z = 0$ or small is more transparent corresponds to AR, large Z goes the case of the tunnel regime.

$$Z = U_0 / \hbar v_F, \text{ Transparency } \tau_N = 1 / (1 + Z^2)$$

τ_N transparency of the barrier. In this is in case the current injection is perpendicular to the interface.

Second association is applied voltage related to energy gap Δ in the superconductor.

- 1- An electron coming with an applied voltage $eV < \Delta$ to the interface between NS and forms with an electron a Cooper pair. The electron leaves behind a hole in the normal conductor in which the move is in opposite direction wherein the net current flows across the

interface $2e$, to correspond thus a Cooper pair. This possibility of Andreev reflection is suppressed with increasing Z .

- 2- Specular reflection is increased with Z .
- 3- Electrons approaching the interface with $eV > \Delta$ are transmitted as electron like quasiparticle (ELQ) or hole like quasiparticle (HLQ) the probability decrease if Z increases but it is always zero for $eV < \Delta$

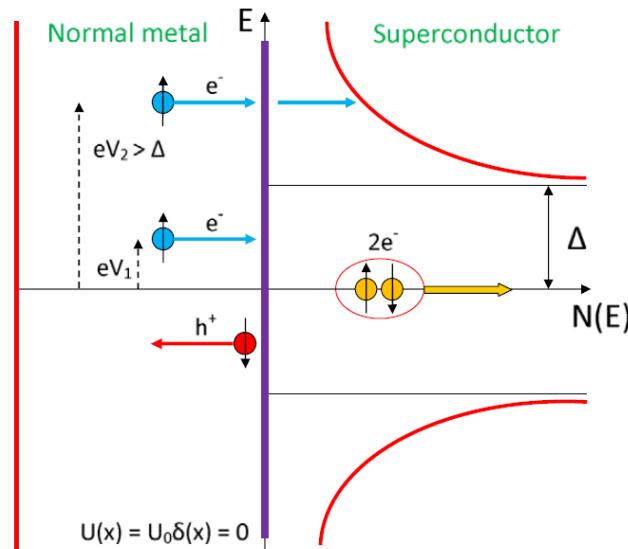


Fig. 2.9: Andreev Reflection, N/S interface at $T = 0$. [61]

The probabilities of these processes depend on the energy of the electron. $A(E)$ and $B(E)$ are the coefficients of the probability of Andreev reflection and ordinary reflection, respectively.

$1 + A(E) - B(E)$ is considered by $T(E)$ which is the transmission probability of the critical current.

The total current propagates across NS

$$I_{NS} = I_0 \int_{-\infty}^{\infty} [f(E - eV) - f(E)] [1 + A(E) - B(E)] dE, \quad f(E) = 1/(1 + \exp \frac{E}{kT})$$

Where I_0 is constant depend on junction area, density of state, the Fermi velocity $f(E)$ is the Fermi distribution function.

By measuring the I-V characteristics of this junction or by measuring the differential resistance (dV/dI), the energy gap can be determined. The normalized conductance G (dI/dV) can be calculated by dividing the conductance junction in superconductor state on normal state, $G_{\text{Normalized}} = (dI/dV)_{NS}/(dI/dV)_{NN}$ [64]. This model is a standard one it is called 1D. whose problem is that the current injection is only perpendicular to the plane surface, the Fermi surface of both material N and S side are spherical thus the superconductor supposed has an isotropic order parameter. For this reason, BTK model has been extended to meet a special property of unconventional parameter [65].

Fig. 2.9.1 (a) shows Normalized conductance depending on Z , Transparency $T=(1+Z^2)^{-1}$ at temperature $T=0$. When Z small results double conductivity at $V = 0$ i.e. “AR regime”. Z high behaves tunnel-like “Tunneling regime“. Fig. 3.9.1 (b) shows that depending on the temperature at constant $\Delta=3$ meV, $Z = 0.2$ temperature enhancement leads to smearing effect in conductance spectrum with increasing T .

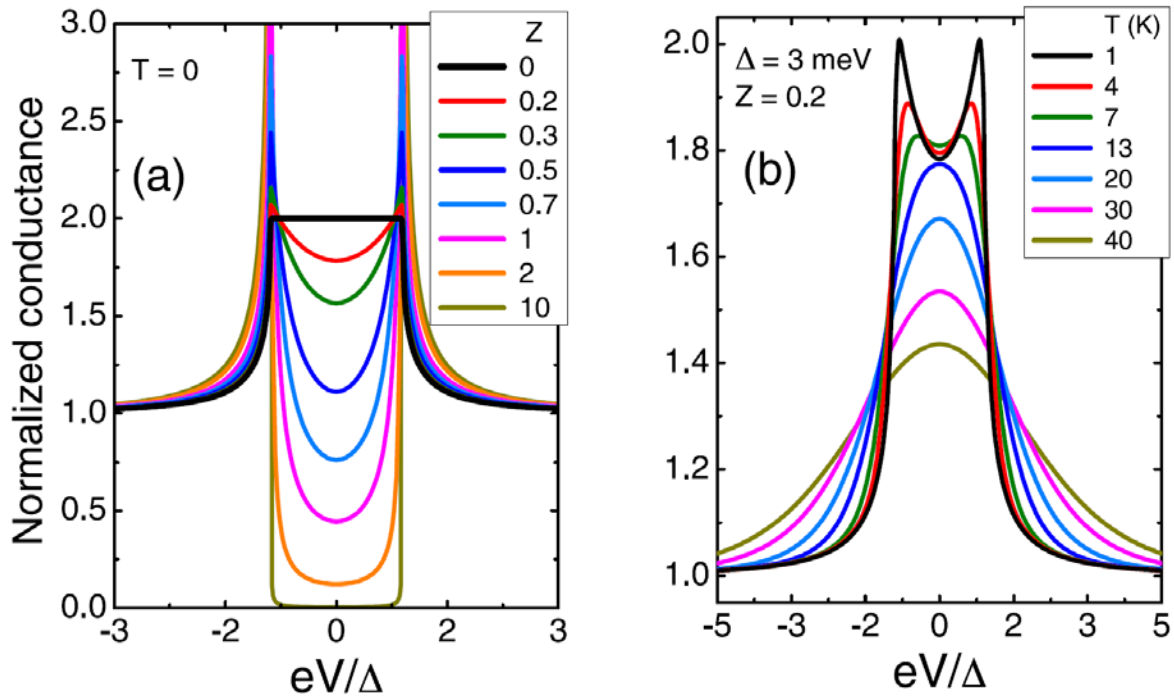


Fig. 2.9.1: Normalized conductance curves of an N/S interface at $T = 0$ calculated within the BTK model with different barrier parameter Z , from pure Andreev ($Z = 0$) to pure tunneling ($Z = 10$) regimes. (b) Effect of the changing temperature on the normalized conductance for $\Delta=3$ meV and $Z = 0.2$ in all the curves. [61]

Fig. 2.9.2 shows the dependence on Dynes-Parameter Γ which is a finite lifetime of Cooper pairs, the Strong influence of Gamma leads to a spread of conductance. The smearing effect in conductance spectrum could become at increased Γ .

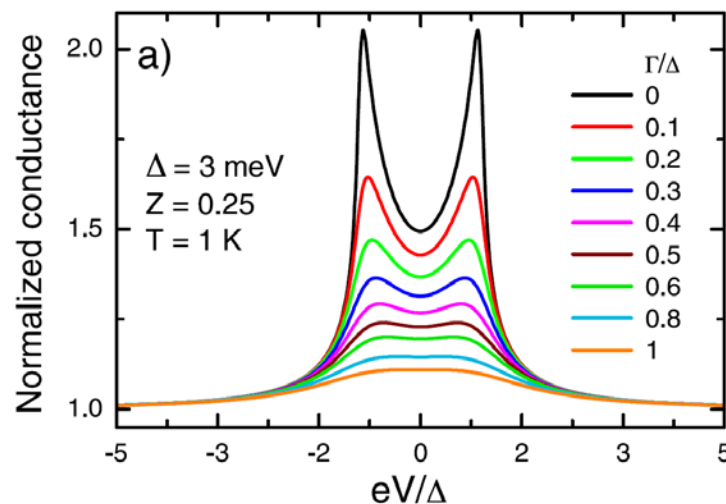


Fig. 2.9.2: Conductance curves calculated at $T = 1$ K by using $\Delta=3.0$ meV, $Z = 0.25$ and increasing values of Γ . [61]

3. MATERIALS PROCESSING AND EXAMINATION

3.1 MATERIALS

To prepare the thin films junctions, we used materials of Ba-122 iron pnictides single crystals. These materials have a rough surface structure that helps prepare a flat surface to fabricate planar Josephson junctions. Therefore this chapter will include the procedure in preparing the crystals, the polishing process, finding the rate of etching polished surface, and examining the crystal surface by EBSD.

3.1.1 CRYSTALS GROWTH

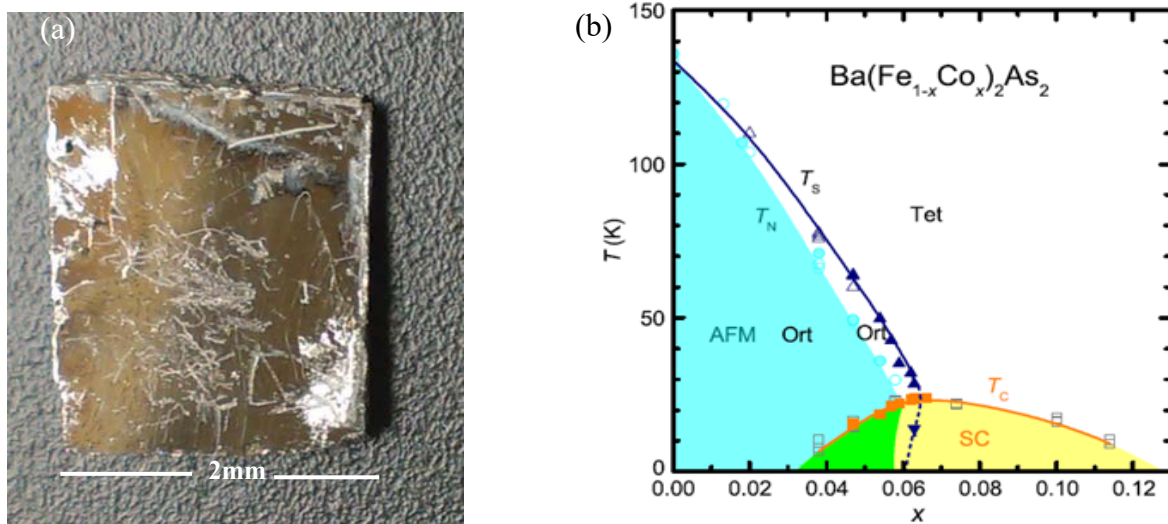


Fig. 3.1.1: (a) A typical Ba-122 single crystal as-grown with rough and scratches (showing irregular surface) surface. (b) Phase diagram of BaFe_2As_2 systems [66].

The $\text{Ba}(\text{Fe}_{1-x}\text{Co}_x)_2\text{As}_2$ single crystals were obtained from T. Wolf's group in Karlsruhe Institute of technology in the optimally doped ($x = 0.06$, $T_c = 23.5$ K) and undoped ($x = 0$) crystals materials. They were produced by a self-flux method [22, 23]. Through this method, the FeAs is used as the common solvent or flux for the growth of the crystal. The amounts of each component were mixed in a ratio of $\text{Ba}:(\text{FeAs}+\text{CoAs}) = 1:4$ or $1:5$. The mixtures were loaded in glassy carbon crucibles. Then they were inserted in an evacuated SiO_2 ampoule in a chamber furnace. The annealing reaction heated the ampoule for 50 °C/h to 700 °C for 20 hours and heated up again up to 1200 °C so that the mixture could be melted under low pressure. The mixture slowly cooled down to 1030 - 1080 °C with the rate of 0.17 - 0.5 °C/h, wherein crystal growth is expected to take place. After reaching the lowest temperature (cooled to room temperature), the ampoules were removed from the furnace, turned round, brought in a steel cylinder, and evacuated. This process enabled in most cases, to obtain crystals mostly free from flux, thus the residual melt is separated from growing

crystals. More details of this technical procedure for different kind of crystals can be found in [67]. A picture of a typical crystal as grown can be seen in Fig. 3.1.1 (a) showing irregular surface.

The phase diagram for $\text{Ba}(\text{Fe}_{1-x}\text{Co}_x)_2\text{As}_2$ is shown in Fig.3.1.1 (b). Temperature $T(\text{K})$ depends on the rate of Cobalt (Co) element (x), where the low Co concentration exhibits antiferromagnetic (AFM) state which appears at normal temperature T_N with orthorhombic (Ort) crystal structure. Co-concentration rate increased slightly for finite x , the compound still has orthorhombic (Ort) crystal structure with low T_c of superconductivity state (SC). T_c reaches the max value for $x \sim 0.063$ which represent the optimally doped, so structural transition temperature (T_s) changed to a tetragonal (Tet) structure with increasing Co concentration.

3.1.2 EDX-ray spectroscopy analysis

Energy dispersive X-ray (EDX) spectroscopy analysis is a technique used to identify the elemental composition of the samples. Thus, the samples of iron pnictides single crystal were analyzed to find the rate of Co. The composition of the different doping for $\text{Ba}(\text{Fe}_{1-x}\text{Co}_x)_2\text{As}_2$ single crystals was tested by EDX analysis. This elemental analysis is shown in Fig. 3.1.2. (a), the rate of Co-doped is calculated to be $x \sim 0.06$, which is optimally doped [66, 68]. The second sample of undoped crystals is shown in Fig. 3.1.2. (b), the analysis shows that there haven't the peaks of the Co-element that means x being equal zero (undoped sample).

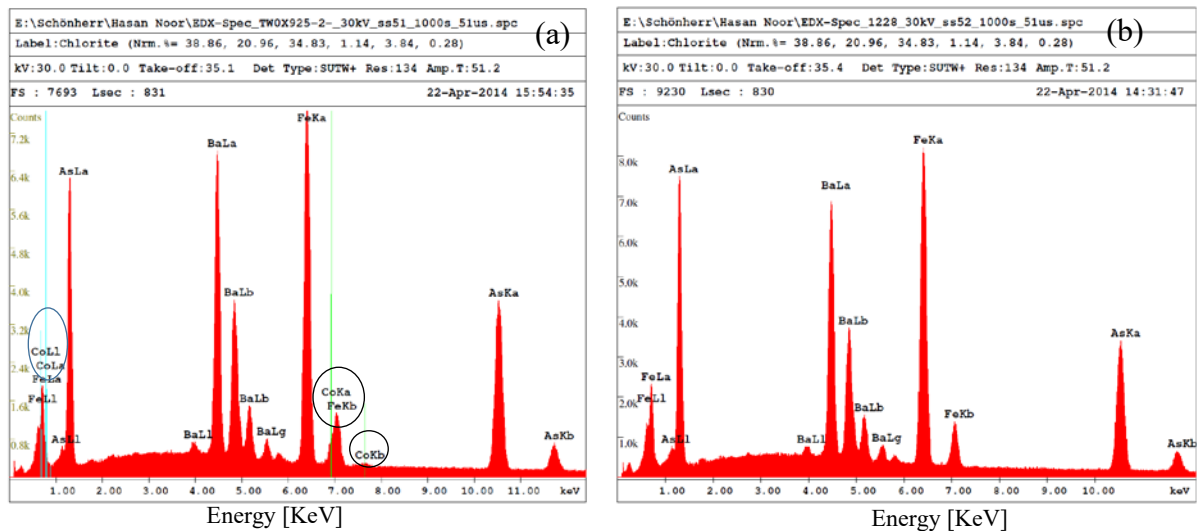


Fig. 3.1.2: The result of EDX spectrum: (a) a sample of Co-doped: Ba-122 single crystal, Co-element illustrated within the black frames. (b) An example of the undoped crystal sample.

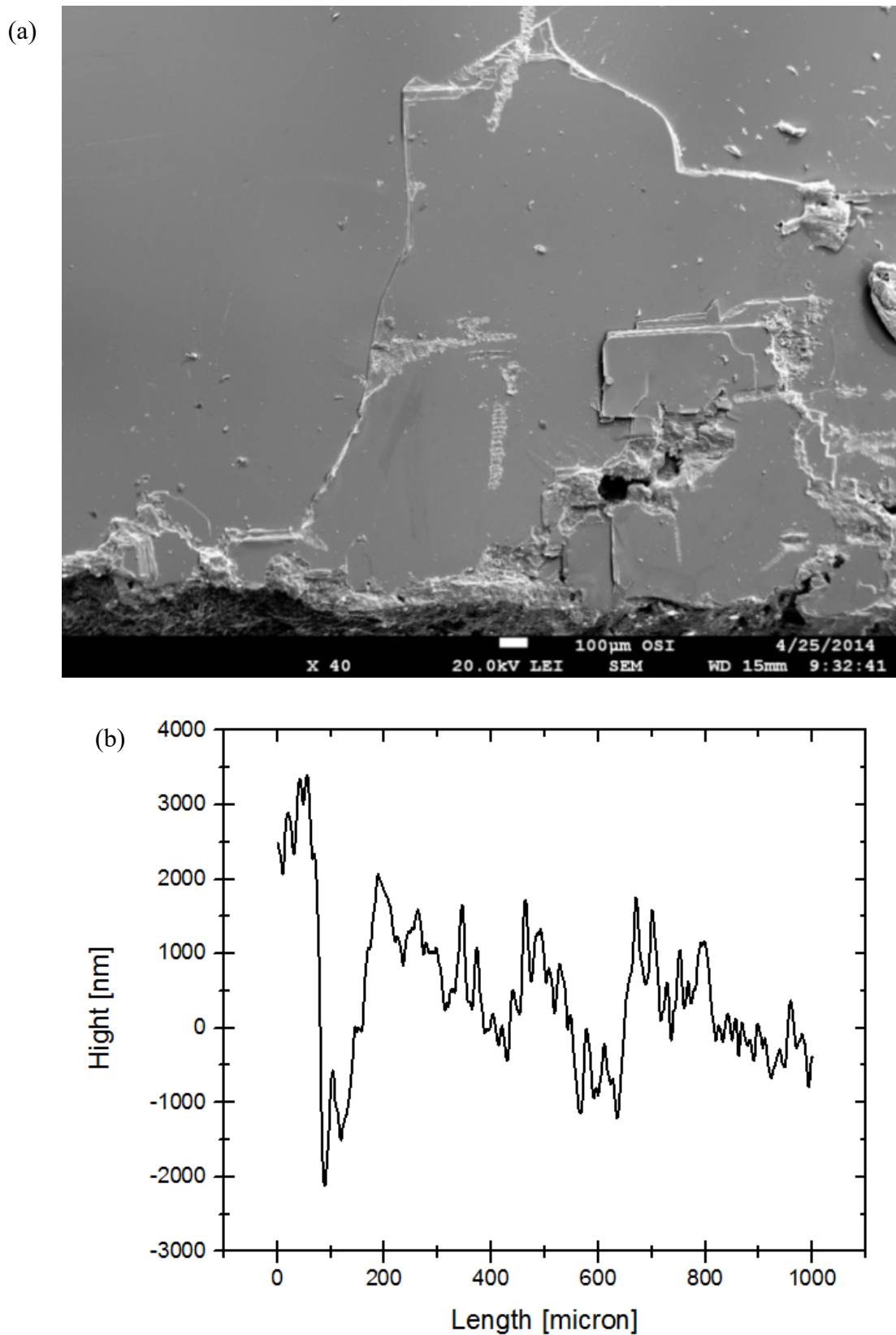


Fig. 3.2.1: (a) SEM-image is taken for the surface of a single crystal as grown, (b) Irregularities measured by Dek-Tak profilometer for an unprocessed surface of a single crystal.

3.2 Crystals processing

A thin film technology requires high-quality surfaces. The surface structure of pnictide materials have rough surface structure, see e.g. the scanning electron microscopy (SEM) image in Fig. 3.2.1 (a) obtained from a crystal as grown. It obviously shows the irregularities that have been estimated by a Dek-Tak profilometer ⁽¹⁾. Measured data of an unprocessed surface is shown in Fig. 3.2.1 (b) give a height of several nm to some microns. These make it necessary to develop and apply a polishing procedure for these materials. Therefore we used chemical-mechanical polishing (CMP) in order to reach a root mean square (RMS) roughness of less than 5 nm.

3.2.1 Cleaving

The received material of the iron pnictide single crystal is like one piece with a relatively large area, larger than $10 \times 10 \text{ mm}^2$. Thus, the cleaving process is required to get several samples from this one piece single crystal. A razor blade (cutting) technique is one possible method for cleaving and cutting it as well. The developed cleavage technique in our laboratory is the second possible method, which is done by attaching the single crystal piece between two different massive plates by using wax. Then the upper massive part should be hitting, in order to cleave it. This process should be repeated several times to have more samples. But unfortunately, these two methods did not provide us the full control within the term of thickness and surface area for the required single crystals to fabricate Josephson junctions in this work.

3.2.2 Sticking

Because of the cleaved single crystals have a small area less than the required area for preparation samples which is about $(4 \times 4 \text{ mm}^2)$, they are mounted on a Si wafer within an area of 10×10 or $5 \times 5 \text{ mm}^2$ in order to improve handling. Therefore, an adhesive is used which is an epoxy material. Other materials existing in our laboratories such as wax and silver paste, their adhesive is not enough to complete and achieve the procedure of thin film technology. During the lift-off process, we faced a problem, the adhesive materials that we used were reduced while using a required removal materials so that the samples and Si-wafer were separated from each other as well as with subsequent steps especially in photolithography which it needs to deal with high-temperature conduction to avoid problem we used an epoxy called “UHU endfest 300” ⁽²⁾ which bearded high temperatures, and can be removed mechanically.

⁽¹⁾Dek-Tak profilometer is a device used to measure a profile of surface roughness.

⁽²⁾UHU plus endfest 300 is an adhesive consists of two components epoxy, which it can be deal with temperature up to 100°C . For more information visit the website of company <http://www.uhu-profishop.de/>

3.2.3 Polishing

Before starting polishing, we have to do the two mentioned steps above in sections 3.2.1 and 3.2.2. Thereafter, there are two possibilities in order to polish the single crystals which are either only Manually Polishing (MP) or Chemical Mechanical Polishing (CMP):

a- Manually Polishing (MP). The first try was accomplished by using Manually Polishing (MP). Thereby different grit sandpaper sheets from rough grit SiC-sandpaper (grit size = 30 and 9 μm) till smooth paper of Micro-Mesh Company (6000 grit size = 4 μm and 12000 grit size = 2 μm), see Fig. 3.2.2. Despite it being a useful method, they may still leave scratches on the surface of single crystals and sometimes be making the surface not plane enough.



Fig. 3.2.2: Two different types of Abrasive sandpaper of Micro-Mesh Company used for polishing.

b- Chemical Mechanical Polishing (CMP). This process is also used for polishing the samples of pnictide single crystals by a Logitech device. This method has an abrasive powder material which decomposes usually by water that causes damage in the surface structure of single crystals. Thus, instead of using water, it is possible to resolve the needed abrasive material by isopropanol in all parts of the process. The Logitech device contains a Lapping disk for planarization, a polishing disk with a certain polishing cloth and a polishing head. That it is shown in the images in Fig. 3.2.3, while in (b) the polishing head overturned to fix the sample holder can be seen.

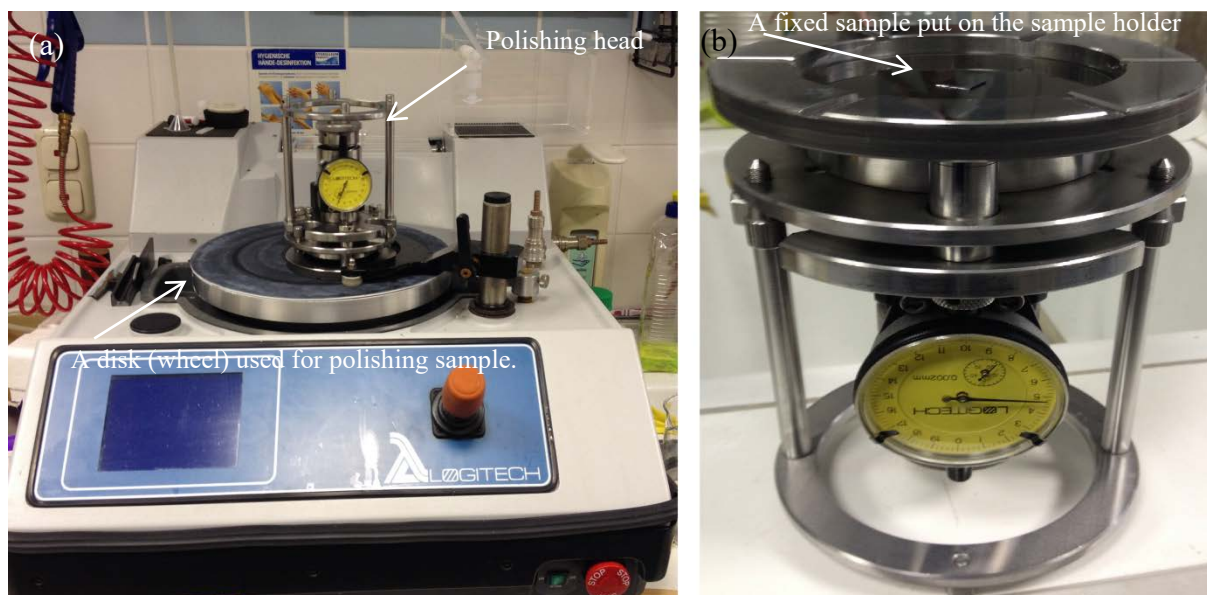


Fig.3.2.3: (a) Logitech device: polishing materials, polishing disk, and polishing head. (b) The polishing head used for fixing a sample. (c) The Polishing head turned up, in order to fix a sample.

The procedure method for polishing finally is as follow:

- 1- Planarization of the crystal with abrasive material “Al₂O₃” powder with particle size 3 μm , resolving an amount of abrasive powder of about 12 g with 200 ml of isopropanol. The speed of the disk can be set to 35 rpm (rounds per minute). After fixing a sample on the holder of the polishing head, we adjusted the applied weight (here within the range of 50g-100g). The maximum weight which can be applied is 2 kg. To carry the flow of abrasive material (Al₂O₃ solution), we used dropping glass funnel that allows the flow to be controlled.
- 2- The second step after planarization is to use abrasive sandpaper Micro-Mesh MM (6000 grit size 4 μm and 12000 grit size 2 μm) see Fig. 3.2.2. This step is required; one has to use them in order to get a roughly smooth surface. The disadvantage of this method is uncontrollable within the term of the crystal surface. Instead of that, an abrasive material should be available with a particle size larger than 0.05 μm .
- 3- High precision finishing can be reached by using abrasive powder material “Al₂O₃” with particle size 0.05 μm , resolving a weight of powder 20 g in 400 ml of isopropanol. Instead of lapping disk which used in the first step, the disk of polishing cloths was set to the speed of the disk to reach 70 rpm. The applied weight should not exceed 2 kg. The surface after polishing can be seen in the Fig. 3.2.4 (a), where the flattened areas of the surface are indicated by white frames. RMS roughness of 1.96 nm was measured by AFM and shown in Fig. 3.2.4 (b), Usually the RMS is less than this mentioned value.

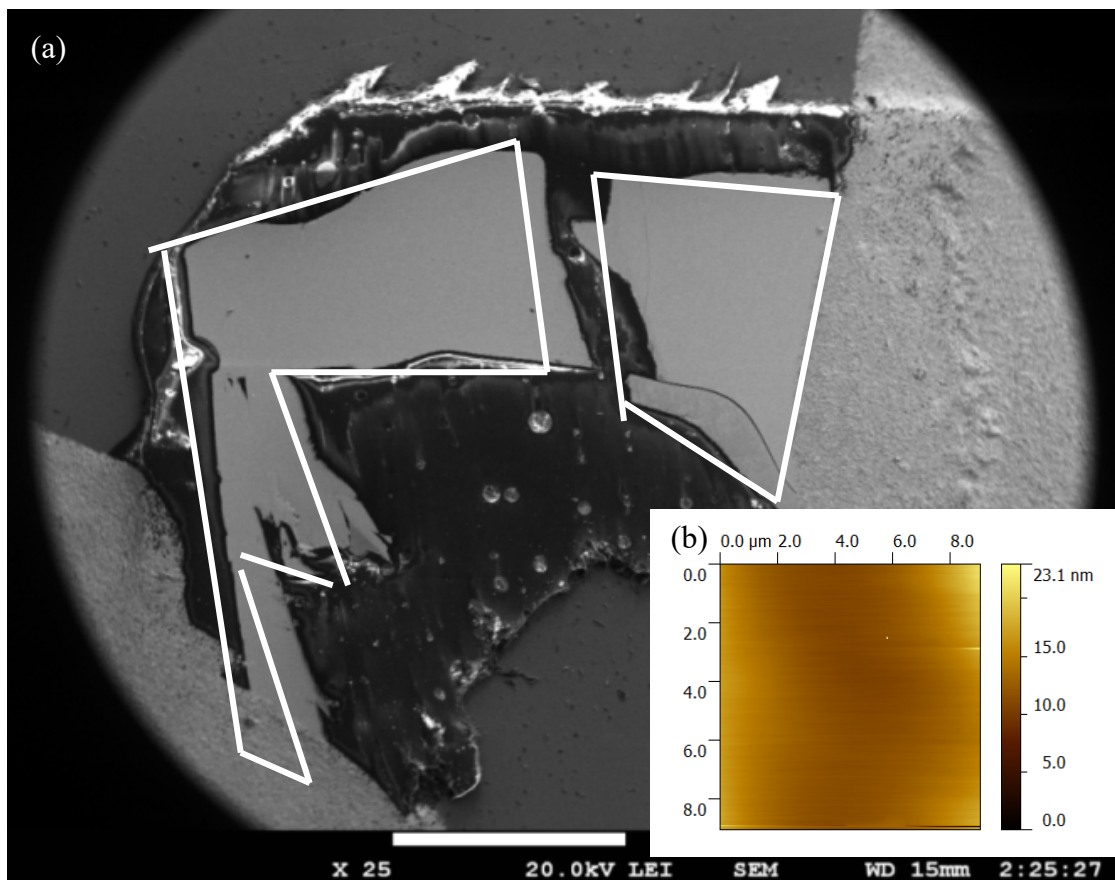


Fig. 3.2.4: (a) SEM-image is taken for a sample of polished surface with flattened areas within the white frames, inset figure (b): AFM measurement of a polished surface RMS=1.96 nm.

3.3 Etching rate of single crystal

Surface etching is necessary for cleaning and reducing the roughness of the surface and thinning films in fabricating a junction device. The etching is needed for all fabrication processes. Thus the rate of deep etching is important to be known. This required subsequent steps as follow:

- 1- Polishing the samples at minimum RMS.
- 2- The mask for patterning was realized by photolithographic preparation process with a positive photoresist. The width of each line of a mask is $3.50\ \mu\text{m}$ and the space between two lines is $8.48\ \mu\text{m}$. Fig. 3.3.1 illustrates the photo mask.
- 3- Etching with different time of 30, 60, 120, and 150 was performed.
- 4- IBE equipment uses argon gas, an angle between beam and target surface of 0° and no sample cooling by liquid N_2 .

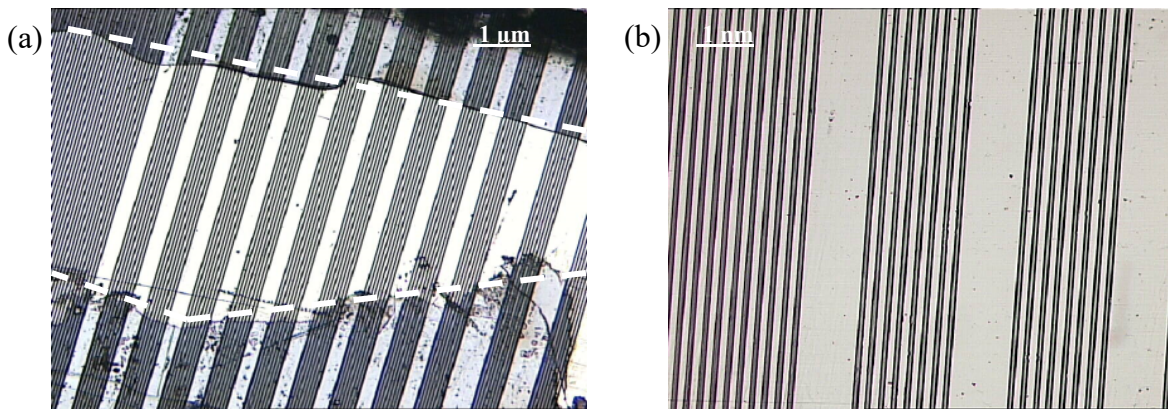


Fig. 3.3.1: Microscope image of a polished single crystal, (a) The black lines represent a mask of positive photoresist process, the surface of single crystal illustrated in a white dashed frame. (b) A part of surface illustrated in Fig. 3.3.1 (a), which is an image with high magnification.

- 5- The used parameters were : beam voltage: 500V, acceleration voltage: 100 V, current density: $0.9\ \text{mA}/\text{cm}^2$
- 6- Measurements were done by atomic force microscope (AFM) for image analyzing used the Gwyddion program⁽³⁾ and Dek-Tak profilometer.
- 7- The rate of error belongs to the roughness of the surface. The rate of etching for Ba-122 single crystal with 0° is about $25\ \text{nm}/\text{min}$. In Fig. 3.3.2 (b) illustrates the rate of etching and graph for different times.

⁽³⁾ Gwyddion is a program used to analysis the images which obtained by AFM, see <http://gwyddion.net>.

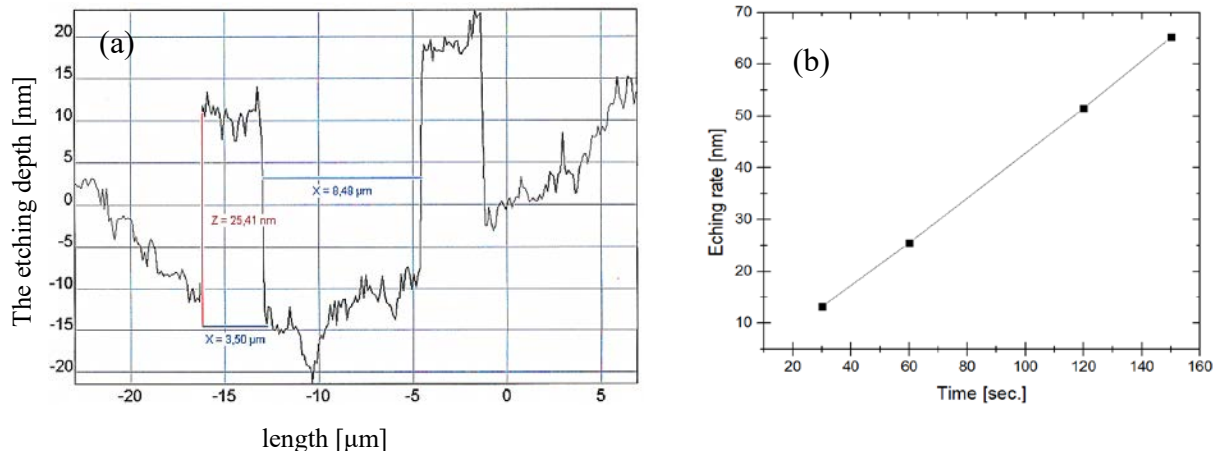


Fig.3.3.2: (a) The etching depth vs. length of a sample measured by Dek-tak profilometer measurement for the polished surface it's time of etching was 1 min. The peaks represent that the regions of surface are not etched down due to the surface was coated with a mask of a positive photoresist. (b) The different etching times corresponding to the etching depth.

3.4 Examination the crystal surface by EBSD-measurements

In order to investigate the surface structure of processed samples including the influence of polishing and etching, the surface was examined by electron backscatter diffraction (EBSD). The examinations for some samples were performed at the Otto-Schott-Institute for Glass Chemistry.

EBSD analysis [69, 70] is used to evaluate quantitative microstructure analysis in the SEM. The SEM micrograph and its EBSD analysis for five different locations of a doped crystal are illustrated in Fig. 3.4.1. It shows that the crystal orientations which can be indicated by three Euler Angles (21° , 178° , 12°) with a deviation of less than 2° , illustrated in the white frame on the left. The crystallographic axes of doped crystals refer to a tetragonal crystal system, like in undoped ones. A SEM image with EBSD analysis of unprocessed undoped crystal is reported in Ref. [71].

The respective Kikuchi bands for both doped and undoped samples are shown in Fig. 3.4.1. The Kikuchi bands, which are shown for a polished sample in Fig. 3.4.1 (a); show a high-quality pattern in the investigated region. The crystal lattice in the investigated region should ideally be strain-free and relatively clean from contamination or thick oxide layers so that the diffraction pattern will occur. If these conditions are not met, the resulting EBSD patterns will have a poor quality or they will be diffuse as can be seen in Fig. 3.4.1 (b) (2, 4, and 5) in the case of doped crystals. They show a locally lower image quality of Kikuchi-patterns, which may be caused by degradation in the atmosphere or an inhomogeneous polishing process.

In contrast, Fig. 3.4.1 (b) (1, 3) display that the crystal structure is not significantly distorted everywhere. That may be the case because its surface is comparatively free from any of the disturbances mentioned above. To remove such degradation that may occur on the surface after a polishing procedure on the surface, an additional process of ion beam etching can be introduced.

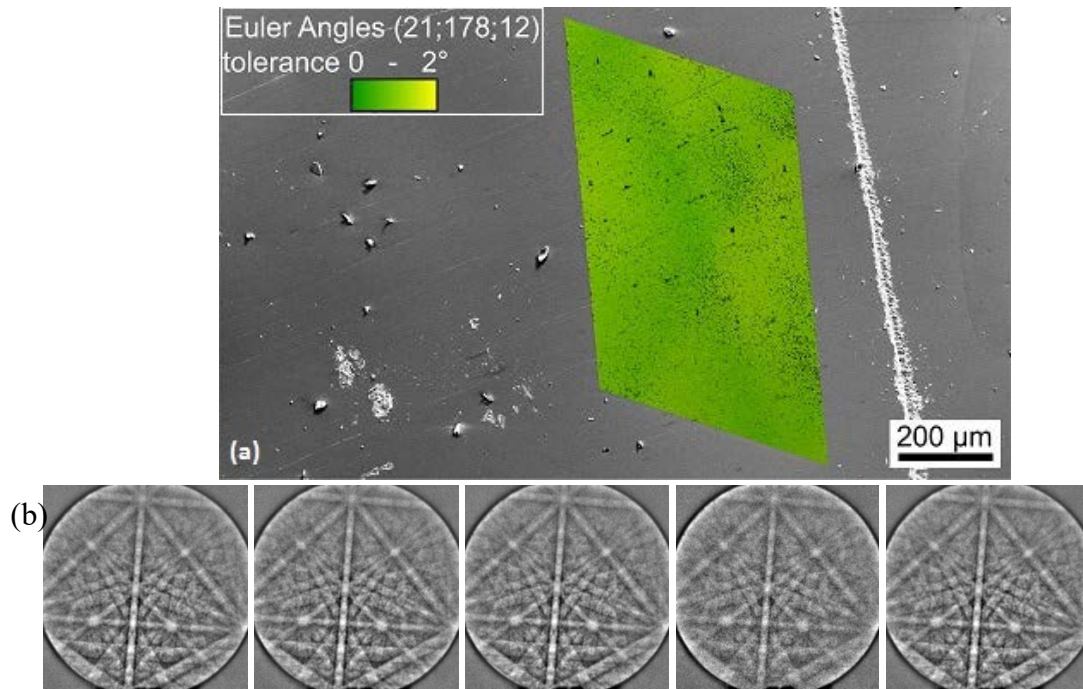


Fig. 3.4.1: (a) SEM image of the unprocessed surface of a doped crystal. (b): Kikuchi patterns obtained from its surface at five different locations.

Fig. 3.4.1 (c) shows that a subsequent etching step may enhance the surface quality and thus may enhance the EBSD-patterns quality compared to the ones in Fig. 3.4.2 (a). In addition to the cleaning, ion beam etching is one of the main tools for sample preparation in thin film technology. The samples are treated by using an Ar ion beam (beam voltage = 500 V, acceleration voltage = 100 V, current density = 0.9 mA/cm²) for both the cleaning and the etching process.

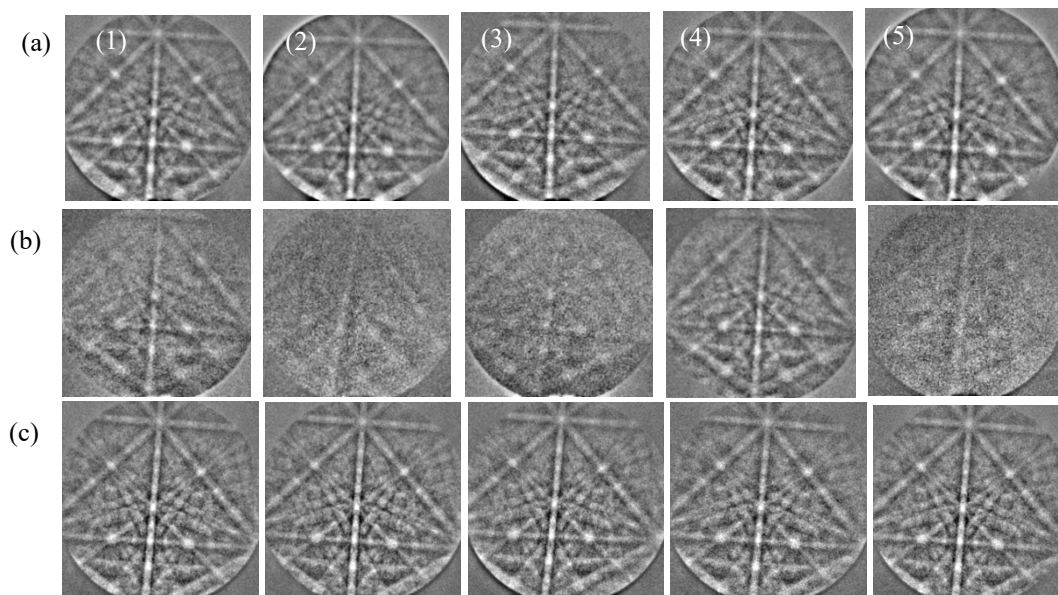


Fig. 3.4.2: Kikuchi -patterns obtained at five different positions (1 to 5) on differently treated (a, b, c) crystal surfaces. (a) and (c) row undoped (twox1228) are polished surface and etched surface respectively, (b) is polished doped crystal (twox925)

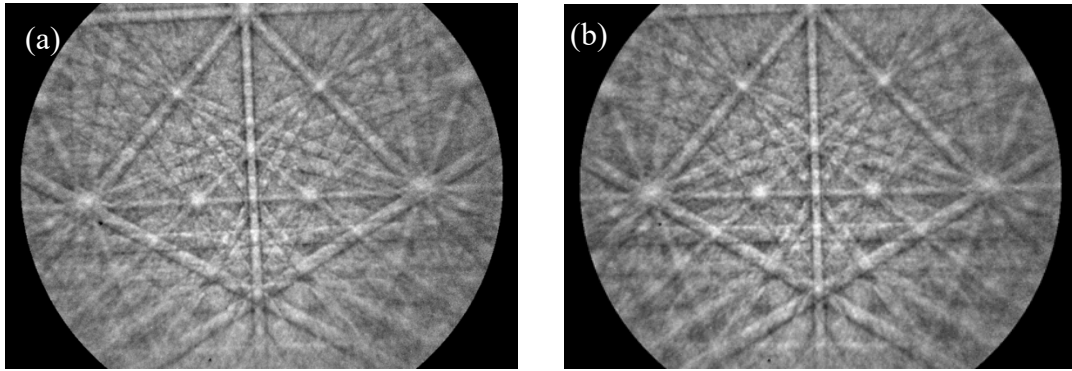


Fig. 3.4.3: (a) & (b) Kikuchi -patterns obtained from two samples of Co-doped crystal surfaces treated under the same conditions show clear diffraction pattern reflected from the surface of the crystal.

Fig. 3.4.3 shows the polished surface of the two doped crystal samples which were etched for 2 min after the EBSD took place. The surface quality is enhanced thus the EBSD-patterns quality becomes better in comparison to the ones in Fig. 3.4.2 (b, a). Through EBSD-patterns results for process surface can ensure that the processing method may have a small influence on surface structure. The surface quality of the doped samples most probably will be improved after a subsequent etching step. We will be able to use doped single crystals for junction fabrication.

4. THIN FILM TECHNOLOGY AND SAMPLE PREPARATION

4.1 THIN FILM TECHNOLOGY

The optimally doped [66, 68] $\text{Ba}(\text{Fe}_{1-x}\text{Co}_x)_2\text{As}_2$ single crystals ($x \sim 0.06$, $T_c = 23.5$ K) used for preparing the planar junctions along the crystallographic c-axis, which is based on the photolithographic preparation process that used in thin films [72, 73] extended to meet the special properties of single crystals, as follows:

4.1.1 PHOTOLITHOGRAPHY AND JUNCTION LAYOUT

Photolithography is an optical technique of uniform UV exposure for transferring patterns onto a substrate wafer. The used mask is a chrome coated glass plate shown in Fig. 4.1.1. The three indicated regions with rectangles frame by green lines are required for fabrication planar hybrid Josephson junctions. Fig. 4.1.1 (a) sector (B3 left) and (b) is the base electrode mask of an area of $5 \times 10 \text{ mm}^2$ which has 10 possible junctions (contacts) with different areas start from $3 \mu\text{m}^2$, $5 \mu\text{m}^2$, $7 \mu\text{m}^2$, $10 \mu\text{m}^2$, $15 \mu\text{m}^2$, $20 \mu\text{m}^2$, $30 \mu\text{m}^2$, $40 \mu\text{m}^2$, $50 \mu\text{m}^2$ and end with large area $100 \mu\text{m}^2$. In the same Fig. 4.1.1 (a) sector (B3 right) and (d) used to make a counter electrode. Fig. 4.1.1 (a) sector (A1 right) and (c) used to make pads for counter electrode. The final fabrication is illustrated in (e) shows a complete schematic design. See Fig. 4.2.4 (b) P. 45 shows a schematic design of planar Junction.

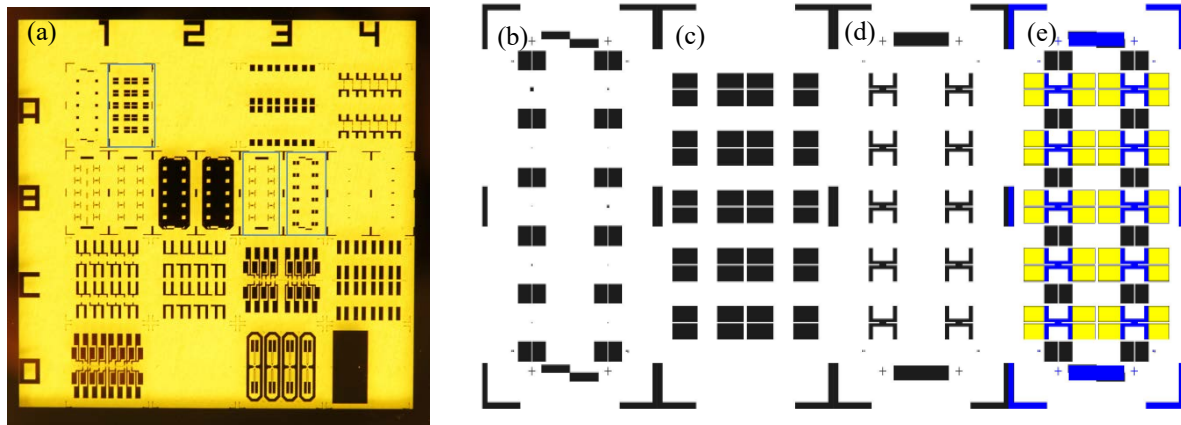


Fig. 4.1.1: (a) Photograph of the photolithography mask. Schematic of the photolithography mask: (b) Base electrode mask with 10 different junctions area, (c) Pads for counter electrode mask, (d) Counter electrode mask and (e) The combination of all masks previously mentioned [74].

There are three different processes required to transfer the mask to a surface sample. That can be achieved in a lab “clean room” by using centrifugal, hot plate, and certain photoresist material which is light sensitive for UV exposure. Normally two photoresist materials are used in this work, which are TI35ES and AZ5214E photoresist for a positive and negative process, respectively. The methods are discussed as following:

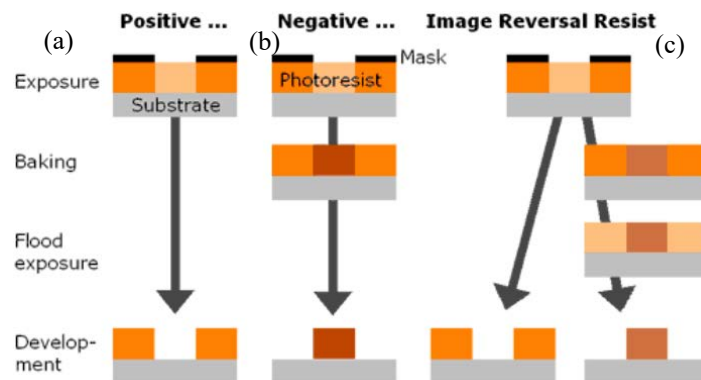


Fig. 4.1.2: Schematic diagram of the three procedures for the photolithography: (a) Positive process. (b) Negative process. (c) Reversal process. [75]

Before any method might be done, the surface of the sample has been cleaned by using isopropanol, and then the sample was placed on hot plate for 2 minutes at temperature 130°C . In order to stick a photoresist material on the surface of the sample, then it should be put in a centrifugal device.

- i) Positive process means when a substrate covered by a positive photoresist which can develop by exposure, a developer solution only removes the photoresist in the exposed areas while unexposed areas patterned on the substrate. Certain developers are used to obtaining a pattern on the sample. There is a need to stop a developer which is done by distilled water. The positive process is illustrated in Fig. 4.1.2 (a). In this work prefer to use the TI35ES photoresist which is necessary for etch down the surface of the crystal and is suitable to stop its developer by isopropanol to prevent any damage may happen to the surface of single crystals while the base electrode is made. However, in this case, the surface of single crystals can be coated by an Au protecting layer with a thickness of more than 50 nm.
- ii) Negative process means when a substrate covered by a negative photoresist. The photoresist is exposed as the first step and then complete the substrate surface exposed to UV light, the process is illustrated in Fig. 4.1.2 (b). The unexposed area of the photoresist is dissolved in the developer. Distilled water must be used here to stop the developer because isopropanol in this photoresist will act as a removal material and disturb the pattern. In this current work used AZ5214E photoresist for all negative fabrication process except base electrode. Here it is possible to use an alternative method as a reversal process like in positive process.
- iii) As an alternative to positive or negative process, In order to obtain negative process from a positive photoresist, we have to resort to image reversal. The process is illustrated in Fig. 4.1.2 (c). The advantage of using the third process is in case only one photoresist available. Then there is a possibility to do either positive or negative process.

4.1.2 EQUIPMENT FOR THIN FILM TECHNOLOGY

The equipment to prepare thin film technology in our laboratories uses the vacuum systems for IBE, Ti/Au, SiO_x and Pb/In. The principle of work the vacuum systems are almost similar. The system contains vacuum chambers with the turbo molecular pump in addition to a rotary vane vacuum pump. The chamber is first evacuated to a pressure 1 mTorr by the rotary vane vacuum pump then after the turbo is turned on which is required to pump the system down to reach pressure at a value less than 1.6×10^{-6} Torr. This prevents the surface from contamination. In order to use sputtering and etching chamber, typically argon gas is introduced into the vacuum chamber, in order to make sputtering procedure. The pressure value is set inside at the range (10-15) mTorr equivalent to value (1.3×10^{-2} - 1.9×10^{-2}) mbar. Additionally, it included oxygen gas in case SiO_x-layer sputtering.

4.1.2.1 SPUTTERING SYSTEMS

Sputtering is a physical vapor deposition (PVD) method. The idea of sputtering is the deposition of a thin film from atoms mechanically kicked out of the target material on any surface (a substrate) in specified pressure in a vacuum chamber.

The sputter deposition uses a technique called magnetron sputtering, which is a plasma coating process. Magnetron consists of a magnet placed behind a target material which works as the cathode, while the substrate acts as the anode. The argon gas is introduced between the target and the substrate leading to the ionization of the gas. In the other hand, the pressure increases in the vacuum chamber into the desired value to operate a magnetron. When a certain power was applied to the magnetron, a voltage of 300 V or higher is applied to the target. The ionized incoming of particles is attracted and accelerated toward the negatively charged target. They bombardment target atoms by energetic particle caused the removal of atoms from the target. The sputtered atoms condense and form a thin film. A sputtering deposition system was used to deposit Ti, Au, and SiO_x thin films. It is achieved by applying a method of direct current (DC) or radio frequency (RF). Fig. 4.3.1 shows a schematic of the physical sputtering technique process.

TYPES OF MAGNETRON SPUTTERING

4.1.2.1. A) DC-MAGNETRON SPUTTERING:

DC-Magnetron sputtering used in this work for depositing metal atoms (e.g. Ti, Au, Nb). The sputtering of thin films was carried out at four constant cathode powers (30, 50, 70 W for Ti target and 50 W for Au target). The required pressure is used for sputtering with a rate of about 15 mTorr by supplying argon gas. More details on the used system can be found in Ref. [76, 77]. Ti/Au film is used as pads for the counter electrode.

4.1.2.1.B)

RF-MAGNETRON SPUTTERING:

Used in this work for depositing insulator material (e.g. SiO_x). Argon gas 20 sccm, oxygen flow of 10 sccm are used in a sputtering process. This gas will react with the target surface as well as the sputter deposited metal atoms. Thus it forms a dioxide thin film on the substrate. SiO_x film is found to be an insulating layer between base electrodes (single crystals) and counter electrodes.

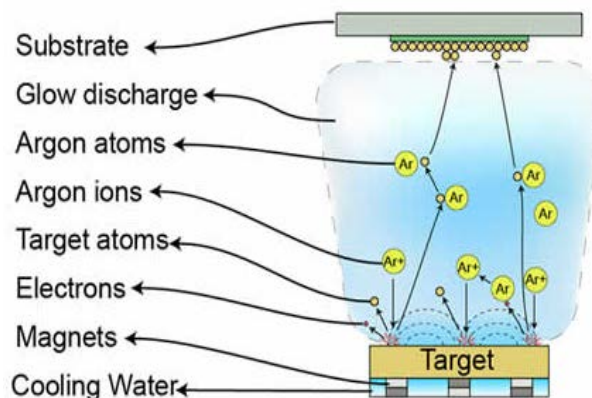


Fig. 4.3.1: Schematic layout of the physical sputtering process: The basic components of a magnetron sputtering system. Ionized Argon bombards a target, releasing atoms which form layers on a substrate. Electrons and Argon ions form plasma, which is located near the target due to the magnetic field, resulting in greater efficiency and quality. [78]

4.1.3 ION BEAM ETCHING (IBE):

IBE is a useful dry etch technique for cleaning surfaces, reducing the roughness of the surface and thinning films in fabricating a junction device. In addition to those, IBE is one of the main tools for sample preparation in thin film technology. In Ref. [79] the authors show that ion etching has advantages regarding surface properties of several materials. A subsequent etching step may enhance the surface quality. The surface to be etched is placed in a vacuum chamber that must be evacuated to 1.6×10^{-6} Torr or less. During the etching process, the working rate of Argon gas is 2 sccm (10^{-4} Torr). The ionized gas is generated inside the ion source which is called Kaufman ion source named after Kaufman. Kaufman ion source is a plasma generation device. The ionized gas is accelerated into ionized beams from the source toward to a substrate. The substrate can be tilted to an angle between argon ion beam and substrate (0° , 10° , and 20°). 0° is used in this current work. The IBE step is realized for a sample which is patterned by the use of a photolithography process. Our samples are treated by using an Ar ion beam (beam voltage = 500 V, acceleration voltage = 100 V, current density = 0.9 mA/cm^2) for both the cleaning and the etching process. On a CMP-polished surface of the single crystal, the etching rate was determined to be up 25 nm/min by using the parameters mentioned above.

4.1.4 THERMAL EVAPORATION

Thermal evaporation is a physical vapor deposition (PVD) method like the sputtering deposition. But the deposition technique here is different little bit thereby a thermal evaporator uses an electric resistance heater to melt the material then raise its vapor to a useful range and condense on the substrate. This is done in a high evacuated vacuum without any including of argon gas or other. The evaporation process used for the deposition of lead and indium superconductors as counter electrodes.

4.2 JUNCTION FABRICATION

The preparation of planar hybrid Josephson junctions including single crystals as base electrode and lead counter electrode is described in the following steps:

1. Sticking a single crystal on a silicon wafer ($10 \times 10 \text{ mm}^2$) for improving handling. Samples have to be polished for getting smooth surface structure, details in section 3.2. To make a single junction, we need a minimum surface area of single crystals about $4 \times 4 \text{ mm}^2$, see Fig. 4.2.1 (a), which contains a large piece of the single crystal. Fig. 4.2.1 (b, c) shows two junctions which were fabricated on it.

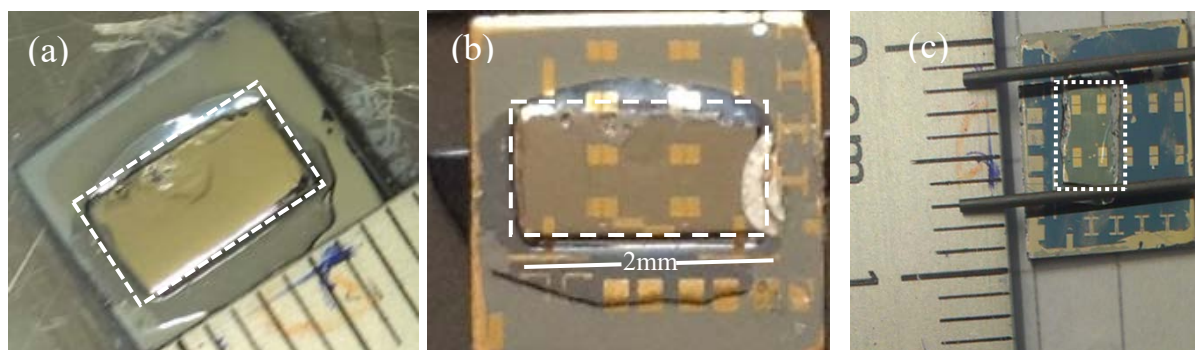


Fig. 4.2.1: Photograph images of a sample of single crystal: (a) An example of a polished sample surface mounted on Si-wafer and placed beside a ruler. (b) & (c) The based electrodes fabricated on surface crystals showed in a yellow color which is a gold protected layer. The pieces of single crystals are illustrated in the dashed rectangle border.

2. Even though, the crystal surface is sensitive to water and acetone, we have to use them in the photolithography process for junction preparation. Thus additionally there is a film by sputtering of a 50 nm thick Au layer which protects the sample surface. In that way, we are able to fabricate the junctions. In order to make a base electrode, it needed photoresist mask with thickness $2.5 \mu\text{m}$ (positive process). Finally, we used an ion beam etching step for patterning the base electrode, see Fig. 4.2.1 (b).

4. Sputtering of a SiO_x layer was used to ensure insulation between the base electrodes (pnictide crystal) and the counter electrode with thickness 200 nm. To prevent short-circuit may be happened later we sputter SiO_x layer many times. We repeated the steps in point two; the SiO_x -layer is sputtered again with thickness 200 nm. Fig. 4.2.2 (a) shows the base electrodes (gold) with two junctions at a different area. A magnification of a single junction is shown in fig. 4.2.2 (b), this is a microscope image shows the base electrode with its junction, where the violet color belongs to the SiO_x layer.

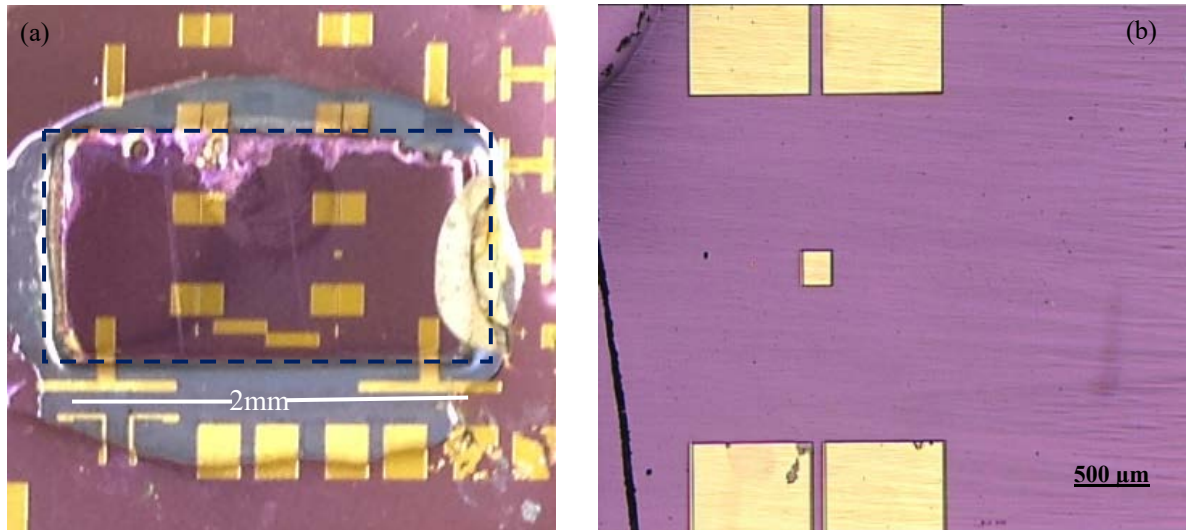


Fig. 4.2.2: (a) Photograph image for a sample which contains base electrodes with two junctions. The single crystal is illustrated in the dashed rectangle border. (b) Microscope image of a single junction is illustrated the base electrode surrounded by SiO_x layer (violet).

5. After sputtering step which mentioned before in point 4, we need a lift-off process which is possible by using acetone or stripping with assisting of ultrasonic. The lift-off process caused sometimes completely removing for SiO_x layer. See for example a sample in Fig. 4.2.3, where the rest of SiO_x insulator layer is identified by elliptical red shapes. To ensure effective layer operation and to avoid short-circuit; the sputtering of SiO_x should be greater than 400 nm and for several times.

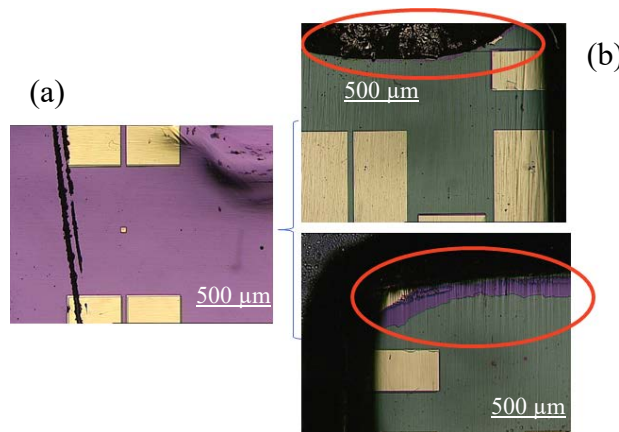


Fig. 4.2.3: Microscope image: (a) An example of a sample still contains SiO_x -layer completed on the all surface. (b) The elliptical frame indicated the violet color is insulator layer which has been removed during lift-off process.

6. To prepare the pads for counter electrode by patterning we need photoresist coating with a thickness of $1.4 \mu\text{m}$ (the negative process used). Before deposition of a Ti and Au layer, we need to sputter a SiO_x layer of 100 nm which will be placed under the Ti/Au layer, see Fig. 4.2.5 (a).

7. The lift-off processing took place by using either Acetone or making warm technistrip, while the ultrasonic is not necessary here.

8. Now, the masking process for the counter electrode pads occurred and the Ti/Au have been deposited in situ which is necessary for binding the electrical wires, Ti, Au film thickness were 26 nm, 120 nm respectively. The titanium used because it is adhesive on the sputtered SiO_x . For electrical contact, such a gold wire bonding was used gold sputtered layer.

There is a possibility to make another film instead of Ti/Au by using another material like (Al/Au, Al/Cu or Al/Cu/Au). The film of Al or Cu is evaporated but Au is sputtered. Al film has the same properties like Ti which is adhesive on the insulator SiO_x layer. See fig. 4.2.4.

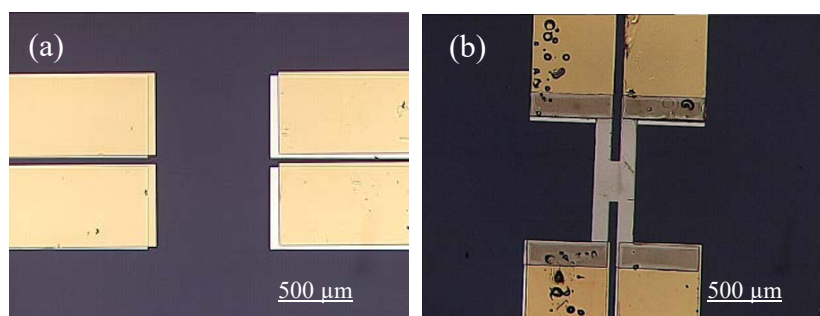


Fig. 4.2.4: Microscopic image of Al/Au pads on a Si-wafer. (a) An example of Al/Au layers used as pads for counter electrodes (above sputtered gold layer (yellow) with thickness 130 nm and down evaporated Al layer (white) is patterned as rectangles shapes). (b) PbIn evaporated as counter electrode on Al/Au pads.

9. A layer of Au cover has been removed by etching the surface. In order to remove it completely to make the mask of the base electrode but in the case, it should be used the negative process as shown in Fig. 4.2.5 (b).

10. Barrier preparation is an important step which is done in-situ by sputtering a Ti layer and metal such as Au-barrier. A Ti barrier can use as an insulator barrier, thus it needed a subsequent oxidation in the atmosphere with heating the sample on the hot plate at 80 °C for 30 min.

11. Lift-off processing takes place again but without using Acetone.

12. For patterning counter electrodes we need a photoresist mask with a thickness 1.4 μm (the negative process used again). Deposition of a double layer of Pb/In as counter electrode is done by thermal evaporation, Pb layer has a thickness of about 300 nm and In layer has a thickness 50 nm. We used an In layer as protecting layer because Pb oxidized with atmosphere if it is left for a long time. It is also possible in this step to remove the Au cover layer.

13. Lift-off processing took place by using either acetone or making warm technistrip, while the ultrasonic is not necessary here.

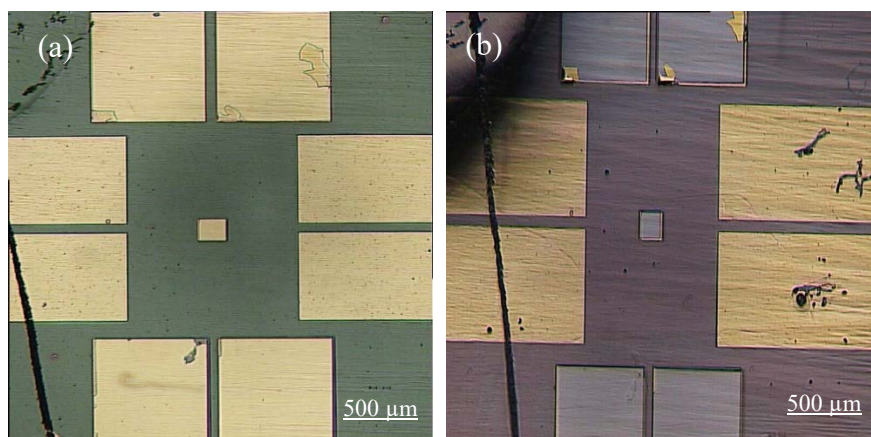


Fig. 4.2.5: (a) and (b) Microscope images of a planar hybrid junction on a single crystal. (a) The base electrode (above and down in the image) is patterned as rectangles shapes by the protection gold layer (yellow), junction area is in the middle, and is formed by a thick SiO_x layer (green). To improve the contacting of the counter electrode (Pb/In) bilayers of Ti/Au (yellow) have been deposited on the insulator. (b) There is an etching process introduced in this sample for removing Au protection layer from base electrode and junction.

14. Fig. 4.2.6 (a, b) shows a final fabricated junction on a processed pnictide single crystals. In order to prepare the sample for electrical meaning, it installed on the electrical board and made electrical wires bonding (Fig. 4.2.7). Fig. 4.2.8 shows where it should be contacted the wires corresponding to bonding pads of the base electrode (Ba-122 single crystals) and counter electrode (lead). The junction design allows examination of transport within c-axis and to measure in 4 point geometry the electrical properties of the single crystal as well as lead thin film, and the junction itself.

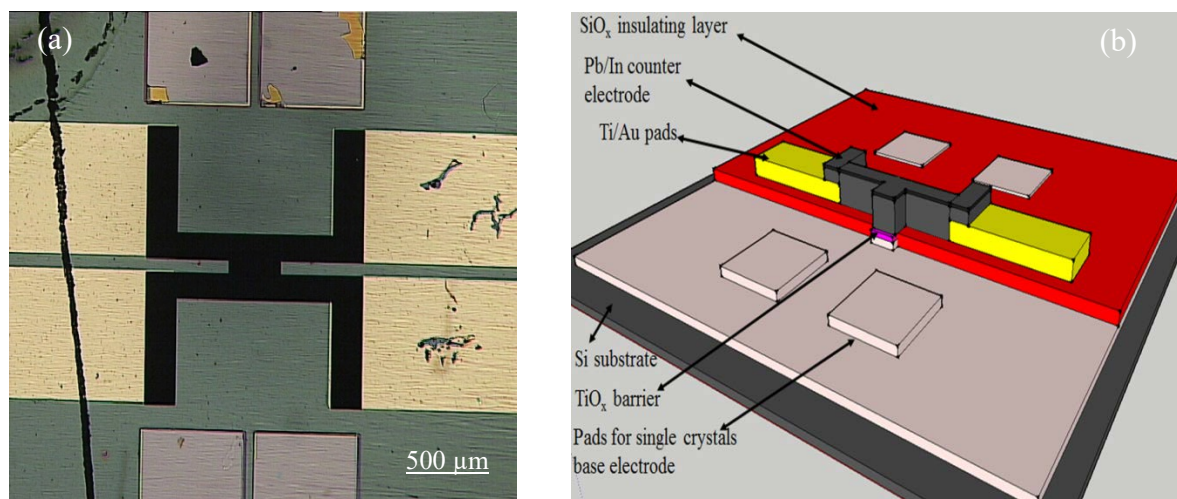


Fig. 4.2.6: (a) Microscope image: a final fabricated junction on a processed crystal. (b) Schematic layout of the junctions.

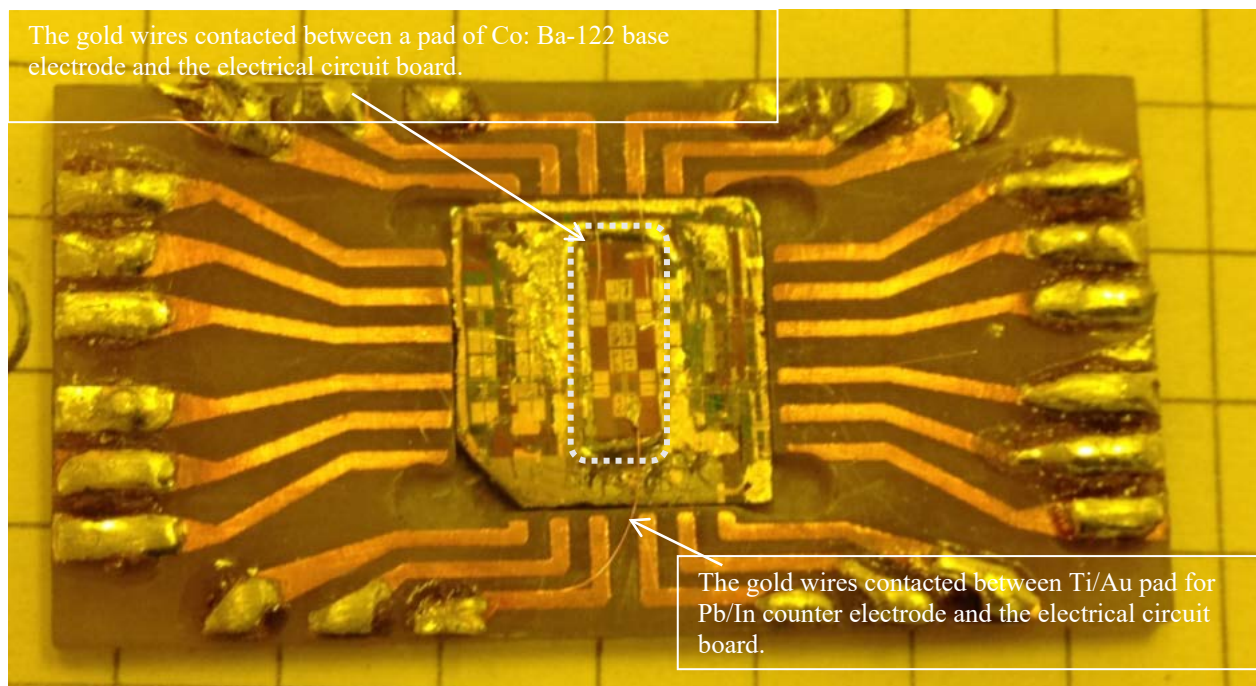


Fig. 4.2.7: A photo image of a sample which is ready for electrical measurements. A sample of Co: Ba-122 single crystals contains of two junctions. That illustrated in the rectangle dotted border.

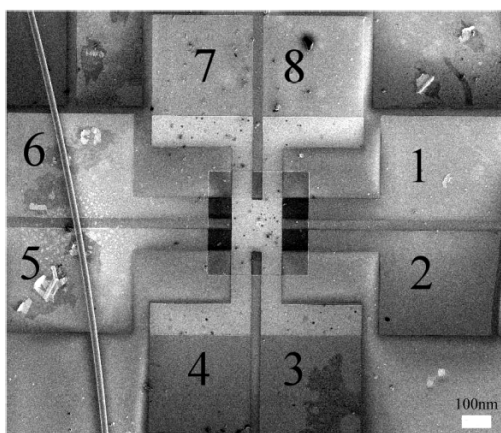


Table .1 Device parts corresponding to bonding pads numbers of left figure.

setup	device part	current	voltage
I	122 electrodes	1-5	2-6
II	Pb electrodes	8-4	7-3
III	junction	1-4	2-3

Fig. 4.2.8: Scanning electron microscope image of a planar cross type junction. The numbers mark the bonding pads. Their assignments to the electrodes are explained in table 1. [80]

4.3 ELECTRICAL MEASURING TECHNIQUES

In order to measure a sample of Josephson junctions or point contact, we adapt a system with an equivalent circuit diagram (see Fig. 4.3.1) of the computer-aided needs to set with using the following devices:

- 1- Source Measure Unit (SMU) : Keithley 236
- 2- Lock-In : EG&G 7260 DSP LOCK-IN Amplifier LabView.
- 3- Gain “Amplifier voltage” : EG&G PARC MODEL 113 PRE-AMP
- 4- A current source for the coil : Keithley 224 Programmable Current Source
- 5- A Voltage meter for temperature diode : Prema 5000 Digital Multimeter
- 6- A microwave generator : Hewlett Packard 83751B Synthesized Sweeper
- 7- To allow and appear the measured $R(T)$, $V(I)$, even $I(V)$ on computer, a special Labview software is installed. Usually it is used to measure $V(I)$ in almost all samples.
- 8- A measuring rod required for measuring $I-V$ characteristic, additional measurements of $I-V$ characteristic under microwave irradiation and magnetic field. The measuring rod consists of many parts as shown in Fig. 4.3.2.
- 9- The measurements are realized by making 4-points on the sample (it is also possible only two points) for current and voltage measurement. The sample mounted on a piece for electrical board with measuring system devices as shown in Fig. 4.2.7 and Fig. 4.2.8. The sample is contacted in 4-point geometry. Then it put on a measuring rod.
- 10- A photo for the devices of the measuring system is shown in Fig. 4.3.3.

For the electrical tunneling measurements, it is necessary to achieve low temperatures within 4.2 K. so that, the liquid helium has been used. At the beginning of the measurement process, a significantly smaller current about (1 μ A) has been applied to avoid the destruction of the junctions contact. In the same time, the gain set at value 1 K (normally written 1000x). The tunneling measurement of $V(I)$ or $R(T)$ can be achieved after input all required data in an installed Labview program.

Even though the smallest deviation in the ohmic line, it can be precisely detected by using a lock-in amplifier Labview. To provide full information about the symmetry in superconductor material, one has to perform differential resistance measurements. Lock-in is a device very sensitive to a small resistance; therefore the total contact resistance in a sample should be not greater than 1 k Ω . Otherwise is not possible to measure a sample has a high resistance, for example, reach some M Ω . Thus, the system is optimized for samples with low resistance.

The spectra of differential resistance (dV/dI) versus current created via the connected lock-in amplifier. In this way is not performed a differential resistance but various voltage (V_{ac}) over current. In order to calculate the (dV/dI) from the actual measurements, thus the spectrum of dV/dI could be calculated by multiplying V_{ac} at a factor R/V_{ac} *. In the following shows how to calculate it.

$$R_{diff} = (dV/dI) = V_{ac} \cdot R/V_{ac}^*$$

$R_{diff} = (dV/dI)$ is the differential resistance for all measured values, V_{ac} is the various voltage R is the normal junction resistance which can calculate from I - V characteristic

V_{ac}^* is the average value which is taken from the measured data V_{ac} vs. I

Thus the result is for this calculation obtained a spectrum of differential resistance (dV/dI) vs. I (or it can set vs. V).

However, this way needed long time (more than one hour) for each attempt, since it is required to measure spectrum at the temperature from 4.2 K to temperature above the T_c of used material. In this case, the electrical behavior in the sample may be not remaining stable during changing their temperature or from a high resistance to a low resistance. For this reason, there is an alternative way one can get differential resistance temperature dependence from the measured I - V . This is a numerical derivative; it is possible to be done by origin lab or similar software. Thus it doesn't require an additional measurement time. To reduce the noise that may appear in numerical derivative for I - V , one can do a curve smoothing after differentiation. In this work, the first way has been followed.

To characterize and prove the behavior of Josephson junctions and exclude the idea of a pin hole in the sample's Josephson Junctions, we have to investigate the Shapiro steps by testing it under microwave irradiation that realizes by placing a sample on a measuring rod is shown in Fig. 4.3.2. The measuring rod contains an antenna and a coil, where an antenna used for coupling of microwave radiation within the range between 2 GHz to 20 GHz and the coil is for investigation of the influence of magnetic fields.

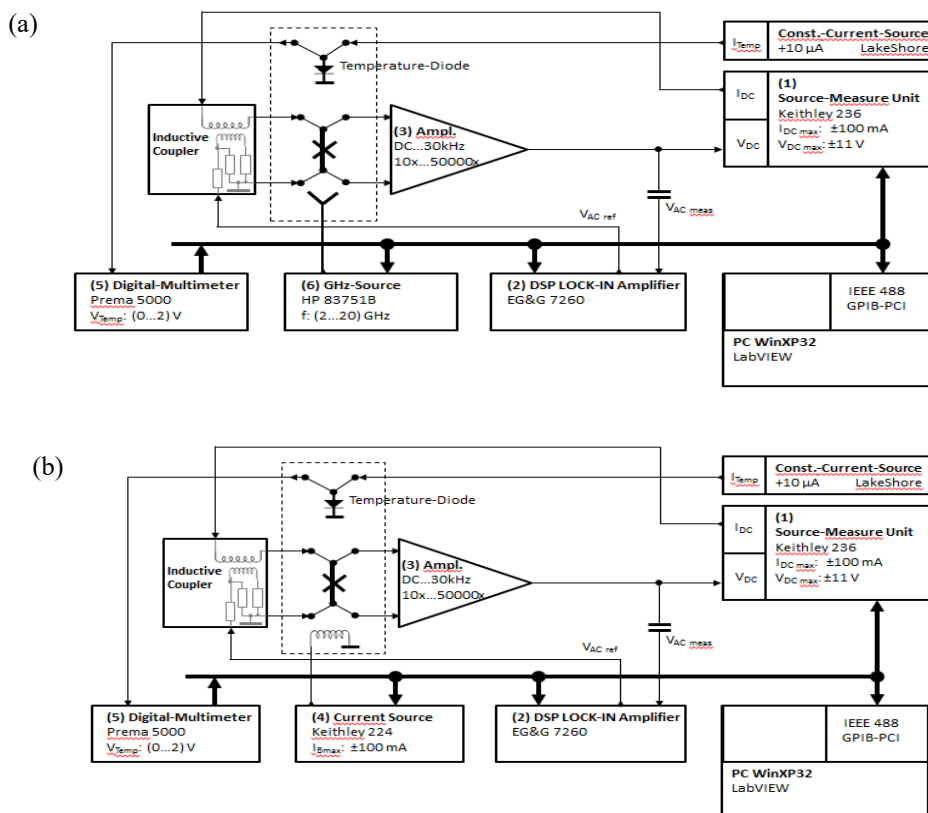


Fig. 4.3.1: A schematically image of the used devices illustrated in figure 4.3.3., PC-based measurement system with connected microwave (a) and lock-in amplifier (b).

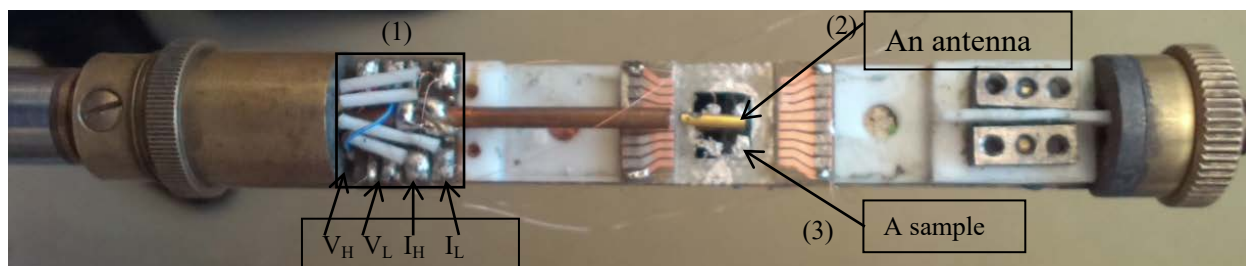


Fig. 4.3.2: A photo image of a measuring rod. The first part (1) has respective four solder joints for low and high current (I_L , I_H), low and high voltage (V_L , V_H). The second part (2) is an antenna which is used to measuring microwave irradiation. The third part (3) is a sample installed below the antenna.

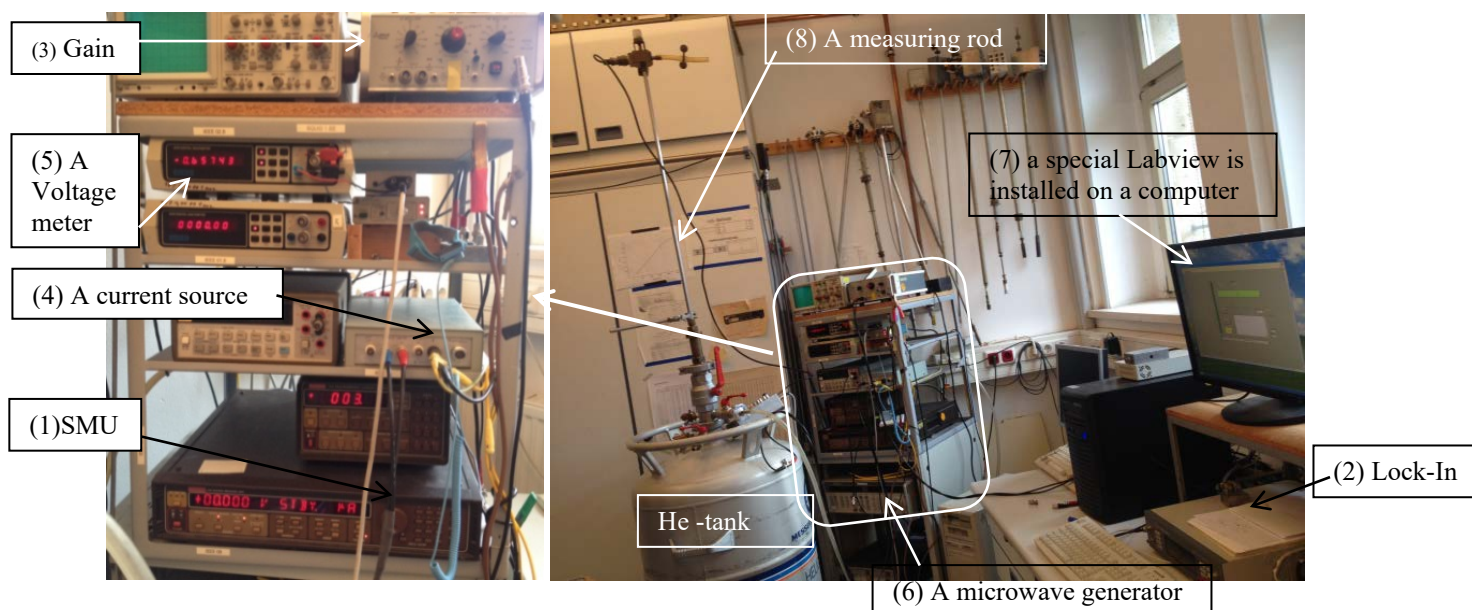


Fig. 4.3.3: A photo image of used devices in electrical measuring.

4.4. TECHNIQUES TO FABRICATE POINT CONTACT

The point contacts (PC) were made by using the standard mechanical classical technique (a point contact measuring rod), in which a metallic tip is pressed along c-axis the sample surface of Co: Ba-122 single crystals. Due to the pressing pressure of the tip can be the contact resistance adjusted. The nature oxide of the metal acts as insulation barrier thus that allows measuring tunneling spectra. Experimental arrangement for PC measurements is shown in Fig. 4.4, a schematic circuit (a), the sample placed on measuring rod (c). Other possible method called soft technique illustrated in (b). This method made by putting a spot of a material like In or Ag on the sample's surface. We will not go deep to discuss it. Because in this work used the former method (standard mechanical classical technique). However, as a metallic tip, we used niobium (Nb) as conventional superconductor electrode as well as Au-tip. Possible switch from Andreev Reflection dominated spectrum to the tunneling regime. In order to describe the carrier transport through crystal surface, one has to get

information about contact radius of the tip. Each of these contacts can fulfill the ballistic condition or inelastic scattering model that depend on the contact radius (a), electron mean free path (l), coherence length (ξ), which is necessary to be known to interpret the model, see section 2.9/Ch.2, is discussed there. The diameter of the tip used in this work is about 0.67 μm , 0.8 μm , for the gold and niobium respectively. However, the disadvantage in the point contacts is extremely sensitive to mechanical influences which cause to change the contacts resistance thus changes the electrical properties and spectra of the sample during the measurement. This made it difficult to measure the temperature dependence of a spectrum with stable contact resistance.

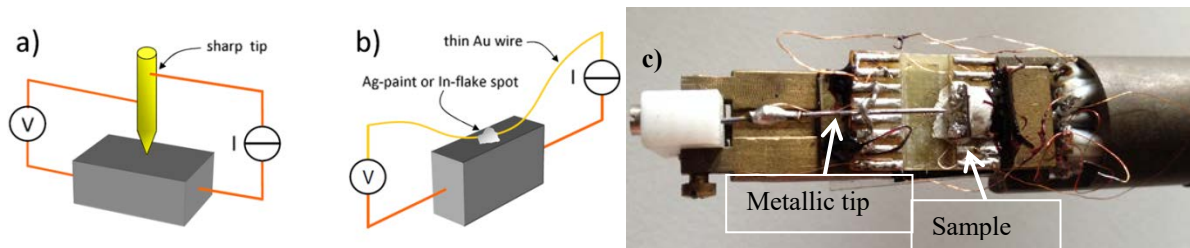


Fig. 4.4: Schematic layout (a) Tip point contact. b) Soft way: by putting a small drop of silver paste on the fresh sample surface. [61]. (c) The measuring rod illustrates a sample of single crystal and a metallic tip.

5. EXPERIMENTAL RESULTS

5.1 PLANAR HYBRID JUNCTIONS BASED ON UNDOPED SINGLE CRYSTALS

5.1.1 CURRENT VOLTAGE CHARACTERISTIC

Since the superconducting crystals were only limited in numbers and not always available in superconducting quality, the fabrication process and electrical measurements of planar hybrid Josephson junctions were initially tested on undoped BaFe_2As_2 single crystals, where the undoped Ba-122 crystals act as a base electrode. After the successful fabrication on undoped one, the thin film technology was transferred to superconducting Co-doped BaFe_2As_2 single crystals.

In the next paragraph, the results of electrical measurements were based on the undoped single crystals. Since they were undoped materials, they were behaving like a metal, thus the expected junctions type in such case would be formed (N^*NS) or (N^*INS). Planar hybrid junctions of single crystal base electrode (N^*) and s-wave conventional Pb/In thin film counter electrode (S) were used. An artificial gold barrier (N) was used with thickness (5-10) nm. An oxides insulator layer (I) may occur in such pnictide crystals, it is assumed as the insulator or degraded layer. The Ba-122 single crystals were produced by the Karlsruhe Institute of Technology by a self-flux method. In shipping letter from Karlsruhe, the materials were called Twox1228 (for undoped single crystals) and Twox925 (for doped single crystals). Thus to distinguish between the results of different electrical behavior, they will be named as it is with different letters corresponding to the numbers of junction samples.

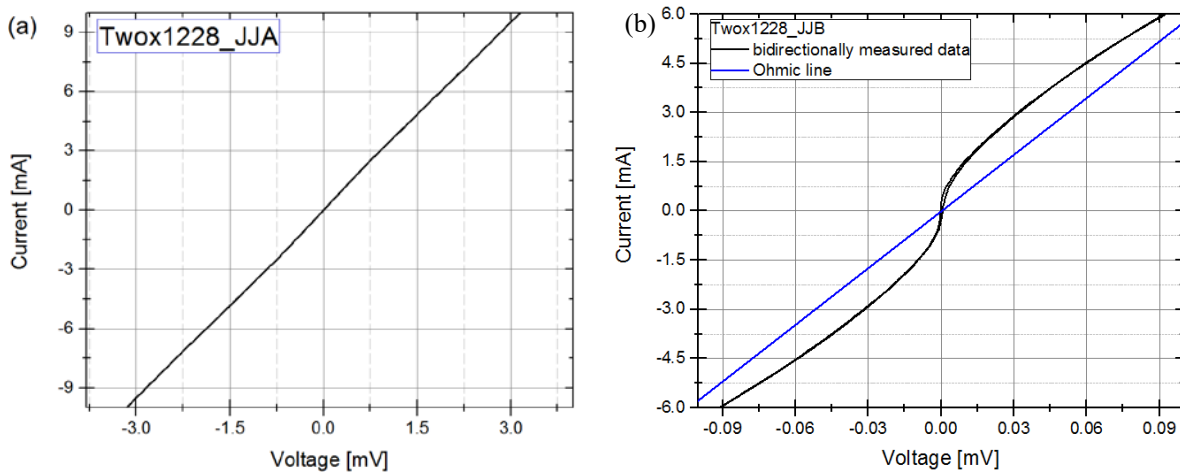


Fig. 5.1.1: (a) *I-V* characteristics from junction with a 5 nm Au barrier and an area of $15 \times 15 \mu\text{m}^2$ measured at 4.2 K. (b) *I-V* characteristics from junction with a 10 nm Au barrier and an area of $15 \times 15 \mu\text{m}^2$ measured at 4.2 K. The curve compared with Ohmic line (blue).

The *I-V* characteristic of a planar junction of an undoped sample (Twox1228_JJA) is shown in Fig. 5.1.1 (a), which is nearly linear. This is as expected for behavior of a N^*NS junction. The normal junction resistance is calculated for about 0.23Ω . One can assume that a high transmission may lead to an occurrence of Andreev reflection at the N/S interface [62].

Fig. 5.1.1 (b) shows another sample (Twox1228_JJB), a planar hybrid junctions of undoped crystal/Au/PbIn measured bidirectional at 4.2 K. in contrast to I-VC of sample before Fig. 5.1.1 (a) (Twox1228_JJA). The I-VC in Fig. 5.1.1 (b) shows more strongly nonlinear curve compared to Ohmic line (blue). One can distinguish clearly that there is a flux flow of current behavior with a value of ± 0.65 mA positive and negative branches respectively at a nearly zero voltage. The corresponding normal junction resistance (R_N) is about 16.01 m Ω .

5.1.2 SPECTROSCOPY

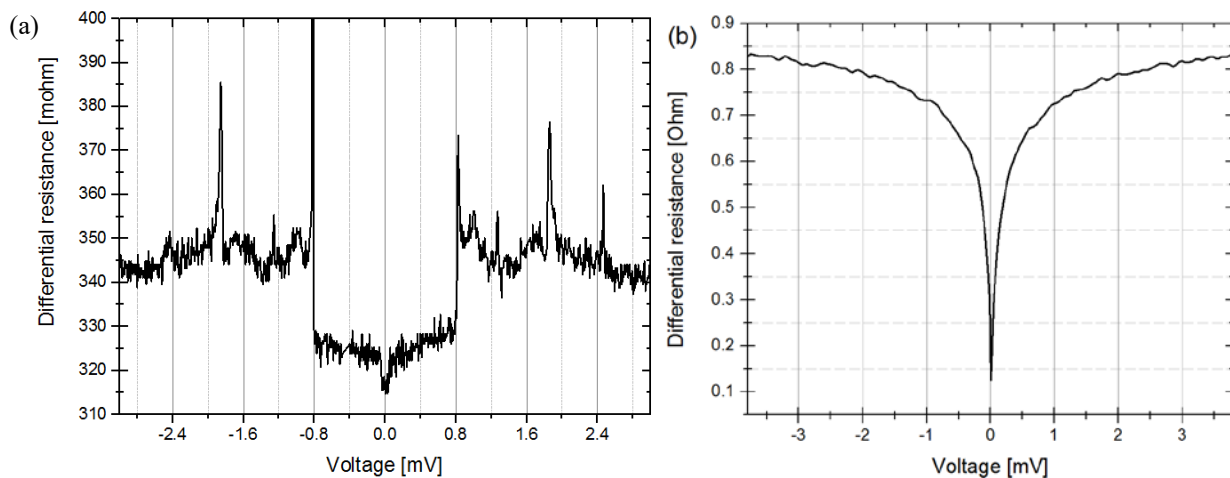


Fig. 5.1.2: (a) Differential resistance vs. voltage of Au-barrier junction measured at 4.2 K for the sample in fig. 5.1.1 (a). (b) Differential resistance vs. voltage Au-barrier junction measured at 4.2 K for the sample in fig. 5.1.1 (b).

The spectroscopy is a method of investigation of the tunneling contact. That offer ways to determine the energy gap(s) in the superconductor. Here differential resistance of a sample illustrated in Fig. 5.1.1 (a) which should be included in the temperature range of 4.2 K which is less than the respective T_c of lead. Fig. 5.1.2 (a) shows the differential resistance spectrum vs. Voltage. Thus, the most feature of the differential curve may come from Pb counter electrodes, which is the only superconductor material in this tunneling case. Thus, the features are shown in the positive and negative branch of about 0.8 mV, 1.9 mV and 2.5 mV. The energy gap for Pb superconducting ($2\Delta_{Pb}$) is about 2.55 meV. [64]

The case of nonlinearity in Fig. 5.1.1 (b) is also confirmed by spectroscopy measurements. This can be seen in the differential resistance curve in Fig. 5.1.2 (b) which shows V-shape and is totally different from the sample before in Fig. 5.1.2 (a). The reason for this difference could be caused via changing the thickness of the barrier, or it could be the thin insulator sputtered layer is incomplete covering between superconducting electrode and single crystal base electrode that cannot exclude with planar junction design.

Again the features caused by the gap of Pb superconductor which may exhibit energy gap $2\Delta_{Pb}$ equals ± 2.5 meV. There are some noises came from thermal effect during the measurements that cannot exclude.

5.2 PLANAR HYBRID JOSEPHSON JUNCTIONS BASED ON CO-DOPED BA-122 SINGLE CRYSTALS

In addition to the measurements of undoped single crystals tunneling junctions, this work focused on the Josephson effect based on the processed materials of doped single crystals ($\text{Ba}(\text{Fe}_{1-x}\text{Co}_x)_2\text{As}_2$ ($x \approx 0.06$, $T_c = 23.5$ K)), and its characterization of the different types of barrier.

This section discusses the planar Josephson junctions based on the Co-doped single crystal (Co-doped: Ba-122)/ a barrier/PdIn. For the characterization of the Josephson effects, it will be presented that temperature dependent I-V characteristic which fitted within the RCSJ model. $I_c R_N$ -product and its temperature dependency were investigated. Interesting $I_c R_N$ - T dependencies suggest a possible $0-\pi$ transition, which may imply the s_{\pm} symmetry of the order parameter in the pnictide electrode. Additionally, it will be showing the formation of Shapiro steps under microwave radiation and the variation of the critical current as a function of the applied magnetic field.

We will name the samples as follow (Twox925_JJA, Twox925_JJB, Twox925_JJD and Twox925-JJC). All junctions are technically prepared under the same conditions with only a small difference in their junction area and junction barrier type. The junction area ranges from $15 \times 15 \mu\text{m}^2$ (Twox925_JJA, Twox925_JJB and Twox925_JJD) to $25 \times 25 \mu\text{m}^2$ (Twox925-JJC). The artificial barrier for the tunneling junctions consisted of thin sputtered or thermally evaporated layers of various materials, metals (like Au) as well as insulators (TiO_x , SiO_x). Titanium was used as insulator barrier by oxidation in ambient atmosphere. It could observe different types of electrical behaviors, which they will be discussed in the following. The differences in the electrical behavior are assumed to be arbitrary artifacts associated with variations of the surface properties of single crystals, which the reasons could either come from the pnictide surface or intrinsic or even coming from the required steps before the junction fabrication.

5.2.1 CURRENT VOLTAGE CHARACTERISTIC & TEMPERATURE DEPENDENCE

Co-doped: Ba122 single crystal/Au-barrier/PbIn

Fig. 5.2.1 (a) shows a sample (Twox925_JJD), which is planar hybrid Josephson Junctions of Co: Ba-122 single crystal/Au-barrier/PbIn. The I-V-characteristic curve converges from the ohmic line so it shows no Josephson effect. Nevertheless it is more like tunneling behavior. The result is in conformity to planar junction based on Co: Ba-122 thin film contains Au barrier [81] or another barrier type is TiO_x -barrier junction [82] and observed also in [83] for grain boundary junctions. There is still a resistance in the junction of about 0.7Ω as it is shown the differential resistance vs. I (Fig. 5.2.1(a)). The critical current (I_c) value is assumed to be of about 0.4 mA and junctions resistance $R_N = 1.5 \Omega$ which results $I_c R_N$ -product can be estimated to 0.6 mV. The I-V characteristic is symmetric in both branches.

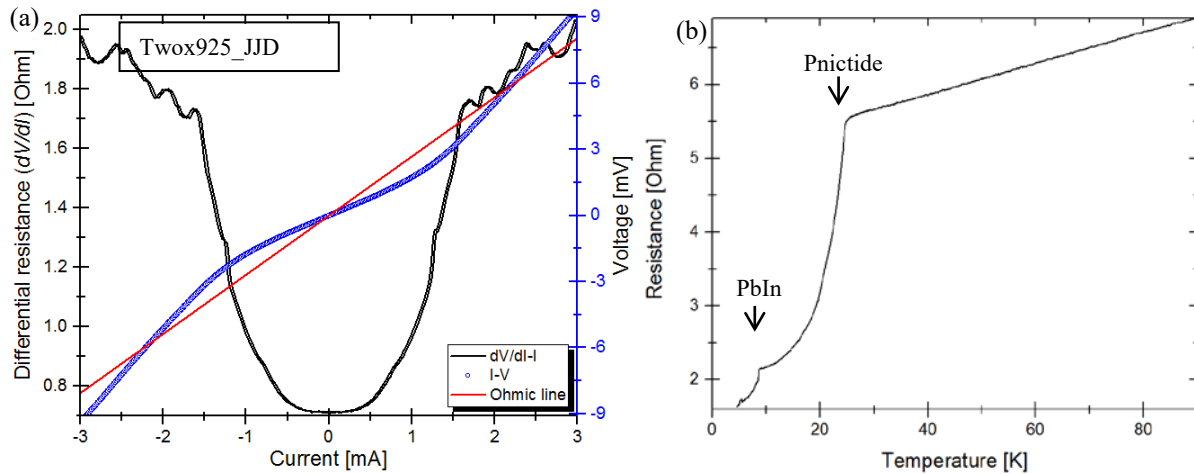


Fig. 5.2.1: (a) I - V characteristics (blue) from junction with a 10 nm Au-barrier and an area of $15 \times 15 \mu\text{m}^2$ measured at temperature 4.2 K compared with an ohmic line (red). Its differential resistance vs. current included in the figure, too. (b) Temperature dependence of the junction resistance of a Ba-122/Au/Pb with a junction area is of $15 \times 15 \mu\text{m}^2$. The arrows show the T_c of Ba-122 and Pb, where both electrodes become superconducting.

In Fig. 5.2.1 (b), the temperature profile of the resistance of a Josephson junction, the temperature dependence of the resistance shows linear behavior above 30 K. This is typical for a metal-like barrier. Thus, it can be emphasized that we have normal metal since the junction has been formed by such thin Au layer barrier at thickness 10 nm which was also used as a protection layer. Clear features, as expected, are in the critical temperatures of the lead counter electrode and the pnictide crystal (Co-doped: Ba-122) to be recognized for transition at $T_c = 23.5$ K, $T_c = 7.3$ K, respectively. Therefore the behavior of the junction contact can be described as a part of the BTK-model [62]. As can be seen $R(T)$ curve, this curve profile does not reach the origin so it is still small resistance at about 1.5 Ω . That is the reason why there is no Josephson behavior occurred in this sample.

Co-doped: Ba122 single crystal/TiO_x-barrier/PbIn

In the following, there will be described the result on doped single crystals for sample's name Twox925_JJA, which is planar hybrid Josephson Junctions of Co-doped single crystal/TiO_x/Pb. Fig. 5.2.2 (a) shows the temperature dependence of the junction resistance measured with a bias current of 100 μA . The curve shows two drops at temperatures of 23.5 K and 7.5 K. These values correspond to the critical temperatures of the pnictide base electrode out of single crystal material and the counter electrode of the Pb/In films, respectively. The curve of $R(T)$ shows a foot-like shape that may be caused by thermally activated phase slips (TAPSs) [84].

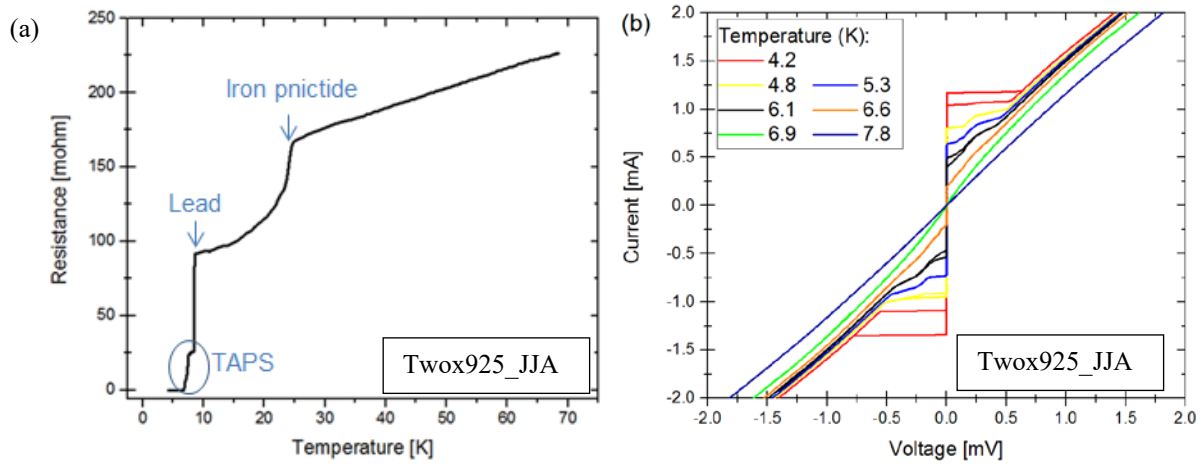


Fig. 5.2.2: (a) Temperature dependence of the junction resistance with a junction area is of $15 \times 15 \mu\text{m}^2$. The foot-like shape may be caused by TAPSs [84], the arrows on the T_c of Ba-122 and Pb, respectively.[85] (b) I-V characteristics from junction with a 10 nm TiO_x barrier and an area of $15 \times 15 \mu\text{m}^2$ measured at different temperatures as illustrated in the inset.[85]

This junction shows a typical I-V characteristic, see Fig. 5.2.2 (b). The asymmetric I-V curves are clearly visible when compared to an ohmic line. This asymmetry may happen due to trapped flux in the junction, like in [73], [86]. Josephson behavior can be described within the RCSJ-model [56, 57]. The fitting parameters extracted from I-V characteristics Fig. 5.2.2. The measured curve at 4.2 K and fit model is shown in Fig. 5.2.3 (a). The fit parameters are critical current $I_c = 1170 \mu\text{A}$ in the positive branch and a normal state resistance $R_N = 868 \text{ m}\Omega$, in the negative branch I_c is $1340 \mu\text{A}$ and $R_N = 874 \text{ m}\Omega$. The corresponding $I_c R_N$ -products are about $1020 \mu\text{V}$ and $1150 \mu\text{V}$ for the positive and negative branches respectively. One can conclude that the TiO_x /single crystals interfaces may play an important role and have an influence. Since the insulator layer was formed by subsequently oxidization, it may become thicker leading to larger $I_c R_N$ -products. In these junctions an excess current of about $I_{ex} = 0.4 \text{ mA}$ occurs at 4.2 K. That excess reduces the critical current and the product of $I_c R_N$. In such junctions a possible source for excess currents is an Andreev reflection dominated transport regime [62, 87] which also appeared in other experimental results with junction containing normal barriers (SNS*) [73, 81]. This junction may contain normal metal, since the sample was protected by an Au layer of thickness 50 nm which is sputtered some steps before junction preparation. We cannot deny the existence of any leftovers in spite of nominally complete removal.

The junction with this I_{ex} influence shows a hysteretic I-V curve corresponding to a McCumber parameter of $\beta_C = 2eI_c R_N^2 C / \hbar$, $\beta_C > 1$. Fitting delivers values of about $\beta_C = 1.76$ (positive branch) and $\beta_C = 3.11$ (negative branch). Temperature dependencies of the corresponding $I_c R_N$ -products show high $I_c R_N$ -product at 4.2 K and an almost linear decrease at temperatures up to T_c (see Fig. 5.2.3 (b)). The temperature dependence of the $I_c R_N$ product agrees with SNS type junctions discussed in [88].

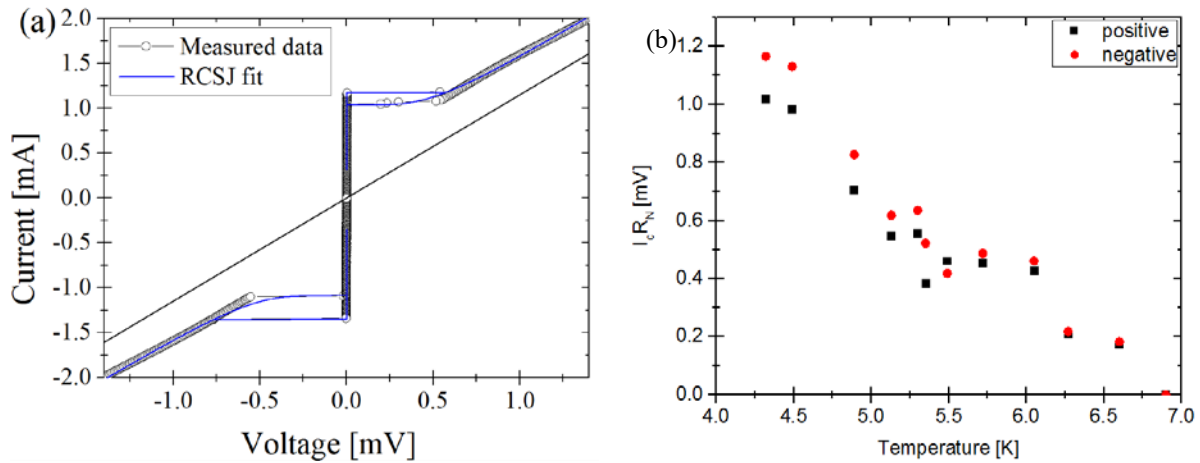


Fig. 5.2.3: (a) I - V characteristics fitted with RCSJ-model (blue line) [89]. (b) Temperature dependencies of the $I_c R_N$ -product, which included excess current. [85]

Co-doped: Ba122 single crystal/TiO_x-barrier/PbIn

For junctions with thick TiO_x barrier for Twox925_JJB Josephson effect was observed. The typical I - V characteristic of the junctions is shown in Fig. 5.2.4. (a).

This junction shows the critical current $I_c = 330 \mu\text{A}$ with a high excess current $I_{ex} = 280 \mu\text{A}$. We first briefly discussed the reasons of I_{ex} . We assumed the reason of high I_{ex} in this sample is related to the larger carrier mean free path compared with the junction dimension of an area of $15 \times 15 \mu\text{m}^2$, lead to larger I_{ex} . Consequently, that reason can be more plausible, in spite of all the samples have almost the same junction area and the extracted value of I_{ex} differ for each sample. However, we can exclude this reason since it is discussed by Waldram [90] the case of large junctions with linear temperature dependence [87]

Our paper about the excess current interpreted some other reasons in more details [89]. I rewrote, for example, “Andreev reflection, leads to a temperature dependence of the excess current similar to the one of the gaps of the lower T_c electrode, which is in our case lead with a BCS-like behavior [87]”.

The measured data at 4.2 K was modeled by RCSJ-model [56, 57] and taking excess current (I_{ex}) into account. Fig. 5.2.4 (b), which shows the fitted curve with an excess current $I_{ex} = 280 \mu\text{A}$. Correspond to this fit, the critical current $I_c = 330 \mu\text{A}$ and normal junction resistance $R_N = 41.5 \text{ m}\Omega$ produce $I_c R_N$ -product equals $13.7 \mu\text{V}$. In contrast to the former sample, the $I_c R_N$ -product is comparatively small. It could be for many reasons for example; the I_c in this sample appears to be 4 times lesser in comparison with I_c occurred in the sample before. R_N of tunneling junction in the sample before is to be 21times higher. The reason of lowering I_c could be an influence of magnetic impurities in the interface area or an external magnetic field. Other possible reasons could be either coming from the pnictide surface [91] or the required steps before the junction fabrication. Nevertheless, the result of $I_c R_N$ -product is close to one which was observed in another work on pnictide thin film base electrodes [73].

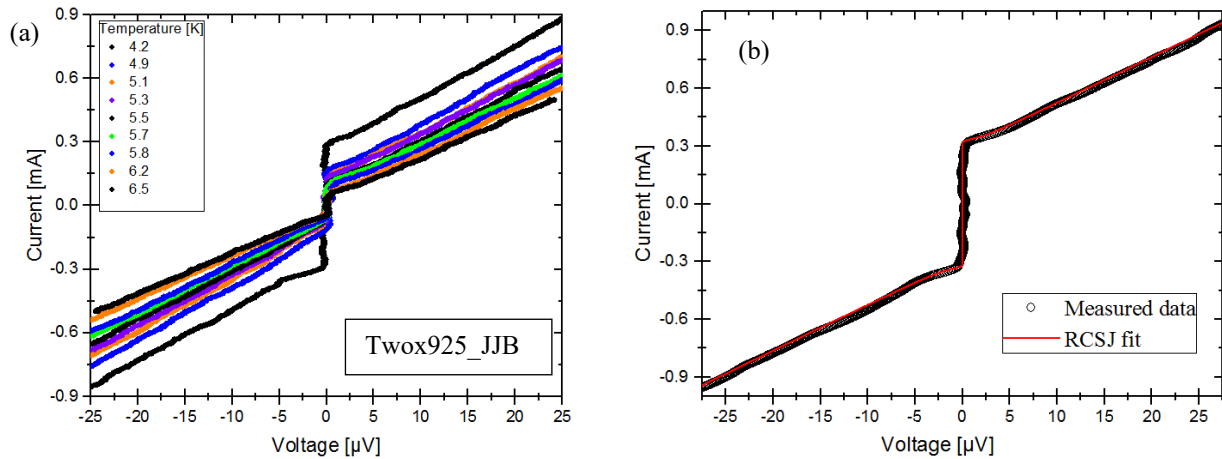


Fig. 5.2.4: (a) I - V characteristics from junction with a 10 nm TiO_x barrier and an area of $15 \times 15 \mu\text{m}^2$ measured at different temperatures as illustrated in the left box. [92] (b) I - V characteristics fitted with RCSJ- model (red line). Parameters of fit are given in the text. [92]

These junctions also show symmetric, non-hysteretic (McCumber $\beta_c < 1$) I - V characteristics. β_c in this junction is about 0.06. To be able to investigate the origin of I - V characteristic in more detail and get information about it, we show temperature dependencies of the extracted values of I_c , $I_c - I_{ex}$ to get reduced critical current (I_c^*), and the excess current (I_{ex}). Consequently, these values are taken within a wide range of different I - V characteristics in the junction, see Fig. 5.2.4. (c), where the I_{ex} vanishes for temperatures $T < T_c$ and the inclined to be linear. Whereas the I_c^* overlaps with critical current then decrease for temperatures significantly smaller than T_c nearly at 4.8 K and increases almost linearly again. I_c reached a maximum value near the critical temperature of I_{ex} , tilted slightly, then come back at $T > 5.4$ K to get linearly increase. Unconventional I_c^* dependence may be related to a possible 0 - π transition like this behavior observed in junctions, with ferromagnetic barriers using electrodes with an s_{\pm} -symmetry of the order parameter [16]. This behavior is also discussed in [21] to identify s_{\pm} -wave symmetry in FBS.

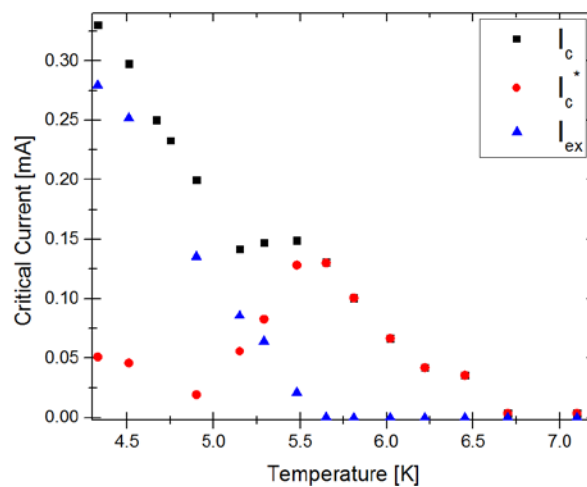


Fig. 5.2.4 (c): Temperature dependence of the critical current (I_c) (square), reduced critical current by excess current (I_c^*) (circles), excess current (I_{ex}) (triangle). [92]

Co-doped: Ba122 single crystal/TiO_x-barrier/PbIn

The I-V characteristic of (Twox925-JJC) is shown in Fig.5.2.5 (a). Josephson effect was clearly observed for the barrier junction also used thick TiO_x. The typical I-V characteristic of the junctions is symmetric without influence of excess current (I_{ex}) taking into account and no hysteresis occurs. The measured data at 4.2 K was modeled by RCSJ-model [56, 57]. Corresponding to this fit, the critical current ($I_c = 64.1 \mu\text{A}$) and normal junction resistance ($R_N = 0.186 \Omega$) produce $I_c R_N$ -product equals $11.9 \mu\text{V}$. Thus it is close to one which was observed in another work on pnictide thin film base electrodes [73].

$I_c R_N - T$ dependencies is shown in Fig.5.2.5 (b). It can be seen that the temperature profile of the critical current is decreased almost linearly so conventional $I_c R_N$ vs. T behavior. It differs significantly from the curve prediction by Ambegaokar and Baratoff.

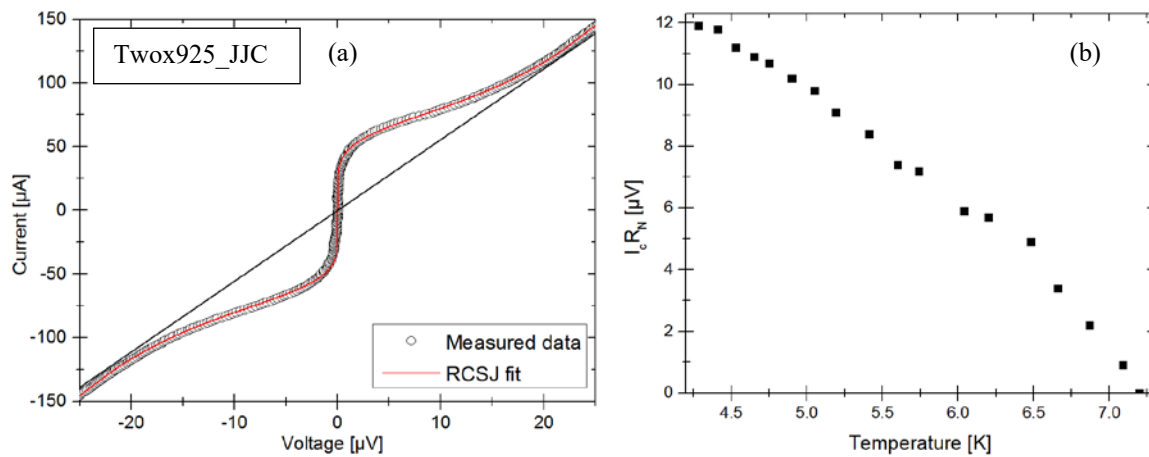


Fig.5.2.5: (a) I-V characteristics from junction with a 10 nm TiO_x barrier and an area of $25 \times 25 \mu\text{m}^2$ measured at different temperatures as illustrated in the left box. The inset figure: I-VC measured at 4.2 K and fitted within RCSJ-model (red line). Parameters of fit are given in the text. (b) Temperature dependence of the critical current (I_c). [89]

5.2.2 MICROWAVE IRRADIATION

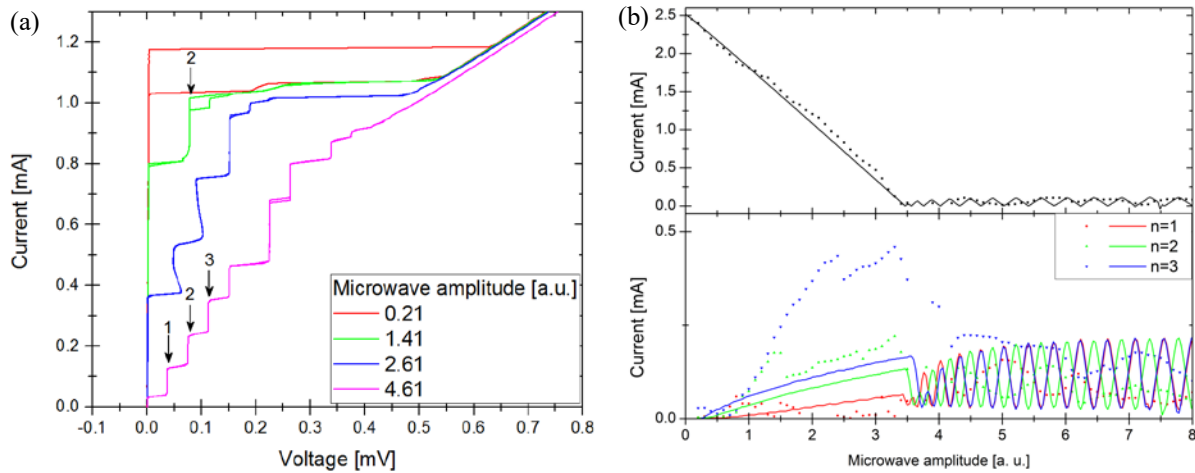


Fig. 5.2.6: (a) selected I-V characteristics from junction in fig. 5.2.3 under different microwave amplitude (a.u.) measured at 18 GHz. the arrows mark the first Shapiro steps. (b) Zeroth Shapiro step (top) and higher steps $n = 1, 2, 3$ (bottom) as function of microwave amplitude (measured at 18 GHz). Measured data are shown as squares, whereas simulations are represented as straight lines, simulations with $\Omega=0.03$. [85]

The Josephson junctions were tested under microwave irradiation for the Josephson junction sample Twox925_JJA. Fig. 5.2.6 (a) shows clear formation of Shapiro steps were observed with different microwave amplitude for junction shown in Fig. 5.2.3 (a), where their steps are marked with arrows and numbers. In the upper of Fig. 5.2.6 (b) shown the critical current with microwaves, which is suppressed completely with applied external frequency at 18 GHz, see in the down of Fig. 5.2.6 (b) which also shows unusual behavior of the step at $n=3$. This step height dependence on power is higher than those for $n=1, 2$. This seems to be similar to the behavior reported in [93]. The measured data are compared with simulations based on the second Josephson equation [94]. The relative frequency $\Omega = h/2e * f_{mw} / I_c R_N$ calculated from I-V characteristics is 0.03. This is very low, which leads to only small maxima of the Shapiro steps, which is in contrast to the values of the measured data. Possible reasons could be non-sinusoidal current-phase relations [95] or resonance steps caused by LC-Shunts [96].

The I-V characteristic of the Josephson junctions for sample Twox925_JJB in Fig. 5.2.4. (a) test under microwave irradiation is shown in Fig. 5.2.7 (a), Shapiro steps could be observed. The steps values calculated corresponding to the Josephson equation $V_n(f_{mw}) = n(h/2e)f_{mw}$, with the f_{mw} as the frequency of the irradiated microwaves. The steps (n) also are marked with arrows and numbers which are as expected constant voltages at different n -integer values. The shape of the modulation of the critical current as well as the higher order Shapiro steps compared with simulations based on the second Josephson equation [94]. This simulation depends on the parameter which is the relative microwave frequency $\Omega = \omega_{mw} / \omega_c$, ω_c is the characteristic frequency in the junctions that lead to $\Omega = h/2e * f_{mw} / I_c R_N$. The fitted value used for simulation is $\Omega=0.30$, critical current with including an excess current. Fig. 5.2.7 (b) shows that the normalized critical current (I_c) suppressed completely as

the first Shapiro step. This simulation with a sinusoidal current-phase relation leads to the assumption the excess current behaves like a Josephson current under microwave irradiation.

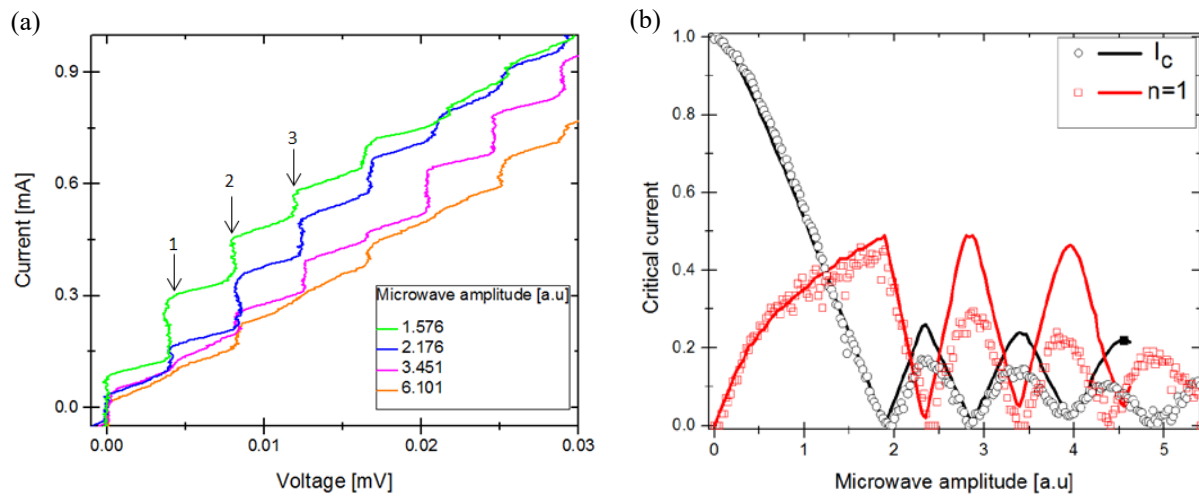


Fig. 5.2.7 (a) I - V characteristic under different microwave amplitudes (a.u.) measured at 2 GHz at $T=4.2$ K. for the junction shown in fig. 5.2.4 (a) Normalized critical current (I_c) and first Shapiro-step ($n=1$) vs. microwave amplitude (measured at 2 GHz). Measured data are shown as circles and squares, whereas simulations with $\Omega=0.30$ are represented as straight lines. [92]

5.2.3 MAGNETIC FIELD DEPENDENCE

This section discusses the dependence of the critical current I_c on the applied magnetic field based on SIS & SNS Josephson junctions. They based on different geometries such as planar hybrid, and corner junction.

For the planar junction geometry can be realized along the c -axis of the superconductor. Fig. 5.2.8 shows investigations within external magnetic fields show a network-like modulation of I_c , incomplete suppression up to 150 μ T, and no similarity to the Fraunhofer pattern. This is a clear indication that the current density distribution of the contact and thus the barrier is not homogeneous.

S-wave and extended s-wave likes s_{\pm} -wave or s_{++} -wave assumed and accepted to the multi-gap pnictide superconductor which shows normally a central peak like in the Fraunhofer diffraction pattern data, but changes in the side part structure. The central peak like can indicate for such symmetry.

Due to geometrical reason with planar junctions, it could be investigated that the symmetry with more suitable experiments by using either phase sensitive devices [9, 10], [11, 97] or a corner-SQUID [98], and even edge junctions. As the symmetry of the cuprates was confirmed d-wave nature by such experiments using corner junctions or corner SQUIDs [32]. Despite the c -axis transport, the electron velocities are mostly ab -directed (due to nearly cylindrical Fermi sheets), and c -axis component is much less. Thus it is a favorite to use phase-sensitive geometry devices.

In the following discussion, there is another geometry kind of “corner junction”⁽¹⁾ a proposal presented by Atkinson Mora [99]. Fig. 5.2.8 (b), shows an example of a corner-like Josephson junction, that show, in particular, Josephson- effects (inset figure) with the magnitudes of I_c 10 μ A. it presented very clear a central pattern of I_c vs. B-field. A central amplitude of I_c feature that suppressed a periodicity in the field axis, periodically with amplitudes much lower than the central and became a minimal field in I_c . This single central peak of I_c around the zero flux point in external magnetic fields shows Fraunhofer-like structure.

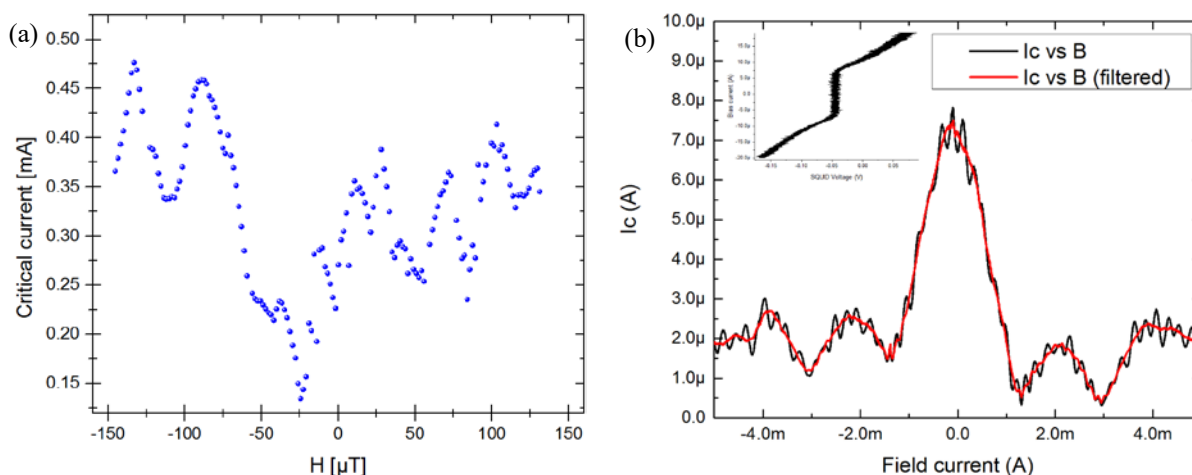
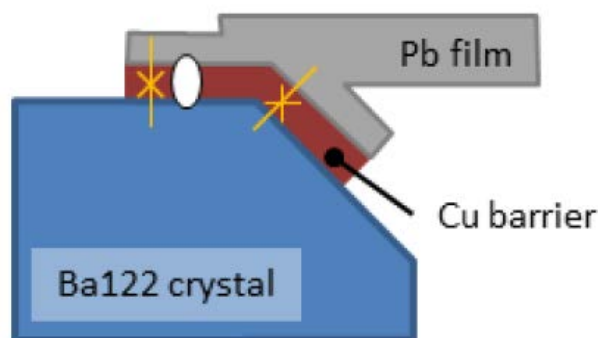


Fig. 5.2.8: (a) Critical current versus magnetic field based on I - V characteristics for sample Twox925_JJB measured at 4.2 K [85]. (b) Critical current versus magnetic field based on I - V characteristics shows in the inset figure, Junction geometry designed by corner junction. [99]

⁽¹⁾ Figure below shows a schematic view of the SNS corner junction Co:doped: Ba-122/ Cu-barrier/ Pb. The corner junction made with 135° angle. The elliptical white shape illustrated a broken barrier creating a split junction case. This junction plays an important role in electrical transport within the ab-plane single crystals. [99]



The schematic view of the corner junction

5.2.4 SPECTROSCOPY

Co-doped: Ba122 single crystal/TiO_x-barrier/PbIn

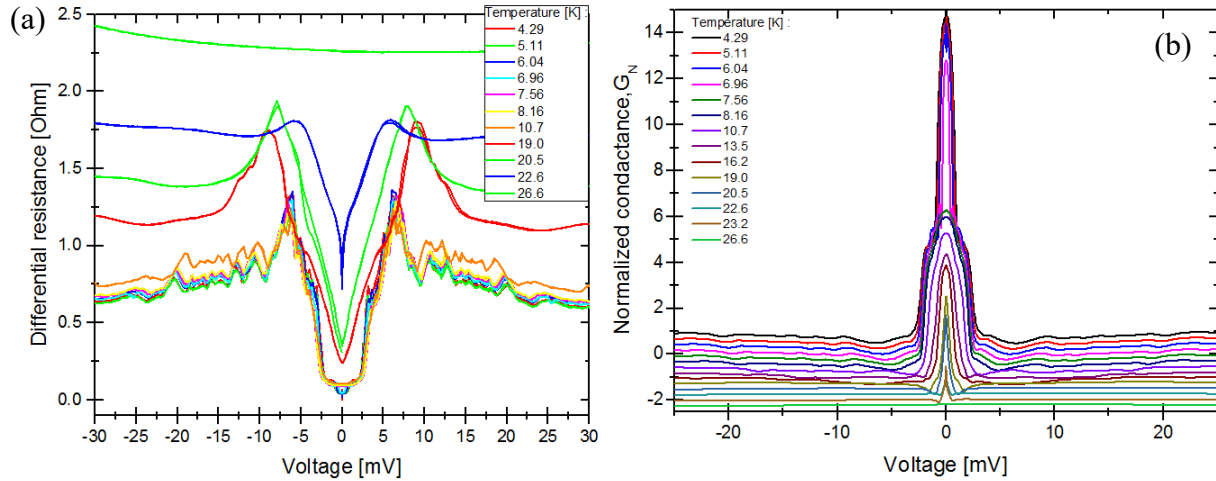


Fig. 5.2.9: (a) differential resistance vs. voltage measured at different temperatures between 4.2 K and 26.6 K. (b) Normalized conductance vs. voltage of TiO_x planar junction measured at different temperatures. Spectra are shifted against each other by 0.25. [92]

To obtain information about the symmetry superconducting order parameter, and for the determination of the value of energy gaps, one uses spectroscopy measurements. Therefore the differential spectra of planar hybrid pnictide single crystal/ TiO_x-barrier/ Pb Josephson junctions was measured for different temperatures as illustrated in Fig. 5.2.9 (a).

The observed results show central peaks with multiple features which disappeared when the spectra are measured above the T_c of lead and then showing V-shaped curves that may be caused by Andreev reflection corresponding to NS interface.

Above the T_c of the pnictide crystal, all features disappear completely as shown in the straight green line at $T = 26$ K. This represents the normal differential resistance in the junctions. In order to ensure better comparability, the analysis of experimental spectra results leads to a normalized conductance [64], $G_N = (dI/dV)_{NS} / (dI/dV)_{NN}$. That allows obtaining information about the superconducting OP. Thus the calculated normalized conductance shows a zero bias conductance peak ZBCP in the conductance-V characteristics; see Fig. 5.2.9 (b). The conductance spectra can be described within the extended BTK-model [62], including extensions multiband character of FBS and broadening effect of Dynes parameter (Γ) [100]. To do that, we take a conductance spectrum at the temperature above the critical temperature of the Pb counter electrode.

The model also contains barrier strength which represents dimensionless parameter (Z) that depends on the transparency $\tau_N = 1 / (1 + Z^2)$ in the junction, here Z , in this case, seems to be about 1, which could be estimated from the following. The planar junction with TiO_x-barrier has $R_N = 41.5$ m Ω and the junction dimension of about 15×15 μm^2 . Corresponding resistivity of contact area is $\rho = 70$ $\mu\Omega \cdot \text{cm}$. As was shown in [101], bulk resistivity for Co-doped Ba-122 with $x = 0.06$ is $\rho \approx 100$ $\mu\Omega \cdot \text{cm}$. The range of true values is

expected to be 50-200. The resistivity of the artificial structure with tunneling barrier is close to that of bulk single crystal without any barrier.

The energy gap are determined to be $\Delta_1 = 2.4$ meV, $\Delta_2 = 8.4$ meV. These values coincide with the literature [102]. Concerning the symmetry of the gap, it can be concluded through the conductance-V spectra. The scale has a value reached to 8 in conductance-scale that can be excluded s-wave symmetry which should be typically up to 2, even it is not expected to FBS to be d-wave symmetry but it is similar result found in [8]. Thesis's Döring [58] also used a model with d-wave to fit his spectra results.

Co-doped: Ba122 single crystal/ AlO_x -barrier/PbIn

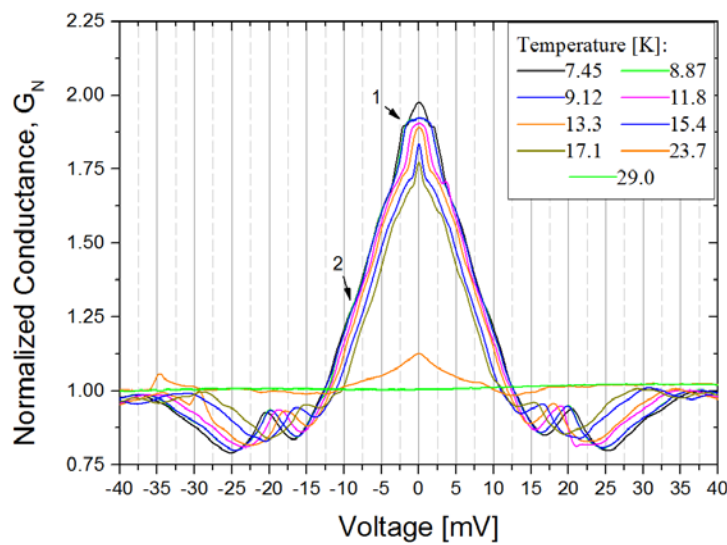


Fig. 5.2.9: Normalized conductance vs. voltage of AlO_x -barrier planar junction from junction with an area of $15 \times 15 \mu\text{m}^2$, which measured at different temperatures illustrated in right box. Arrows marked for $\Delta_1 = 2.2$ meV and $\Delta_2 = 8.5$ meV. [92]

Planar Junction was prepared by using barrier of aluminum oxide material Co:Ba-122/ AlO_x /PbIn. The I-V characteristics with this type barrier show no Josephson behavior with of a barrier thickness 9 nm but transport mechanism are dominated by Andreev reflection, the reason could be caused by getting thicker oxidization layer since we formed the insulator layer by subsequent oxidization under normal atmosphere. Similar to the other works which used thick metal gold barrier and an insulator barrier, both based on pnictide thin film [82,83], respectively. However, one can get conductance spectra with the stable normal junction resistance of about 9.17Ω . The resulting temperature dependence of conductance spectra in such a junction is shown in Fig. 5.2.9 measured at $T > 7.2\text{K}$ so the Pb counter electrode is in the normal state. One can see a ZBCP surrounded by dips. The value of normalized conductance is smaller 4 times than the sample before (Fig. 5.2.9 (b)).

One also can observe two gaps marked with arrows at values of $\Delta_1 = 2.2$ meV and $\Delta_2 = 8.5$ meV at 7.45 K, which occur as a steep increase of conductance. At a voltage of 20 mV, there can be observed another peak structure as a third feature. This peak is not associated with a

superconducting gap, but occurs due to electron-phonon interactions usually at energies $E=\Delta_2+\Omega_{\text{Ph}}$, with Ω_{Ph} as a typical boson energy. Typically values are around 12 meV for Co:Ba-122 [103].

5.3 POINT CONTACT ANDREEV REFLECTIONS AND TUNNELING SPECTROSCOPY

5.3.1 NIOBIUM TIP PRESSED ON UNPROCESSED SURFACE OF SINGLE CRYSTALS

The tunneling spectroscopy has been made on the untreated surface of doped $\text{Ba}(\text{Fe}_{1-x}\text{Co}_x)_2\text{As}_2$ single crystals by using Nb point contact. The electron tunneling is performed along the c-axis of the single crystals. Fig. 5.3.1 shows, the shape of the calculated normalized conductance which gives features which do not much differ from that of planar junctions in Fig.5.2.9 (b). In contrast to PC, the JJs offer a favored way which is carried out through the stability of the junction resistance even if there are changes in temperature or some tuning of junction area and thickness barrier as well. For these reasons, in case of the PC it is just taken one measured curve at 4.2 K. The normal junction resistance is about 5.2Ω .

The spectrum was measured at 4.2K, at which niobium is superconducting. Therefore, depending on the barrier transparency, the tunneling junction contact is either SIS^* or SNS^* , where I is the assumed oxidize layer. Insulator barrier could result either from the surface of the single crystal or from the Nb tip. Since the SIS is a tunneling junction measured at 4.2 K, we cannot make a description through BTK-model which works for a normal metal/superconductor junction (NS) or NIS.

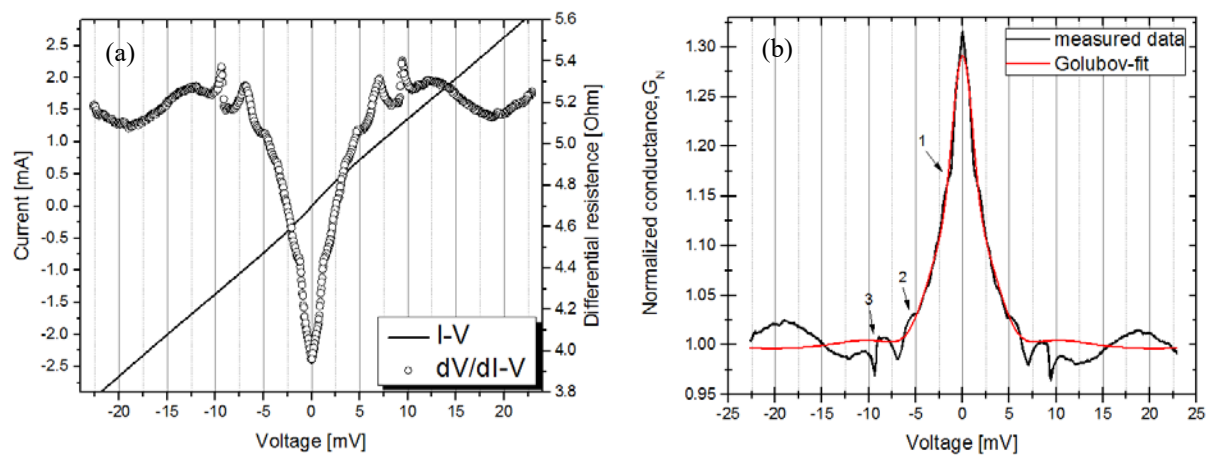


Fig. 5.3.1: (a) I - V characteristics from doped single crystal and Nb tip measured at 4.2 K. its Differential resistances vs. voltage of contact measured directionally at 4.2 K. (b) Normalized conductance vs. voltage measured at 4.2 K, the black and red line represents measured data and Golubov -fit, respectively. Arrows with 1, 2, 3 numbers represent Δ_{Nb} , Δ_1 , and Δ_2 for Ba-122, respectively. [92]

From the conductance spectrum analysis Fig. 5.3.1 (b), as it can be seen, the gaps values can be determined to be about 4.9 meV (small gap) and 8.5 meV (large gap) for the Ba-122 electrode. They are close to values which were observed in [102]. Since we showed a conductance spectrum taken at the temperature 4.2 K, thus the superconducting effect by the influence of Nb electrode is not excluded. Therefore the spectra also show small peaks in the positive and negative voltage branch at ± 1.5 mV that could be caused by the energy gap of Nb (Δ_{Nb}), which is about 1.5 meV [104]. The gap features would correspond to $\Delta_1 + \Delta_{\text{Nb}}$ and $\Delta_2 + \Delta_{\text{Nb}}$, and, correspondingly, the determined gap values for Ba-122 can be reduced by $\Delta_{\text{Nb}} \approx 1.5$ meV.

However, we tried to fit these conductance spectra with Golubov-model; even if it is not possible with two superconductors' electrodes (SIS or SNS) but we have to think about how much the influence of Nb tip as a superconductor, since the tip quality is affected over the time with the atmosphere. For this reason we assumed it behaves like a metal. In Fig. 5.3.1 (b), we can see that the model and the measured data have been significantly fitted on each other in the period of $-5\text{mV} \geq V \geq 5\text{mV}$, while in the other periods; we can see obviously small changing of the fitting pattern which fails to catch up the small features of the measured data. These are most likely caused by electron-boson interaction spectra and, therefore, it could be interpreted in the context of complex Eliashberg theory, similar to spectra studied by another group [102] on a Ba-122 single crystal.

The other work by Gonnelli [105] they lowered the BCS-ratio for the large gap to 5.5 - 6, and the shoulders in conductance spectra corresponding to the "BCS-ratio" 7- 8, they referred to the signature of a bosonic mode.

Within this model, the barrier strength is included. It is fitted to be of about $Z=10$. The fitted gaps values are the same assumed values before to be about 4.9 meV and 8.5 meV for Ba-122 electrode.

To analyze the spectra with more detailed it can be concluded that the unconventional ZBP in Fig. 5.3.1 (b) may correspond to that of d-wave symmetry [106]. The d-wave symmetry of the order parameter is not adopted for FBS, which would, however, seem very unlikely on these materials, if compared to other PCAR data published in literature over the past years. That could be estimated from the following. The conductance spectra curve (Fig. 5.3.1 (b)) which is less than 2 cannot be obtained with d-wave symmetry of the gaps. It could be done with an s-wave one. One can consider sufficiently relevant for s_{\pm} -wave symmetry of the gaps like other publication [5].

5.3.2 NIOBIUM TIP PRESSED ON PROCESSED SURFACE OF SINGLE CRYSTALS

The samples in this section are prepared by using niobium (Nb) tunneling point contacts on doped $\text{Ba}(\text{Fe}_{1-x}\text{Co}_x)_2\text{As}_2$ single crystals for sample name Twox925_PC2. The preparation performed by a sharp tip of a Nb electrode pressed along the c-axis of the polished surface of single crystals. Fig. 5.3.2 (a) shows the temperature dependence of the contact resistance. The curve shows two drops at temperatures of about 23.5 K and ~ 9.2 K which correspond to the T_c of the pnictide single crystal and the Nb tip, respectively. The $R(T)$ curve also displays that is not passing through the origin. That may be the case because of the relatively high carrier transportation rate. In contrast to this case the behavior of junctions showing Josephson effects gives an indication for a critical current and leads to $R(T)$ curves passing through the origin about that see section 5.2. A typical I-V characteristic is given in Fig. 5.3.2 (b), shows obviously a nonlinear behavior which is confirmed by measuring the differential resistance (dV/dI) vs. voltage spectra at 4.2 K. On the other hand, the value of the dV/dI spectra at zero voltage is equal to 200 m Ω which is the same minimum value of $R(T)$ as in Fig. 5.3.2 (a).

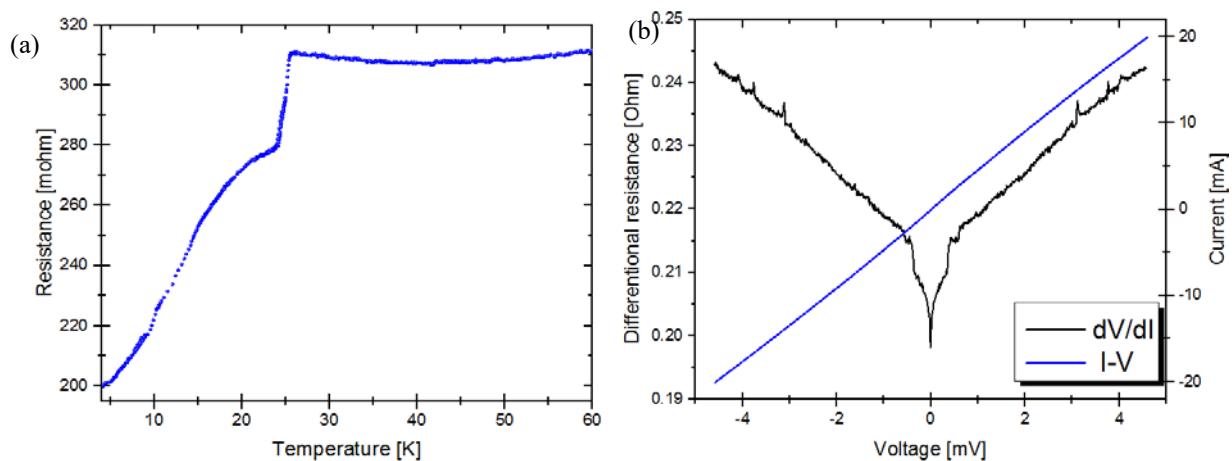


Fig. 5.3.2: (a) Temperature dependence of the contact resistance obtained from a Co-doped single crystal and Nb electrode. (b) I-V characteristics and its differential resistance measured at 4.2 K.

The measured differential resistance spectra at different temperatures in Fig. 5.3.3 (a) show V-shaped central peaks that may be caused by Andreev reflection. In order to evaluate these data, again an extended BTK-model is used [58]. SN type can be used for Andreev- and tunneling spectroscopy, if it is measured at temperature above the critical temperature of the Nb tip. The observed results show central peaks with multiple features which decreases with the increasing of the temperature and just disappeared above the T_c of the crystal as shown by the green line at $T=26.2$ K in Fig. 5.3.3 (a). As well as it shows spread in bias voltage (energy spectra), which may correspond to the broadening parameter Γ [100]. The gap value is determined to be about 3 meV for Ba-122 electrode which is close to one value which was observed in [102], where they showed two gap values of $\Delta_1=3.8$ meV and $\Delta_2=8.2$ meV. The spectra also show small peaks in the positive and negative voltage branch at ± 1.5 mV that may be caused by the gap of Nb Δ_{Nb} , which is about 1.5 meV [104].

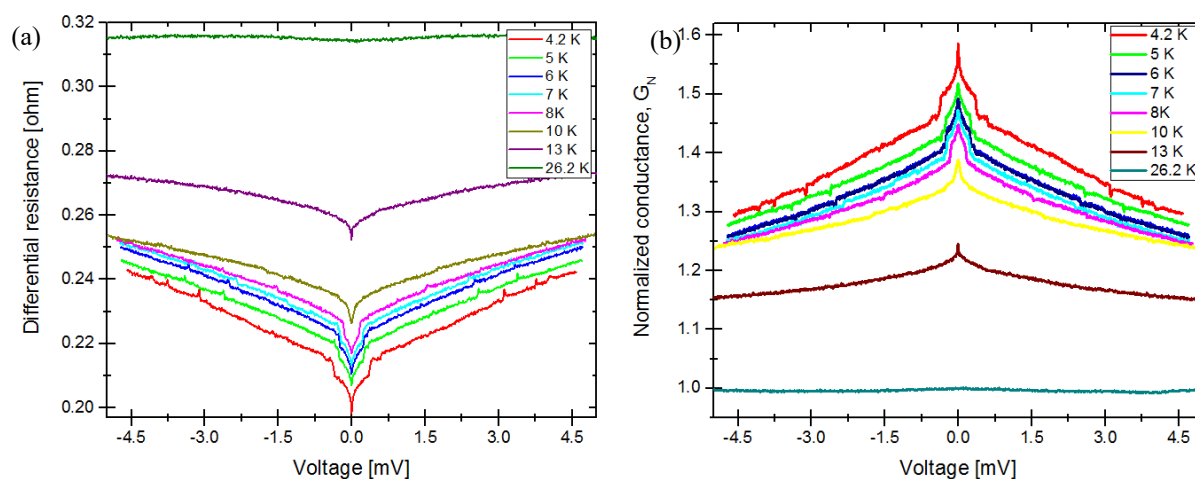


Fig. 5.3.3: (a) Differential resistance vs. voltage of contact at different temperatures. (b) Normalized conductance of contact at different temperatures.

5.3.3 GOLD TIP PRESSED ON PROCESSED SURFACE OF SINGLE CRYSTALS

PCAR has reported again on Co:Ba-122 single for samples name Twox925_PC3 which have a polished surface structure by using metallic Au tip is pressed along the c-axis. The differential resistance is measured and shown in Fig. 5.3.4 (a). The similar shape also is shown for hybrid planar junctions Ba-122/Au/PbIn (N*NS), see Fig. 5.1.2 in section 5.1. The normalized conductance is calculated and shown in Fig. 5.3.4 (b). The spectrum is like the samples interpreted before by the extended BTK-model and shows spreading in energy that may lead by broadening Dynes parameter. Similar spectrum measured by using Au tip from another group [107], in our sample shows there is a larger junction resistance of 0.233 Ω .

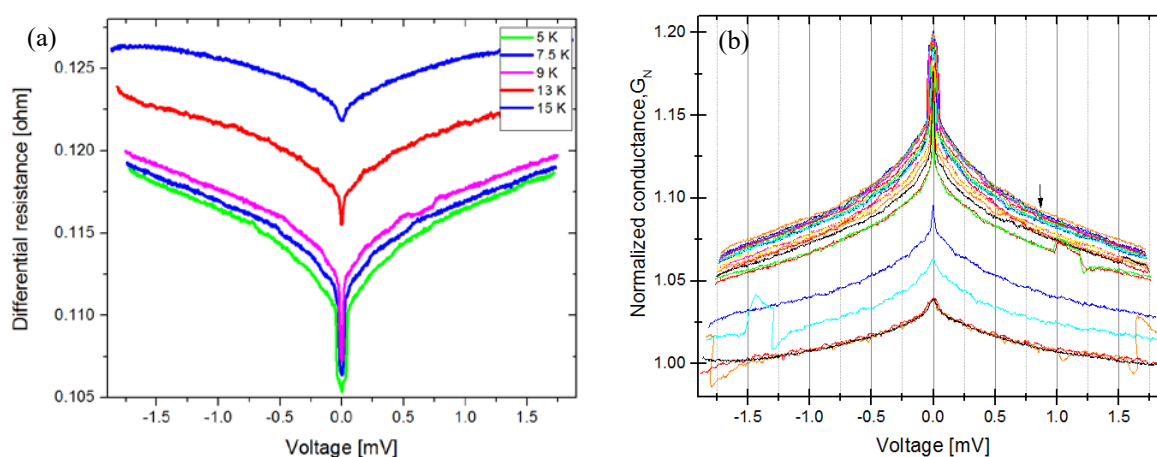


Fig. 5.3.4 : (a) Differential resistance vs. voltage of contact at different temperatures. (b) Normalized conductance of contact vs. voltage at different temperatures from 4.2 K to 26.5 K.

5.3.4 DIFFICULTIES IN THE POINT CONTACT SPECTROSCOPY MEASUREMENTS

Different spectrum and junction resistance from Nb point contact accomplished on the unprocessed surface of pnictide Co-doped single crystal shown in Fig. 5.3.5 (samples Twox925_PC4). There are three different spectrum shapes of differential resistance vs. voltage. The differential electrical behavior came from the same sample measured at $T = 4.2$ K. that shows an unstable contact resistance which is changing for each spectrum shape. For these reasons, the fabrication of hybrid planar junctions is more favor with artificial barrier than point contacts, although the fabrication process is complicated and need a long time.

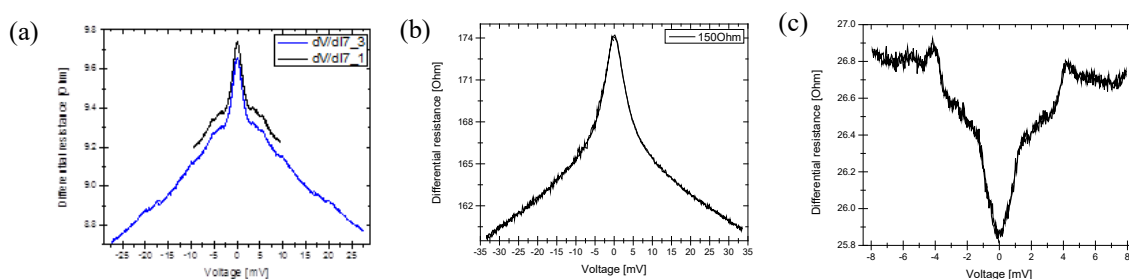


Fig. 5.3.5: (a), (b), (c) Differential resistance vs. voltage based on the same contact measured at $T = 4.2$ K.

6.1 SUMMARY AND CONCLUSIONS

In this work, it has been realized to fabricate and investigate of the Josephson junctions based on iron pnictide $\text{Ba}(\text{Fe}_{1-x}\text{Co}_x)_2\text{As}_2$ single crystals (Co:Ba-122) using established thin-film process. The designed layout was achieved for the first time worldwide which is a planar hybrid Josephson junctions. The c-axis planar junctions were achieved, in which were tested different barriers such as the intrinsic barrier, or metal barrier (gold) then were further developed to use the insulating barrier (titanium oxide, aluminum oxide).

The high surface quality is required since it utilizes the procedure of the photolithographic preparation process used for thin film technologies. However, the single crystals materials have rough surface structure; therefore it was necessary to develop a new polishing method which made it possible to reduce the surface roughness of crystals to less than 5 nm. Other difficulties in the work were connected to the small dimensions of the sample $2 \times 2 \times 0.25$ mm or even less after cleaving the single crystal, which allows preparing only one single junction on a crystal.

Another problem is an influence of degradation can be caused by using water, chemical removal (like acetone), and oxidation in the air as well. The solutions for all these issues are mentioned, it can be found in chapter 4. There are other difficulties with the insulating layer between the pnictide electrodes and the lead counter electrodes, which are probably due to problems with the chemical removals and lithography planar mask. To avoid that it was attempted to making several insulating layers by using subsequent with different masks. Despite these difficulties, the planar Josephson junction on Ba-122 single crystals could be successfully achieved.

The planar Josephson junction design allows measuring the electrical properties of these junctions like resistance on temperature on each electrode and the junctions itself as well as temperature dependent current-voltage characteristics and differential conductance vs. voltage. The planar hybrid Josephson junction design has been tested first on undoped single crystals. SN-tunneling junctions are formed for spectroscopic studies of these contacts with a gold barrier.

Josephson effects observed in planar junctions between Co: Ba-122 pnictide materials and conventional s-wave superconductor counter electrodes. The investigation of Josephson junctions showed that the RCSJ-model can be used to describe the experimental I-V characteristics. However, there were excess currents at several sample types, which were included in the model. The determination of the $I_c R_N$ -product gives information on the characteristic quality of the Josephson junctions. The $I_c R_N$ -product of the Interface- TiO_x barrier could be realized up to 1.15 mV which is the highest value reported in literature up to now.

The advantage of high values of those $I_c R_N$ -products increased the possibilities for applications like superconducting quantum interference devices (SQUID). The quantitative study of the microwave response has been performed within this work. The measured microwave modulation could be described by the simulations, which suggest a Josephson nature of the excess current.

The modulation of the critical Josephson current in the external magnetic field was investigated. However, this differs significantly from the expected Fraunhofer pattern, may be caused by the inhomogeneity of the barrier.

Additionally, results from tunneling and Andreev spectroscopy i.e. temperature dependent dI/dV - V spectra are shown. Through the measured spectra of differential resistance, and calculated differential conductance, the energy gaps values were determined to about $\Delta_1 = 2.4$ meV, and $\Delta_2 = 8.4$ meV in agreement with others results published in the literature.

Summarizing, a new thin film technology was realized to use pnictide single crystals as an electrode of tunneling junctions. The measurements show a good quality of the junctions and will be helpful to explain the physics of the superconducting in the iron-based materials.

REFERENCES

- [1] Y. KAMIHARA, H. HIRAMATSU, M. HIRANO, R. KAWAMURA, H. YANAGI, T. KAMIYA, AND H. HOSONO, “Iron-Based Layered Superconductor: LaOFeP”; *J. Am. Chem. Soc.*, 128, 10012-10013 (2006).
- [2] Z.-A. REN, W. LU, J. YANG, W. YI, X.-L. SHEN, Z.-C. LI, G.-C. CHE, X.-L. DONG, L.-L. SUN, F. ZHOU, Z.-X. ZHAO, “Superconductivity at 55 K in Iron-Based F-Doped Layered Quaternary Compound Sm[O_{1-x}F_x]FeAs”; *Chin. Phys. Lett.*, 25, 2215-2216 (2008).
- [3] A. YAMAMOTO, J. JAROSZYNSKI, C. TARANTINI, L. BALICAS, J. JIANG, A. GUREVICH, D.C. LARBALESTIER, R. JIN, A.S. SEFAT, M.A. MCGUIRE, B.C. SALES, D.K. CHRISTEN, D. MANDRUS, “Small anisotropy, weak thermal fluctuations, and high field superconductivity in Co-doped iron pnictide Ba(Fe_{1-x}Co_x)₂As₂”; *Appl. Phys. Lett.* 94, 062511 (2009).
- [4] L. FANG, Y. JIA, V. MISHRA, C. CHAPARRO, V. K. VLASKO-VLASOV, A. E. KOSHELEV, U. WELP, G. W. CRABTREE, S. ZHU, N. D. ZHIGADLO, S. KATRYCH, J. KARPINSKI AND W. K. KWOK, “Huge critical current density and tailored superconducting anisotropy in SmFeAsO_{0.8}F_{0.15} by low-density columnar-defect incorporation” ; *Nat. Commun.* 4, 2655 (2013).
- [5] I. I. MAZIN, D.J. SINGH, M.D. JOHANNES, M.H. DU, “Unconventional Superconductivity with a Sign Reversal in the Order Parameter of LaFeAsO_{1-x}F_x”; *Phys. Rev. Lett.*, 101, 057003 (2008).
- [6] Z. ZHANG, A. F. WANG, X. C. HONG, J. ZHANG, B. Y. PAN, J. PAN, Y. XU, X. G. LUO, X. H. CHEN, AND S. Y. LI, “Heat transport in RbFe₂As₂ single crystals: Evidence for nodal superconducting gap”; *Phys. Rev. B*, 91, 024502 (2015).
- [7] H. KONTANI AND S. ONARI, “Orbital Fluctuation Mediated Superconductivity in Iron Pnictides: Analysis of the Five Orbital Hubbard-Holstein Model”; *Phys. Rev. Lett.*, 104, 157001 (2010).
- [8] J.-PH. REID, M. A. TANATAR, A. JUNEAU-FECTEAU, R. T. GORDON, S. RENE DE COTRET, N. DOIRON-LEYRAUD, T. SAITO, H. FUKAZAWA, Y. KOHORI, K. KIHOU, C. H. LEE, A. IYO, H. EISAKI, R. PROZOROV, L. TAILLEFER, “Universal heat conduction in the iron arsenide superconductor KFe₂As₂: evidence of a d-wave state”; *Phys. Rev. Lett.*, 109, 087001, (2012).
- [9] D. PARKER, I.I. MAZIN, “Possible Phase-Sensitive Tests of Pairing Symmetry in Pnictide Superconductors”; *Phys. Rev. Lett.*, 102, 227007 (2009).

References

- [10] W.-Q. CHEN, F. MA, Z.-Y. LU, F. ZHANG, “ π Junction to Probe Antiphase s-Wave pairing in Iron pnictide superconductors”; *Phys. Rev. Lett.*, 103, 207001 (2009).
- [11] J. WU, P. PHILLIPS, “Experimental detection of sign-reversal pairing in iron-based Superconductors”; *Phys. Rev. B* 79, 092502 (2009).
- [12] M. M. PARISH, J. HU,; B. A. BERNEVIG, “Experimental consequences of the s-wave $\cos(k_x)\cos(k_y)$ superconductivity in the iron pnictides”; *Phys. Rev. B* 78, 144514 (2008).
- [13] A. A. GOLUBOV, A. BRINKMAN, Y. TANAKA, I.I. MAZIN, O.V. DOLGOV, “Andreev Spectra and Subgap Bound States in Multiband Superconductors”; *Phys. Rev.Lett.* 103, 077003 (2009).
- [14] S. APOSTOLOV, A. LEVCHENKO, “Josephson current and density of states in proximity circuits with s_{\pm} superconductors”; *Phys. Rev. B* 86, 224501 (2012).
- [15] C. S. LIU, J.Y. CHANG, W.C. WU, C.-Y. MOU, “Possible s(+/-)-wave pairing evidenced by mid gap surface bound states in Fe-pnictide superconductors”; *J. Phys. Cond. Mat.* 25, 365701 (2013).
- [16] J. LINDER, I. B. SPERSTAD, A. SUDBO, “0- π phase shifts in Josephson junctions as a signature for the s(+/-)-wave pairing state”; *Phys. Rev. B* 80 020503 (2009).
- [17] I. B. SPERSTAD, J. LINDER, A. SUDBO, “Quantum transport in ballistic s(+/-)-wave superconductors with interband coupling: Conductance spectra, crossed Andreev reflection, and Josephson current”; *Phys. Rev. B* 80, 144507 (2009).
- [18] E. BERG, N. H. LINDNER, T. PEREG-BARNEA, “Metastable π Junction between an s(+/-)-Wave and an s-wave superconductor”; *Phys. Rev. Lett.*, 106, 147003 (2011).
- [19] S.-Z. LIN, “Josephson effect between a two-band superconductor with s plus or s +/- pairing symmetry and a conventional s-wave superconductor”; *Phys. Rev. B* 86, 014510 (2012).
- [20] C. NAPPI, S. DE NICOLA, M. ADAMO, E. SARNELLI, “Model prediction of high temperature π -states in iron pnictide superconductor-insulator-superconductor Josephson junctions”; *Europhys. Lett.* 102, 47007 (2013).
- [21] D. WANG, H.-Y. LU, Q.-H. WANG, “The Finite Temperature Effect on Josephson junction between an s-Wave Superconductor and an s_{\pm} -Wave Superconductor”; *Chin. Phys. Lett.*, 30, 077404 (2013).

References

- [22] F. HARDY, T. WOLF, R. A. FISHER, R. EDER, P. SCHWEISS, P. ADELMANN, H. V. LOEHNEISEN, C. MEINGAST, “Calorimetric evidence of multiband superconductivity in $\text{Ba}(\text{Fe}_{0.925}\text{Co}_{0.075})_2\text{As}_2$ single crystals”; *Phys. Rev. B*, 81, 060501(R) (2010).
- [23] F. HARDY, P. ADELMANN, H. V. LOEHNEISEN, T. WOLF, C. MEINGAST “Large Anisotropic Uniaxial Pressure Dependencies of T_c in Single Crystalline $\text{Ba}(\text{Fe}_{0.92}\text{Co}_{0.08})_2\text{As}_2$ ”; *Phys. Rev. Lett.*, 102, 187004 (2009).
- [24] P. SEIDEL, “Applied Superconductivity” ISBN: 978-3-527-41209-9, 1336 (2015).
- [25] P. SEIDEL’S lecture, “Supraleitende Materialien”; summer semester (SS2016)/ <http://www.tieftemperaturphysik.uni-jena.de>.
- [26] K. TANABE & H. HOSONO, “Frontiers of research on iron-based superconductors toward their application” ; *Jpn. J. Appl. Phys.* 51, 010005 (2012).
- [27] U. WELP, C. CHAPARRO, A. E. KOSHELEV, W. K. KWOK, A. RYDH, N. D. ZHIGADLO, J. KARPINSKI, S. WEYENETH, “Anisotropic phase diagram and superconducting fluctuations of single-crystalline $\text{SmFeAsO}_{0.85}\text{F}_{0.15}$ ” ; *Phys. Rev. B* 83, 100513(R) (2011).
- [28] J. GIAPINTZAKIS, W.C. LEE, J.P. RICE, D.M. GINSBERG, ROBERTSON, I.M. R. WHEELER, M.A. KIRK, M.O. RUAULT, “Production and Identification of Flux-Pinning Defects by Electron-Irradiation in $\text{YBa}_2\text{Cu}_3\text{O}_7$ Single-Crystals”; *Phys. Rev. B* 45, 10677-10683 (1992).
- [29] Y. NAKAJIMA, Y. TSUCHIYA, T. TAEN, H. YAGYUDA, T. TAMEGAI, S. OKAYASU, M. SASASE, H. KITAMURA, T. MURAKAMI, “Critical current densities and flux creep rate in Co-doped BaFe_2As_2 with columnar defects introduced by heavy-Ion irradiation”; *Physica C.*, 470, 1103-1105 (2010).
- [30] C. KATZER, C. STAHL, P. MICHALOWSKI, S. TREIBER, F. SCHMIDL, P. SEIDEL, J. ALBRECHT, G. SCHÜTZ, “Gold nano crystals in high-temperature superconducting films: creation of pinning Patterns of choice” ; *New J. Phys.* 15, 113029 (2013).
- [31] J. BARDEEN, L. N. COOPER, AND J. R. SCHRIEFFER, “Theory of Superconductivity” *Phys. Rev.*, 108, 1175-1204 (1957).
- [32] D. J. VAN HARLINGEN, “Phase-sensitive tests of the symmetry of the pairing state in the high-temperature superconductors - Evidence for $d_{x^2-y^2}$ symmetry”; *Rev. Mod. Phys.*, 67, 515-535 (1995).
- [33] M. WAGENKNECHT, ”Korngrenzen-Tunnelspektroskopie am elektronendotierten Kupratsupraleiter $\text{La}_{2-x}\text{Ce}_x\text{CuO}_4$ ”; PhD-Thesis, University Tübingen (2008).

- [34] T. WATANABE, H. YANAGI, T. KAMIYA, Y. KAMIHARA, H. HIRAMATSU, M. HIRANO, AND H. HOSONO, “Nickel-Based Oxyphosphide Superconductor with a Layered Crystal Structure, LaNiOP”; *Inorg. Chem.* 46, 7719-7721 (2007).
- [35] M. TEGEL, I. SCHELLENBERG, R. PÖTTGEN AND D. JOHRENDT, “A ^{57}Fe Mössbauer Spectroscopy Study of the 7 K Superconductor LaFePO” *Solid State Sci.* 10, 193 (2008).
- [36] Y. Kamihara, T. Watanabe, M. Hirano, and H. Hosono, “Iron-Based Layered Superconductor $\text{La}[\text{O}_{1-x}\text{F}_x]\text{FeAs}$ ($x = 0.05\text{--}0.12$) with $T_c = 26$ K” *J. Am. Chem. Soc.* 130, 3296-3297 (2008).
- [37] H. TAKAHASHI, K. IGAWA, K. ARII, Y. KAMIHARA, M. HIRANO, AND H. HOSONO, “Superconductivity at 43 K in an iron-based layered compound $\text{LaO}_{1-x}\text{F}_x\text{FeAs}$ ” *Nature* 453, 376-378 (2008).
- [38] Z.-A. REN, G.-C. CHE, X.-L. DONG, J. YANG, W. LU, W. YI, X.-L. SHEN, Z.-C. LI, L.-L. SUN, F. ZHOU, AND Z.-X. ZHAO, “Superconductivity and Phase Diagram in the Iron-based Arsenic-oxides $\text{ReFeAsO}_{1-\delta}$ (Re = rare earth metal) without F-Doping”; *Europhys. Lett.* 83, 17002 (2008).
- [39] J.-F. GE, Z.-L. LIU, C. LIU, C.-L. GAO, D. QIAN, Q.-K. XUE, Y. LIU, AND J.-F. JIA, “Superconductivity above 100 K in single-layer FeSe films on doped SrTiO_3 ”; *Nature Mater.* 14, 285-289 (2015).
- [40] J. PAGLIONE AND R. L. GREENE, “High-temperature superconductivity in iron-based materials”; *Nature Physics* 6, 645–658 (2010).
- [41] Z.-J. YAO, J.-X. LI, AND Z. D. WANG, “Spin fluctuations, interband coupling and unconventional pairing in iron-based superconductors”; *New J. Phys.* 11, 025009 (2009).
- [42] C.-T. CHEN, C. C. TSUEI, M. B. KETCHEN, Z.-A. REN, AND Z. X. ZHAO, “Integer and half-integer flux-quantum transitions in a niobium–iron pnictide loop”; *Nature Phys.*, 6, 260-264 (2010).
- [43] T. HANAGURI, S. NIITAKA, K. KUROKI, AND H. TAKAGI, “Unconventional s -Wave Superconductivity in $\text{Fe}(\text{Se},\text{Te})$ ”; *Science* 328, 474-476 (2010).
- [44] MA. YANWEI, “Progress in wire fabrication of iron-based superconductors”; *Supercond. Sci. Technol.*, 25, 113001(2012).
- [45] M. ROTTER, M. TEGEL, AND D. JOHRENDT “Superconductivity at 38 K in the Iron Arsenide $(\text{Ba}_{1-x}\text{K}_x)\text{Fe}_2\text{As}_2$ ”; *Phys. Rev. Lett.* 101, 107006 (2008).

- [46] P. J. HIRSCHFELD, M. M. KORSHUNOV AND I. I. MAZIN, “Gap symmetry and structure of Fe-based superconductors”; *Rep. Prog. Phys.* 74, 124508 (2011).
- [47] D. J. SINGH AND M.-H. DU, “Density Functional Study of LaFeAsO_{1-x}F_x: A Low Carrier Density Superconductor Near Itinerant Magnetism”; *Phys. Rev. Lett.* 100, 237003 (2008).
- [48] B. D. JOSEPHSON, “Possible new effects in superconductive tunneling”; *Phys. Lett.*, 1, 251-253 (1962).
- [49] P. W. ANDERSON, “How Josephson discovered his effect”; *Phys. Today*, 23, 23-29 (1970).
- [50] P. W. ANDERSON AND J. M. ROWELL, “Probable observation of the Josephson superconducting tunneling effect”; *Phys. Rev. Lett.*, 10, 230–232 (1963).
- [51] S. ANDERS, M.G. BLAMIRE, F.-IM. BUCHHOLZ, D.-G. CRÉTÉ, R. CRISTIANO, P. FEBVRE, L. FRITZSCH, A. HERR, E. IL'ICHEV, J. KOHLMANN, J. KUNERT, H.-G. MEYER, J. NIEMEYER, T. ORTLEPP, H. ROGALLA, T. SCHURIG, M. SIEGEL, R. STOLZ, E. TARTE, H.J.M. TER BRAKE, H. TOEPFER, J.-C. VILLEGIER, A.M. ZAGOSKIN, A.B. ZORIN, “European roadmap on superconductive electronics – status and perspectives”; *Physica C*, 470, 2079-2126 (2010).
- [52] P. SEIDEL, “Josephson effects in iron based superconductors”; *Supercond. Sci. Technol.*, 24, 043001 (2011).
- [53] V. AMBEGAOKAR, A. BARATOFF, “Tunneling Between Superconductors”; *Phys. Rev. Lett.*, 10, 386-489 (1963).
- [54] V. AMBEGAOKAR, A. BARATOFF, “Tunneling Between Superconductors”; *Phys. Rev. Lett.*, 11, 104-104 (1963).
- [55] M. D. FISKE “Temperature and Magnetic Field Dependences of the Josephson Tunneling Current”; *Rev. Mod. Phys.*, 36, 221-222 (1964).
- [56] W. C. STEWART, “Current-Voltage Characteristics of Josephson junctions”; *Appl. Phys. Lett.* 12, 277 (1968).
- [57] D. E. MCCUMBER, “Effect of ac Impedance on dc Voltage-Current Characteristics of Superconductor Weak-Link Junctions”; *J. Appl. Phys.* 39, 3113 (1968).
- [58] S. DÖRING, “Dünnschicht-Josephson-Kontakte zur Charakterisierung eisenbasierter Supraleiter”; Ph.D thesis, Friedrich Schiller University Jena (2015).
- [59] LEE, A.P., “Effect of Noise on the Current-Voltage Characteristics of a Josephson Junction” *J. Appl. Phys.* 42, 325–334 (1971).

- [60] Z. HUANG AND Z. HU, “Josephson effects in three-band superconductors with broken time-reversal symmetry”; *Appl. Phys. Lett.*, 104, 162602 (2014).
- [61] D. DAGHERO, R. S. GONNELLI, “Probing multiband superconductivity by point-contact spectroscopy”; *Supercond. Sci. Technol.*, 23, 043001 (2010).
- [62] G. E. BLONDER, M. TINKHAM, AND T. M. KLAPWIJK, “Transition from metallic to tunneling regimes in superconducting microconstrictions: Excess current, charge imbalance and supercurrent conversion”; *Phys. Rev. B*, 25, 4515-4532 (1982).
- [63] A. A. GOLUBOV AND M. Y. KUPRIYANOV., “Theoretical investigation of Josephson tunnel Junctions with spatially inhomogeneous superconducting electrodes” ; *Journal of low temperature physics*, 70(1-2), 83–130 (1988).
- [64] I. GIAEVER, “Energy gap in superconductors measured by electron tunneling”; *Phys. Rev. Lett.* 5, (1960).
- [65] A. PLECENÍK, M. GRAJCAR, Š. BEŇAČKA, P. SEIDEL, AND A. PFUCH, “Finite-quasiparticle-lifetime effects in the differential conductance of $\text{Bi}_2\text{Sr}_2\text{CaCu}_2\text{O}_y/\text{Au}$ junctions”; *Phys. Rev. B*, 49, 10016 (1994).
- [66] S. NANDI, M. G. KIM, A. KREYSSIG, R. M. FERNANDES, D. K. PRATT, A. THALER, N. NI, S. L. BUD’KO, P. C. CANFIELD, J. SCHMALIAN, R. J. MCQUEENEY, AND A. I. GOLDMAN, “Anomalous Suppression of the Orthorhombic Lattice Distortion in Superconducting $\text{Ba}(\text{Fe}_{1-x}\text{Co}_x)_2\text{As}_2$ Single Crystals”; *Phys. Rev. Lett.*, 104, 057006 (2010).
- [67] D. P. CHEN AND C. T. LIN “The growth of 122 and 11 iron-based superconductor single crystals and the influence of doping”; *Supercond. Sci. Technol.*, 27, 103002 (2014).
- [68] J.-H. CHU, J. G. ANALYTIS, C. KUCHARCZYK, AND I. R. FISHER, “Determination of the phase diagram of the electron-doped superconductor $\text{Ba}(\text{Fe}_{1-x}\text{Co}_x)_2\text{As}_2$ ”; *Phys. Rev. B*, 79, 014506 (2009).
- [69] A. J. WILKINSON AND P. B. HIRSCH, “Electron Diffraction Based Techniques in Scanning Electron Microscopy of Bulk Materials”; *Micron*, 28, 279-308 (1997).
- [70] S. D. SITZMAN, G NOLZE AND MM NOWELL, “EBSD Pattern Quality and its Use in Evaluating Sample Surface Condition”; *Microsc. Microanal.*, 16, Supplement S2, 698-699 (2010).
- [71] D. REIFERT, N. HASAN, S. DÖRING, S. SCHMIDT, M. MONECKE, M. FELTZ, F. SCHMIDL, V. TYMPEL, W. WISNIEWSKI, I. MÖNCH, T. WOLF AND P. SEIDEL, “Preparation of hybrid

Josephson junctions on Co-doped Ba-122 single crystals”; *Supercond. Sci. Technol.*, 27, 085003 (2014).

[72] S. DÖRING, S. SCHMIDT, F. SCHMIDL, V. TYMPEL, S. HAINDL, F. KURTH, K. IIDA, I. MÖNCH, B. HOLZAPFEL, P. SEIDEL, “Planar hybrid superconductor-normal metal-superconductor thin film junctions based on $\text{BaFe}_{1.8}\text{Co}_{0.2}\text{As}_2$ ”; *Physica C*, 478, 15-18 (2012).

[73] S. SCHMIDT, S. DÖRING, F. SCHMIDL, V. GROSSE, P. SEIDEL, K. IIDA, F. KURTH, S. HAINDL, I. MÖNCH, B. HOLZAPFEL, “ $\text{BaFe}_{1.8}\text{Co}_{0.2}\text{As}_2$ thin film hybrid Josephson junctions”; *Appl. Phys. Lett.*, 97, 172504 (2010).

[74] D. REIFERT “Kontaktentwicklung auf Pniktid-Einkristallen” Master thesis, Friedrich Schiller University Jena (2013).

[75] The image (Fig. 4.1.2) is taken from website of Company MicroChemicals
<http://www.microchemicals.com/company/history.html>

[76] M. MONECKE “Herstellung und Charakterisierung dünner Titan/Goldschichten für superleitende Bauelemente” Bachelor thesis, Friedrich Schiller University Jena (2011).

[77] M. MONECKE “Herstellung und Charakterisierung von Dünnschichtbarrieren für supraleitende Bauelemente” Master thesis, Friedrich Schiller University Jena (2013).

[78] The image (Fig. 4.3.1) and figure’s paragraph is recopied from web site/ <http://www.directvacuum.com/sputter.asp>.

[79] Z. RADI, K. HAVANCSÁK, SZ. KALÁCSKA, A. BARIS, “Surface polishing and slope cut by parallel Ar ion beams for high resolution electron backscatter diffraction measurements”; IEEE- International Conference on Nanotechnology, 1-3 (2014).

[80] S. DÖRING, S. SCHMIDT, S. GOTTWALS, F. SCHMIDL, V. TYMPEL, I. MÖNCH, F. KURTH, K. IIDA, B. HOLZAPFEL AND P. SEIDEL “Influence of the spreading resistance on the conductance spectrum of planar hybrid thin film SNS' junctions based on iron pnictides”; *Journal of Physics: Conference Series*, 507, 012008 (2014).

[81] S. DÖRING, S. SCHMIDT, F. SCHMIDL, V. TYMPEL, S. HAINDL, F. KURTH, K. IIDA, I. MÖNCH, B. HOLZAPFEL, P. SEIDEL, “Development of iron-based superconducting devices”; *Phys. Procedia*, 27, 296-299 (2012).

[82] S. DÖRING, M. MONECKE, S. SCHMIDT, F. SCHMIDL, V. TYMPEL, J. ENGELMANN, F. KURTH, K. IIDA, S. HAINDL, I. MÖNCH, B. HOLZAPFEL, P. SEIDEL, “Investigation of TiO_x barriers for their use in hybrid Josephson and tunneling junctions based on pnictide thin films”; *J. of Appl. Phys.* 115, 083901 (2014).

References

- [83] T. KATASE, Y. ISIMARU, A. TSUKAMOTO, H. HIRAMATSU, T. KAMIYA, K. TANABE, H. HOSONO, “Advantageous grain boundaries in iron pnictide superconductors”; *Nature Comm.*, 2, 409 (2011).
- [84] R. GROSS, P. CHAUDHARI, D. DIMOS, A. GUPTA, AND G. KOREN, “Thermally activated phase slippage in high- T_c , grain-boundary Josephson junctions”; *Phys. Rev. Lett.*, 64, 228-232 (1990).
- [85] N. HASAN, D. REIFERT, S. DÖRING, S. SCHMIDT, V. TYMPEL, F. SCHMIDL, T. WOLF, AND P. SEIDEL, “Planar Hybrid Josephson Junctions Based on Ba-122 Single Crystals”; *IEEE Trans. on Appl. Supercond.*, 26, 1100304 (2016).
- [86] S. DÖRING, S. SCHMIDT, F. SCHMIDL, V. TYMPEL, S. HAINDL, F. KURTH, K. IIDA, I. MÖNCH, B. HOLZAPFEL AND P. SEIDEL, “Edge-type Josephson junctions with Co-doped Ba-122 thin films”; *Supercond. Sci. Technol.*, 25, 084020 (2012).
- [87] J. L. SUN AND J. GAO, “Excess current in high- T_c Josephson junction with thin $\text{PrBa}_2\text{Cu}_3\text{O}_y$ barrier layer”; *Solid State Commun.*, 116, 465–470 (2000).
- [88] V. LACQUANITI, N. DE LEO, M. FRETTO, A. SOSSO, AND M. BELOGOLOVSKII, “Nb/Al- AlO_x -Nb superconducting heterostructures: A promising class of self-shunted Josephson junctions,” *J. Appl. Phys.*, 108, 093701–093708, (2010).
- [89] S. DÖRING, D. REIFERT, N. HASAN, S. SCHMIDT, M. FELTZ, F. SCHMIDL, V. TYMPEL, F. KURTH, K. IIDA, T. WOLF, B. HOLZAPFEL, P. SEIDEL, “Excess currents in planar $\text{Ba}(\text{Fe}_{1-x}\text{Co}_x)_2\text{As}_2/\text{TiO}_x/\text{Pb}$ Josephson junctions” ; *Phys. Status Solidi B*, 1–9 (2015).
- [90] J. WALDRAM, A. PIPPARD, AND J. CLARKE, PHILOS, “Theory of the Current-Voltage Characteristics of SNS Junctions and other Superconducting Weak Links” ; *Trans. R. Soc. A* 268, 265–287 (1970).
- [91] PLECENIK T., GREGOR M., SOBOTA R., TRUCHLY M., SATRAPINSKY L., KURTH F., HOLZAPFEL B., IIDA K., KUS P. , PLECENIK A., “Surface transport properties of Fe-based superconductors: The influence of degradation and inhomogeneity”; *Appl. Phys. Lett.*, 103 052601 (2013).
- [92] N. HASAN, D. REIFERT, S. SCHMIDT, V. TYMPEL, F. SCHMIDL, T. WOLF, AND P. SEIDEL, “Characterizing the Josephson Effect and Andreev Reflection Studies on Ba-122 Single Crystal Junctions”; submitted at *J. of Super. and Nov. Mag.* in ICSM 2016.
- [93] J. KUZNIK, M. ODEHNAL, AND P. SEIDEL, “Simulation of Josephson junction in a microwave field”; *J. Low Temp. Phys.*, 72, 391-406 (1988).

References

- [94] P. SEIDEL, M. SIEGEL, AND E. HEINZ, “Microwave-induced steps in high- T_c Josephson junctions”; *Physica C*, 180, 284-288 (1991).
- [95] P. KOMISSINSKIY, G. A. OVSYANNIKOV, K. Y. CONSTANTINIAN, Y. V. KISLINSKI, I. V. BORISENKO, I. I. SOLOVIEV, V. K. KORNEV, E. GOLDOBIN, AND D. WINKLER, “High-frequency dynamics of hybrid oxide Josephson heterostructures”; *Phys. Rev. B*, 78, 024501 (2008).
- [96] Y. M. SHUKRINOV, I. R. RAHMANOV, K. V. KULIKOV, AND P. SEIDEL, “Effects of LC-shunting on the Shapiro steps features of Josephson junction”; *Europhys. Lett.*, 110, 47001 (2015).
- [97] A. A. GOLUBOV, I. I. MAZIN, “Designing phase-sensitive tests for Fe-based superconductors”; *Appl. Phys. Lett.* 102, 032601 (2013).
- [98] ZHOU Y.R., LI Y.R., ZUO J.W., LIU R.Y., SU S.K., CHEN G.F., LU J.L., WANG N.L., “Phase-Sensitive measurements on the corner junction of iron-based superconductor $\text{BaFe}_{1.8}\text{Co}_{0.2}\text{As}_2$ ”; *arXiv:0812.3295* (2008).
- [99] J.M. ATKINSON MORA, “Probing the superconducting order parameter of Iron-based superconductors through the Josephson effect”; Ph.D thesis, Illinois University (2015).
- [100] R. C. DYNES, V. NARAYANAMURTI, GARNO J. P.: Direct Measurement of Quasiparticle-Lifetime Broadening in a Strong-Coupled Superconductor” ; *Phys. Rev. Lett.* 41, 1509-1512 (1978).
- [101] M. NAKAJIMA, S. ISHIDA, T. TANAKA, K. KIHOU, Y. TOMIOKA, T. SAITO, C. H. LEE, H. FUKAZAWA, Y. KOHORI, T. KAKESHITA, A. IYO, T. ITO, H. EISAKI, S. UCHIDA, “Normal-state charge dynamics in doped BaFe_2As_2 : Roles of doping and necessary ingredients for superconductivity” ; *Sci. Rep.* 4, 5873 (2014).
- [102] TORTELLO M., DAGHERO D., UMMARINO G.A., STEPANOV V.A., JIANG J., WEISS J.D., HELLSTROM E.E., GONNELLI R.S., “Multigap Superconductivity and Strong Electron-Boson Coupling in Fe-Based Superconductors: A Point-Contact Andreev-Reflection Study of $\text{Ba}(\text{Fe}_{1-x}\text{Co}_x)_2\text{As}_2$ Single Crystals . *Phys. Rev. Lett.* 105, 237002 (2010).
- [103] TORTELLO M., DAGHERO D., UMMARINO G.A., STEPANOV V.A., ZHIGADLO N.D., KARPINSKI J., JIANG J., GONNELLI R.S. : Point- Contact Andreev-Reflection Spectroscopy in Fe-Based Superconductors: Multigap Superconductivity and Strong Electron– Boson Interaction. *J. of Super. and Nov. Mag.*, 25, 1297-1301 (2012)
- [104] H.-J. KÖHLER, P. SEIDEL, “Temperature Dependence of the Effective Niobium Energy Gap in Nb-NbO_x-Pb Tunnel Junctions” *Phys. stat. sol. (b)* g, K 51 (1980).

References

- [105] D. DAGHERO, P. PECCHIO, G.A. UMMARINO, R.S. GONNELLI, “Point-contact Andreev-reflection spectroscopy in Fe(Te,Se) films: multiband superconductivity and electron-boson coupling” ; *Supercond. Sci. Tech.* 27, 124014 (2014).
- [106] D. DAGHERO, M. TORTELLO, G. A. UMMARINO, R.S. GONNELLI, “Directional point-contact Andreev-reflection spectroscopy of Fe-based superconductors: Fermi surface topology, gap symmetry, and electron-boson interaction” ; *Rep. Prog. Phys.* 74, 124509 (2011).
- [107] X LU, W PARK, H Q YUAN, G F CHEN, G L LUO, NL WANG, A S SEFAT, M A MCGUIRE, R JIN, B C SALES, D MANDRUS, J GILLET, S. E SEBASTIAN AND L H GREENE, “Point-contact spectroscopic studies on normal and superconducting AFe₂As₂-type iron pnictide single crystals” ; *Supercond. Sci. Technol.*, 23, 054009 (2010).
- [108] G. LI, W. Z. HU, J. DONG, Z. LI, P. ZHENG, G. F. CHEN, J. L. LUO, AND N. L. WANG, “Probing the Superconducting Energy Gap from Infrared Spectroscopy on a Ba_{0.6}K_{0.4}Fe₂As₂ Single Crystal with T_c=37 K”; *Phys. Rev. Lett.* 101, 107004 (2008).

FIGURES	PAGE
2.1.1: (a) The relationship between critical temperature (T_c), critical magnetic field (H_c), and critical current density (J_c). These parameters are a characterization of a superconductor. (b) Meissner effect: a material changes its state from normal metal (NL) to superconductor (SL) under different conditions [25].	5
2.1.2: Characterizes the distance vs. a magnetic field penetrates inside the superconductor material, Exponential decay of a constant applied magnetic field $B_z(x)$ inside a superconductor for the case $\lambda_L > \xi$. Note the small deviation from exponential behavior within a coherence length ξ of the surface. [25]	7
2.1.3: (a) Magnetic field behavior of Type-II superconductor. [25] (b) Flow penetration in the form of vortices, Such a distribution of magnetic field lines is expected for a type-II superconductor, i.e. for all high-temperature superconductors (HTS). [25]	8
2.1.4: (a) Cooper pair: pairing interaction between two electron by a virtual phonon q overall effect [32]. (b) An isotropic s-wave Symmetry of Order parameter OP (Gap Δ in Fig.) [32].	8
2.2.1: Temperature dependence of the energy gap. The temperature is normalized to the critical temperature and the energy gap to the energy gap at 0K. [25]	10
2.2.2: Symmetry of OP: a) Isotropic s-wave, “Fermi Kugel” is written in the German language which means Fermi Sphere. (b) Anisotropic s-wave invariant under 90° rotation, no sign change. (c) d-wave sign change under 90° rotation. [33]	11
2.3.1: Crystal structure of the different classes of FBS. All of these FBS contain FeSe or FeAs building blocks (the iron ions are shown in red and the pnictogen/chalcogen are shown in gold) [41].	12
Table 2.3: Physical properties of iron-based superconductors with those of cuprates and MgB_2 . [45]	13
2.3.2: a) Order parameters in the FBS represented in the 2D 1-Fe Brillouin zone. Different colors stands for different signs of the gap [47]. b) The calculation of band structure for LaFeAsO [48].	13
2.3.3: Left: structure of BaFeAs. [46]. (a) FeAs lattice indicating As above and below the Fe plane. Dashed green and solid blue squares indicate 1- and 2-Fe unit cells, respectively. (b) Schematic of Fermi surface in the 1-Fe BZ whose boundaries are indicated by a green dashed square. The arrow indicates folding wave vector Q . (c) Fermi sheets in the folded BZ whose boundaries are now shown by a solid blue square. [47]	14
2.3.1: A Josephson junction using a Barrier layer between two superconductors. [52]	14
2.3.2: Different junctions geometry where Josephson effect can take place. : (a) point contact, (b) break junction, (c) junction with crossed electrodes and barrier (B),(d) edge junction with barrier (B) and insulator layer (I), (e) nanobridge, and (f) bicrystal grain boundary junction.[53]	15
2.3.3: The temperature profile of the critical Josephson current. The solid lines followed calculations of Ambegaokar and Baratoff, open symbols show experimental results from Fiske [56]	16
2.5.1: schematic I-V characteristics without microwave (a), with a microwave (b). [52]	16

2.6.1: Equivalent circuit diagram of a Josephson junction in a) The resistively shunted Josephson junction RSJ model and b) The resistively and capacitively shunted Josephson junction RCSJ consisting of a power source with the bias current I_b , the Josephson junction (J) and Josephson current I_s , a capacity C, and an Ohmic resistance R.	18
2.3.2: (a) I-V characteristics curves calculated for different values of β_C according to equation (2.5.7) [59]. (b) Schematic I-V characteristics for hysteretic Josephson junctions ($\beta_C > 1$).	20
2.7.: Josephson junctions under irradiation of applied microwave wave showing Shapiro steps (schematic) [25].	21
2.8: Ideal magnetic field dependence of the critical current for Josephson junctions	23
2.9: Andreev Reflection, N/S interface at $T = 0$. [62]	25
2.9.1: Normalized conductance curves of an N/S interface at $T = 0$ calculated within the BTK model with different barrier parameter Z, from pure Andreev ($Z = 0$) to pure tunneling ($Z = 10$) regimes. (b) Effect of the changing temperature on the normalized conductance for $\Delta = 3$ meV and $Z = 0.2$ in all the curves. [62]	26
2.9.2: Conductance curves calculated at $T = 1$ K by using $\Delta = 3.0$ meV, $Z = 0.25$ and increasing values of Γ . [62]	26
3.1.1: (a) A typical Ba-122 single crystal as-grown with rough and scratches (showing irregular surface). (b) Phase diagram of BaFe_2As_2 systems [67].	27
3.1.2: The result of EDX spectrum: (a) a sample of Co-doped: Ba-122 single crystal, Co-element illustrated within the black frames. (b) An example of the undoped crystal samples	28
3.2.1: (a) SEM-image is taken for the surface of a single crystal as grown, (b) irregularities measured by Dek-Tak profilometer for an unprocessed surface of a single crystal	29
3.2.2: Two different types of Abrasive sandpaper of Micro-Mesh Company used for polishing.	31
3.2.3: (a) Logitech device: polishing materials, polishing disk, and polishing head. (b) The polishing head used for fixing a sample. (c) The Polishing head turned up, in order to fix a sample.	31
3.2.4: (a) SEM-image is taken for a sample of polished surface with flattened areas within the white frames, inset figure (b): AFM measurement of a polished surface $\text{RMS} = 1.96$ nm.	33
3.3.1: Microscope image of a polished single crystal, (a) The black lines represent a mask of positive photoresist process, the surface of single crystal illustrated in a white dashed frame. (b) A part of surface illustrated in Fig. 3.3.1 (a), which is an image with high magnification.	33
3.3.2: (a) The etching depth vs. length of a sample measured by Dek-Tak profilometer measurement for the polished surface it's time of etching was 1 min. The peaks represent that the regions of surface are not etched down due to the surface was coated with a mask of a positive photoresist. (b) The different etching times corresponding to the etching depth.	34

List of figures

3.4.1: (a) SEM image of the unprocessed surface of a doped crystal. (b): Kikuchi patterns obtained from its surface at five different locations.	37
3.4.2: Kikuchi -patterns obtained at five different positions (1 to 5) on differently treated (a, b, c) crystal surfaces. (a) and (c) row undoped (twox1228) are polished surface and etched surface respectively, (b) is polished doped crystal (twox925)	35
3.4.3: (a) & (b) Kikuchi -patterns obtained from two samples of Co-doped crystal surfaces treated under the same conditions show clear diffraction pattern reflected from the surface of the crystal.	36
4.1.1: (a) Photograph of the photolithography mask. Schematic of the photolithography mask: (b) Base electrode mask with 10 different junctions area, (c) Pads for counter electrode mask,(d) Counter electrode mask and (e) The combination of all masks previously mentioned [75].	37
4.1.2: Schematic diagram of the three procedures for the photolithography: (a) Positive process. (b) Negative process. (c) Reversal process. [76]	38
4.3.1: Schematic layout of the physical sputtering process: The basic components of a magnetron sputtering system. Ionized Argon bombards a target, releasing atoms which form layers on a substrate. Electrons and Argon ions form plasma, which is located near the target due to the magnetic field, resulting in greater efficiency and quality. [79]	40
4.2.1: Photograph images of a sample of single crystal: (a) An example of a polished sample surface mounted on Si-wafer and placed beside a ruler. (b) & (c) The based electrodes fabricated on surface crystals showed in a yellow color which is a gold protected layer. The pieces of single crystals illustrated in the dashed rectangle border.	41
4.2.2: (a) Photograph image for a sample which contains base electrodes with two junctions. The single crystal is illustrated in the dashed rectangle border. (b) Microscope image of a single junction is illustrated the base electrode surrounded by SiO _x layer (violet).	42
4.2.3: Microscope image: (a) An example of a sample still contains SiO _x -layer completed on the all surface. (b) The elliptical frame indicated the violet color is insulator layer which has been removed during lift-off process.	42
4.2.4: Microscopic image of Al/Au pads on a Si-wafer. (a) An example of Al/Au layers used as pads for counter electrodes (above sputtered gold layer (yellow) with thickness 130 nm and down evaporated Al layer (white) is patterned as rectangles shapes). (b) PbIn evaporated as counter electrode on Al/Au pads.	43
4.2.5: (a) and (b) Microscope image of a planar hybrid junction on a single crystal. (a) The base electrode (above and down in the image) is patterned as rectangles shapes by the protection gold layer (yellow), junction area is in the middle, and is formed by a thick SiO _x layer (green). To improve the contacting of the counter electrode (Pb/In) bilayers of Ti/Au (yellow) have been deposited on the insulator. (b) There is an etching process introduced in this sample for removing Au protection layer from base electrode and junction.	44
4.2.6: (a) Microscope image: a final fabricated junction on a processed crystal. (b) Schematic layout of the junctions.	44

4.2.7: A photo image of a sample which is ready for electrical measurements. A sample of Co: Ba-122 single crystals contains of two junctions. That illustrated in rectangle dotted border.	45
4.2.8: Scanning electron microscope image of a planar cross type junction. The numbers mark the bonding pads. Their assignments to the electrodes are explained in table 1. [81]	45
4.3.1: A schematically image of the used devices illustrated in figure 4.3.3., PC-based measurement system with connected microwave (a) and lock-in amplifier (b).	47
4.3.2: A photo image of a measuring rod. The first part (1) has respective four solder joints for low and high current (I_L , I_H), low and high voltage (V_L , V_H). The second part (2) is an antenna which is used to measuring microwave irradiation. The third part (3) is a sample installed below the antenna.	48
4.3.3: A photo image of used devices in electrical measuring.	48
4.4: Schematic layout (a) tip point contact. b) Soft way: by putting a small drop of silver paste on the fresh sample surface [62]. (c) measuring rod illustrates a sample of single crystal and a metallic tip	49
5.1.1: (a) I-V characteristics from junction with a 5 nm Au barrier and an area of $15 \times 15 \mu\text{m}^2$ measured at 4.2 K. (b) I-V characteristics from junction with a 10 nm Au barrier and an area of $15 \times 15 \mu\text{m}^2$ measured at 4.2 K. The curve compared with Ohmic line (blue).	50
5.1.2: (a) Differential resistance vs. voltage of Au-barrier junction measured at 4.2 K for the sample in fig. 5.1.1 (a.) (b) Differential resistance vs. voltage Au-barrier junction measured at 4.2 K for the sample in fig. 5.1.1 (b).	50
5.2.1: (a) I-V characteristics (blue) from junction with a 10 nm Au-barrier and an area of $15 \times 15 \mu\text{m}^2$ measured at temperature 4.2 K compared with an ohmic line (red). Its differential resistance vs. current included in the figure, too. (b) Temperature dependence of the junction resistance of a Ba-122/Au/Pb with a junction area is of $15 \times 15 \mu\text{m}^2$. The arrows show the T_c of Ba-122 and Pb, where both electrodes become superconducting.	53
5.2.2: (a) Temperature dependence of the junction resistance with a junction area is of $15 \times 15 \mu\text{m}^2$. The foot-like shape may be caused by TAPSs [85], the arrows an the T_c of Ba-122 and Pb, respectively.[86](b) I-V characteristics from junction with a 10 nm TiO_x barrier and an area of $15 \times 15 \mu\text{m}^2$ measured at different temperatures as illustrated in the inset.[86]	54
5.2.3: (a) I-V characteristics fitted with RSCJ- model (blue line) [90]. (b) Temperature dependencies of the $I_c R_N$ -product, which included excess current. [86]	55
5.2.4: (a) I-V characteristics from junction with a 10 nm TiO_x barrier and an area of $15 \times 15 \mu\text{m}^2$ measured at different temperatures as illustrated in the left box.[93] (b) I-V characteristics fitted with RSCJ- model (red line). Parameters of fit are given in the text. [93]	56
5.2.4: (c) Temperature dependence of the critical current (I_c) (square), reduced critical current by excess current (I_c^*) (circles), excess current (I_{ex})(triangle). [39]	56
5.2.5: (a) I-V characteristics from junction with a 10 nm TiO_x barrier and an area of $25 \times 25 \mu\text{m}^2$ measured at different temperatures as illustrated in the left box. The inset figure: I-VC measured at 4.2 K and fitted within RCSJ-model (red line). Parameters of fit are given in the text. (b) Temperature dependence of the critical current (I_c). [90]	57

List of figures

<p>5.2.6: (a) selected I-V characteristics from junction in fig. 5.2.3 under different microwave amplitude (a.u) measured at 18 GHz. the arrows mark the first Schapiro steps. (b) Zeroth Shapiro step (top) and higher steps $n = 1, 2, 3$ (bottom) as function of microwave amplitude (measured at 18 GHz). Measured data are shown as squares, whereas simulations are represented as straight lines, simulations with $\Omega=0.03$. [86]</p>	58
<p>5.2.7 (a) I-V characteristic under different microwave amplitudes (a.u.) measured at 2 GHz at $T=4.2$ K. for the junction shown in fig. 5.2.4 (a) Normalized critical current (I_c) and first Shapiro-step ($n=1$) vs. microwave amplitude (measured at 2 GHz). Measured data are shown as circles and squares, whereas simulations with $\Omega=0.30$ are represented as straight lines. [93]</p>	59
<p>5.2.8: (a) Critical current versus magnetic field based on I-V characteristics for sample Twox925_JJB measured at 4.2 K [86]. (b) Critical current versus magnetic field shows in the inset figure, Junction geometry desgined by corner junction. [100]</p>	60
<p>5.2.9: (a) differential resistance vs. voltage measured at different temperatures between 4.2 K and 26.6 K. (b) Normalized conductance vs. voltage of TiO_x planar junction measured at different temperatures. Spectra are shifted against each other by 0.25. [93]</p>	61
<p>5.2.9: Normalized conductance vs. voltage of AlO_x-barrier planar junction from junction with an area of $15 \times 15 \mu m^2$, which measured at different temperatures illustrated in right box. Arrows marked for $\Delta_1=2.2$ meV and $\Delta_2 =8.5$ meV. [93]</p>	62
<p>5.3.1: (a) I-V characteristics from doped single crystal and Nb tip measured at 4.2 K. its differential resistances vs. voltage of contact measured directionally at 4.2 K. (b) Normalized conductance vs. voltage measured at 4.2 K, the black and red line represents measured data and Golubov-fit, respectively. Arrows with 1, 2, 3 numbers represent Δ_{Nb}, Δ_1, and Δ_2 for Ba-122, respectively. [93]</p>	63
<p>5.3.2: (a) Temperature dependence of the contact resistance obtained from a Co-doped single crystal and Nb electrode. (b) I-V characteristics and its differential resistance measured at 4.2 K.</p>	65
<p>5.3.3: (a) Differential resistance vs. voltage of contact at different temperatures. (b) Normalized conductance of contact at different temperatures.</p>	66
<p>5.3.4 : (a) Differential resistance vs. voltage of contact at different temperatures.(b) Normalized conductance of contact vs. voltage at different temperatures from 4.2 K to 26.5 K.</p>	66
<p>5.3.5: (a), (b), (c) Differential resistance vs. voltage based on the same contact measured at $T=4.2$</p>	67

Ehrenwörtliche Erklärung

Ich erkläre hiermit ehrenwörtlich, dass ich die vorliegende Arbeit selbständig, ohne unzulässige Hilfe Dritter und ohne Benutzung anderer als der angegebenen Hilfsmittel und Literatur angefertigt habe. Die aus anderen Quellen direkt oder indirekt übernommenen Daten und Konzepte sind unter Angabe der Quelle gekennzeichnet.

Bei der Auswahl und Auswertung folgenden Materials haben mir die nachstehend aufgeführten Personen in der jeweils beschriebenen Weise entgeltlich/unentgeltlich geholfen:

1. Frau C. Voigt (AG Experimentelle Festkörperphysik) war bei der Erstellung der Dek-Tak Messungen Aufnahmen behilflich. Insbesondere erfolgte die für die Messungen der Oberflächenrauheit der Proben notwendige Probepräparation durch sie.
2. Herr S. Schönherr (AG Experimentelle Festkörperphysik) war bei der Erstellung der EDX-Aufnahmen behilflich. Insbesondere erfolgte die für die Messungen der Co-Konzentration in der Probenkomponente notwendige Probepräparation durch sie.
3. Dr. W. Wisniewski (Otto-Schott-Institute of Materials Research, FSU Jena) und Prof. Dr. S. Teichert (University of Applied Sciences Jena, Department of SciTec) waren bei der Erstellung der Proben von SEM-Aufnahmen und EBSD-Messungen behilflich. Es erfolgte auf die für die Analyse der Oberflächenrauheit der Proben notwendige Probepräparation durch sie.

Weitere Personen waren an der inhaltlich-materiellen Erstellung der vorliegenden Arbeit nicht beteiligt. Insbesondere habe ich hierfür nicht die entgeltliche Hilfe von Vermittlungs- bzw. Beratungsdiensten (Promotionsberater oder andere Personen) in Anspruch genommen. Niemand hat von mir unmittelbar oder mittelbar geldwerte Leistungen für Arbeiten erhalten, die im Zusammenhang mit dem Inhalt der vorgelegten Dissertation stehen.

Die Arbeit wurde bisher weder im In- noch im Ausland in gleicher oder ähnlicher Form einer anderen Prüfungsbehörde vorgelegt.

Die geltende Promotionsordnung der Physikalisch-Astronomischen Fakultät ist mir bekannt.

Ich versichere ehrenwörtlich, dass ich nach bestem Wissen die reine Wahrheit gesagt und nichts verschwiegen habe.

Jena, 02.09.2016

Noor Ali Hasan

Lebenslauf

Noor Hasan

- 24.01.1984 geb. in Bagdad
- 09/1989-08/1995 Grundschule
- 09/1995-08/2001 High school / Balgees for girls
- 2001 Abitur (Note: 75.3%)
- 09/2001-06/2004 Studium der Physik (Bachelor of Science Degree in Physics)
an der Al-Nahrain-Universität/ Irak
- 09/2004 – 02/2008 MasterArbeit M.Sc. (Master of Science Degree in Physics)
an der Al-Nahrain-Universität/ Irak
- 2008 Abschluss als Master-Physikerin (Note: 76.8%)
- 08/2008 – 03/2012 berufliche Tätigkeit als Lehrerin
an der Technische Universität
Fakultät für Angewandte Wissenschaften / Irak
- 04/2012 – 10/2012 Deutsche Sprache lernen
interDaF eV. am Herder-Institut der Universität Leipzig/Deutschland
- 10/2012-09/2016 Doktorandin am Institut für Festkörperphysik
Friedrich-Schiller-Universität Jena/ Deutschland
(gefördert von DAAD)

Jena, 02.09.2016

Noor Ali Hasan

ACKNOWLEDGEMENT

I would like to take this opportunity to express my profound gratitude and deep regards to the German Academic Exchange Service (DAAD) for their cordial support, valuable information, guidance and, financial assistance as I accomplish my research in Germany.

This work also was partially supported by Friedrich-Schiller-Universität Jena (ProChance 2015/ Programme Line A2), Institute of Physics IOP, and the DPG “Deutsche Physikalische Gesellschaft e.V.”. These bursaries supported my attendance for the 12th European Conference on Applied Superconductivity EUCAS 2015, 5th International conference superconductivity and magnesium ICSM2016, and DPG conferences in Dresden and Berlin, respectively.

I would particularly like to thank Prof. PAUL SEIDEL who allowed me to work in his working group as well as write my Doctoral thesis at Friedrich Schiller-Universität Jena particularly in the Institute of Solid State Physics (IFK).

Gratitude goes to Prof. FRANK SCHMIDL, who always found time for helping me such advising on my research work as well as to teach me in the laboratory, how to use the systems of the vacuum chambers. I’m always grateful for his advice and his assistance.

I would also like to thank DR. VOLKER TYMPEL for his active support and helping me in laboratory measurements without him, the measurements have been impossible to be done.

My thanks go to my working group (DAVID REIFERT, SEBASTIAN DÖRING, AND STEFAN SCHMIDT) for their advice.

Of Course, one cannot forget each person in IFK for his help like SYLVIA STENDER, KRISTINA GARLIPP who helped me in the clean room and helpful advice during the polishing of surface single crystals.

I would like to thank RALF NEUBERT & HOLGER MÜHLIG who helped me how to use origin.9 and installing it.

I would like to thank Dr. ANDREAS PFUCH from INNOVENT e.V. Jena who allowed me to work in his laboratory in order to sputter SiO_x layer on some samples.

Dr. THOMAS WOLF from the Karlsruhe Institute of Technology, I would like to thank him for his cooperation for sending the iron pnictide single crystals materials.

To perform the SEM images and EBSD measurements, I would like to thank Prof. STEFAN TEICHERT and Dr. WOLFGANG WISNIEWSKI.

I would like to thank MR. S. SCHÖNHERR to perform analysis by energy dispersive X-ray spectroscopy (EDX).

I want to thank CARMEN VOIGT for doing the measurements of Dek-Tak profilometer.

I would like to thank my housebound and my little son, my family; parents, my sister and my brother, who all supported me in every situation and without which neither this work nor my studies would have been possible.

Finally, I am very much thankful Almighty for his constant support because without him this assignment would never be possible.